POLITECNICO DI MILANO
DEPARTMENT OF AEROSPACE SCIENCE AND TECHNOLOGY
DOCTORAL PROGRAMME IN AEROSPACE ENGINEERING

NUMERICAL STUDY OF AERODYNAMIC AND AEROACOUSTIC METHODS BASED ON COMPUTATIONAL FLUID DYNAMICS FOR HELICOPTER ROTOR FLOWS: DEVELOPMENT, IMPLEMENTATION AND VALIDATION ISSUES

Doctoral Dissertation of:
Jinbin Fu

Supervisor:
Prof. Luigi Vigevano

Tutor:
Prof. Alberto Guardone

The Chair of the Doctoral Program:
Prof. Pierangelo Masarati

Academic Year 2022/23 – Cycle XXXIII

Acknowledgements

My five year doctoral program at Politecnico di Milano is an experience I treasure deeply and hold as one of the most meaningful in my life. Coming to the end of my Ph.D. journey, I would like to thank all those who made this moment possible.

I am truly grateful to my supervisor, Professor Luigi Vigevano, for his invaluable contributions to my project. His expertise in rotor aerodynamics and aeroacoustics, as well as his step-by step guidance and continuous support, have been instrumental in my success. I would not have been able to complete this doctoral thesis without his dedicated efforts from the beginning. I extend my heartfelt thanks for his encouragement, technical knowledge, and unwavering support.

I would like thank to Prof. Renzo Arina and Dr. Michel Costes, my thesis reviewers. Your willingness to devote your valuable time and expertise to reviewing my work is deeply appreciated. Your insightful comments and constructive suggestions greatly improved my thesis and will be highly valuable for my future research.

I wish to thank all my friends I met at Politecnico di Milano and in Italy. I appreciate our friendship and all the exciting experiences we have shared, including the silly moments that make us laugh. I treasure all of the memories we have created together and I hope that our paths will intersect again soon in the future.

The use of the clusters CFDHUB of Politecnico di Milano and the high performance computing resources at CINECA (https://www.hpc. cineca.it/) under the ISCRA initiative, ISCRA-C project NOGENROT and ROVOC, is gratefully acknowledged.

Most importantly, my deepest gratitude goes to my parents for their boundless patience and love throughout these years, and for supporting me in every difficult moment. I would also like to thank my girlfriend, Xiaonan Wang. You are one of the best things that have ever happened to me in my life.

Finally, thanks to China Scholarship Council (CSC) for the financial support to me to study in Italy (No. 201706030145).

Abstract

The simulation of helicopter rotor flows and the prediction of rotor impulse noise are practically very challenging tasks from a computational perspective as the flight environment of a helicopter rotor contributes to extremely complex flow phenomena and noise generation mechanisms, For instance, such rotor systems often experience the Blade-Vortex Interaction (BVI) phenomenon in low-speed descending flight, where the rotating blades interact with tip vortices shed from previous blades, resulting in obtrusive noise levels; and/or operate in high-speed flight conditions, where shock waves appear in the blade tip region, resulting in highly impulsive transonic noise. While analytical, semi-empirical, and low-fidelity numerical approaches can quickly provide results suitable for performance analysis, they are poorly predictive as these models are insufficient to fully resolve the complicated flow phenomenon described above. With this in mind, the present work combines Computational Fluid Dynamics (CFD) methods with the Ffowcs-Williams and Hawking (FW-H) acoustic analogy to accurately calculate the aerodynamics and aeroacoustics of helicopter rotors. The core of this dissertation is divided into three main parts; (i) construct and validate a simulation framework for helicopter rotor wake modeling and rotor noise prediction; (ii) implement the two vortex feature-based second vorticity confinement (VC2) models into the CFD solver ROSITA and assess the capabilities of these two models in three-dominated flows; (iii) develop a three-dimensional r-refinement method that effectively concentrates mesh points into regions of interest without mesh tangling for improving the vorticity preservation in helicopter rotor flows.

The first part of this thesis is dedicated to the construction and validation of the simulation framework for helicopter rotor aerodynamics and aeroacoustics. In this simulation framework, the CFD solver ROSITA is used for the simulation of helicopter rotor flows; a novel acoustic solver ROCAAP that employs the Retarded-Time based Permeable Surface FW-H (PS-FWH) equation for subsonic noise source and the Marching-Cube Emission-Surface (MCES) based PS-FWH equation for transonic/supersonic noise source is developed for noise prediction; a high-efficient rotor trim algorithm that combines the original delta trim algorithm with multiple levels of the grid and temporal resolutions is proposed for obtaining the trimmed rotor in forwarding flight. The validation work is then performed through a sequence of numerical

test cases. Firstly, the acoustic solver is validated by comparing with analytical spherical monopole source solutions and the well-established WOPWOP solutions; three well-documented forwarding flight rotors are then employed to validate the rotor trim method; finally, the performance of the integrated simulation framework is demonstrated via the prediction of the transonic rotor noise and the BVI rotor noise.

In the second part, two locally normalized vortex feature detection techniques (non-dimensional Q and λ_2 criteria) are combined with the original VC2 model, resulting in the FVC2-L2 and the FVC2-Q models, respectively. These two vortex feature-based VC2 models have been implemented into the CFD solver ROSITA and compared with the results of the standard CFD solver and those of the original VC2 model in two benchmark test cases (NACA0015 wing in steady state and Caradonna-Tung rotor in hover condition). The result shows that the performances of the feature-based VC2 models in terms of computational stability, aerodynamics prediction, vorticity preservation, and computational efficiency are significantly improved. In particular, the FVC2-L2 model allows using higher confinement parameter values to achieve better solutions than the FVC2-Q model. On this basis, the FVC2-L2 model is then adopted for the HART-II rotor descending flight case to enhance the prediction of the helicopter rotor BVI phenomenon. Afterward, the non-lifting UH-1H hovering rotor case and the AH-1/OLS forwarding flight case are employed to demonstrate the ability of the FVC2-L2 model to provide more reliable noise predictions than the non-VC models, even if there are no tip vortices shed from the blade tip.

The third part of this thesis describes an effective three-dimensional r-refinement method to improve the vorticity preservation in helicopter rotor flows. This approach relies on the Jacobian-weighted elliptic grid generation method, which derives from the combination of the variational principle and the least-square fitting of the inverse Jacobian matrix to the weight matrix. In this part, the original Jacobian-weighted elliptic method is extended from two dimensions to three, and the derivation of the weight matrix in three dimensions is presented for the first time. Several practical test examples are used to preliminary validate this three-dimensional method. The results show that this method is effective and reliable in generating grids without mesh tangling after the redistribution procedure. Furthermore, the potential of this method in the application of helicopter rotor flows is also demonstrated.

Contents

List of Figures

List of Tables

List of Symbols

Latin Symbols

a	Attractive Strength
AR	Aspect Ratio
c	Airfoil Chord
c_0	Local Speed of Sound
C_D	Drag Coefficient
C_L	Lift Coefficient
C_M	Moment Coefficient
C_{Mx}, C_{My}	Rolling, Pitching Moment Coefficient
C_n	Normal Force Coefficient
C_P	Pressure Coefficient
C_T	Thrust Coefficient
f	Integration Control Surface
$f_{threshold}$	Threshold function
f_0	Cut-off Value
$\mathbf{F_b}$	Body Force Term
$\mathbf{F_c}$	Convective Flux Tensor
$\mathbf{F_d}$	Diffusive Flux Tensor
$\mathbf{F_s}$	Source Term
$\overline{\boldsymbol{F}}_{\boldsymbol{s}}$	Modified Source Term
$H(f)$	Heaviside Function
$\boldsymbol{J}$	Jacobian Matrix
k_x, k_y	Inflow coefficients
l	Length of the Local Tangent Vetors of a Curve
$\mathbf{M}$	Mach Number Vector of Source at Control surface
M	Mach Number

M_T	Blade Tip Mach Number
M_x, M_y	Rolling, Pitching Moment
$\mathbf{n}$	Unit Normal Vector Outwards to the Control Surface
N_b	Number of Rotor Blades
N_c	Number of CFD Grids
N_{quad}	Number of Quadrilateral Elements
N_{tri}	Number of triangular Elements
N_{tot}	Number of Total Grid Cells
N_X, N_Y, N_Z	Number of Grid Cells in X, Y, Z Direction
N_ξ, N_η, N_ζ	Number of Grid Cells in Chordwise, Normal, Spanwise Direction
p	Local Fluid Pressure
p'	Acoustic Pressure
p'_T, p'_L	Thickness, Loading Noise Pressure
p_0	Undisturbed Medium Pressure
P_{ij}	Compressive Stress Tensor
$\mathbf{Q_c}$	Convective Flux Balance
$\mathbf{Q_d}$	Diffusive Flux Balance
$\mathbf{r}$	Distance Vector from Observer to Source
R	Rotor Radius
$\mathbf{R}$	Flux Balance
Re	Reynolds Number
$\boldsymbol{S}$	Weight Matrix in Jacobian-Weighted Elliptic Grid Equation
S_{cs}	Control Surface Ordered Pair
S_{ijk}	Cell Surface of the Hexahedral Cell ijk
t	Time Variable
T	Thrust
T_{ij}	Lighthill's Equivalent Stress Tensor
u_i	Local Fluid Velocity Components
U_P	Perpendicular Inflow Velocity Components
U_T	Tangential Inflow Velocity Components
$\mathbf{v}$	Entrainment Velocity Vector
v_i	Local Surface Velocity Components
V_{ijk}	Cell Volume of the Hexahedral Cell ijk
$\mathbf{W}$	Conservative Variables Vector
$\mathbf{x}$, $\mathbf{y}$	Observer, Source Position Coordinates
x, y, z	Coordinates in Physical Space
Δx_t	Spanwise Extension Outward to the Blade Tip Section
Δy_r	Maximum Radial Extension at the Blade Section Center
ΔX, ΔY, ΔZ	Minimum Spacing of Grid Cells in X, Y, Z Direction
$\Delta\xi$, $\Delta\eta$, $\Delta\zeta$	Minimum Spacing of Grid Cells in Chordwise, Normal, Spanwise Direction

Geeks Symbols

α	Angle of Attack
β	Blade Flapping Angle
β_0	Blade Pre-Cone Angle
β_{1c}	First Harmonic of Blade Lateral Cyclic Flap Angle
β_{1s}	First Harmonic of Blade Longitudinal Cyclic Flap Angle
ϵ	Tolerance
$\delta(f)$	Dirac Delta Function
δ_{ij}	Kronecker's Delta
μ	Advanced Ratio
λ	Inflow Ratio
λ_c	Climbing Inflow Ratio
λ_i	Induced Inflow Ratio
θ	Blade Pitch Angle
θ_0	Blade Collective Pitch Angle
θ_{1c}	First Harmonic of Blade Lateral Cyclic Pitch Angle
θ_{1s}	First Harmonic of Blade Longitudinal Cyclic Pitch Angle
θ_{tw}	Twist Angle of Rotor Blade
ρ	Local Fluid Density
ρ_0	Undisturbed Medium Density
τ	Source time variables
τ_{ij}	Viscous Stress Tensor
ψ	Azimuth Angle
Ψ	Wake Age Angle
ϕ	Inflow Angle
$\boldsymbol{\omega}$	Vorticity Vector
$\omega_x, \omega_y, \omega_z$	Vorticity Vector Components
Ω	Angular Velocity
Ω_C	Computational Domain
Ω_P	Physical Domain
Λ	Doppler Term in Emission-Surface Formulation
Σ	Emission Surface
ε	Confinement Parameter
ε_o	Reference Confinement Parameter
ξ, η, ζ	Coordinates in Computational Space

Abbreviation

2D	Two-Dimensional
3D	Three-Dimensional

A

AMR	Automatic Mesh Refinement
APE	Acoustic Pertubation Equations

B

BET	Blade Element Theory
BILU	Block Incomplete Lower-Upper
BVI	Blade-Vortex Interaction

C

CAA	Computational Aeroacoustics
CFD	Computational Fluid Dynamics
CFL	Courant-Friedrichs-Lewy
CPU	Central Processing Unit
CRWENO	Compact-Reconstruction Weighted Essential Non-Oscillatory

D

DES	Detached Eddy Simulation
DNW	German-Dutch Wind Tunnel
DOF	Degree of Freedom

E

ENO	Essential Non-Oscillatory
EPS	Emission Porous Surface

F

FD	Finite-Difference
FFT	Fast Fourier Transformation
FV	Finite-Volume
FVC2-L2	λ_2-based Second Vorticity Confinement
FVC2-Q	Q-based Second Vorticity Confinement
FW-H	Ffowcs Williams and Hawkings

G

GCG	Generalized Conjugate Gradient

H

HART-II	Second Higher-Harmonic Control Acoustic Rotor Test
HSI	High-Speed Impulsive

I

IS-FWH	Impermeable Surface Ffowcs Williams and Hawkings

L

LBM	Lattice-Boltzmann Method

LEE	Linearized Euler Equations
LES	Large Eddy Simulation

M

MC	Marching-Cube
MCES	Marching-Cube Emission-Surface
MUSCL	Monotonic Upstream-centered Scheme for Conservative Law

O

OLS/TAAT	Operational Load Survey/Tip Aerodynamics and Acoustics Test
OVC2	Standard Second Vorticity Confinement

P

PDEs	Partial Differential Equations
PS-FWH	Penetrable Surface Ffowcs Williams and Hawkings
PSOR	Point Successive Over-Relaxation

R

RANS	Reynolds-Averaged Navier-Stokes
ROCAAP	ROtorcraft Code for AeroAcoustic Prediction
ROSITA	ROtorcraft Software ITAly

S

SA	Spalart-Allmaras
SAS	Scale-Adaptive Simulation
SGS	Subgrid-Scale
SRS	Scaled-Resolving Simulation

T

TFI	Tranfinite Interpolation
TPP	Tip Path Plane

V

VC	Vorticity Confinement
VC1	First Vorticity Confinement
VC2	Second Vorticity Confinement
VLES	Very Large Eddy Simulation
VVPM	Viscous Vortex Particle Method

W

WENO	Weighted Essential Non-Oscillatory
WMLES	Wall-Modeled Large Eddy Simulation

CHAPTER 1

Introduction

1.1 Background and Motivation

HELICOPTERS are versatile flying vehicles that can achieve missions that regular fixed-wing aircraft are incapable of due to their uniqueness in vertical take-off, landing, hovering, and flying maneuvering. However, these versatile characteristics come at a price. The flight environment of a helicopter rotor contributes to both extremely complex flow phenomena and obtrusive noise levels, which will limit the scope of helicopter operation, as shown in Figure.1.1. For instance, on the advancing blade side, where the relative blade velocity is in the relative freestream direction, the delocalized shock waves appear near the blade tip region and generate the High-Speed Impulsive (HSI) noise with in-plane directivity. While on the retreating blade side, where the blade moves opposite the flight direction, the dynamic stall may occur due to the necessity of moment balance. Particularly, the interaction of shed blade tip vortices with the following rotor blades severely impacts the blade local airloads and results in the annoying and loud Blade-Vortex Interaction (BVI) noise. In addition, the highly unsteady airloads may cause aeroelastic behavior. Therefore, having a more penetrating understanding of these complex aerodynamic phenomena and noise generation mechanisms can potentially expand the flight envelope of helicopters.

1.1.1 Nature of Rotor Wake

The rotor vortical wake is among the most complex fluid dynamic structures in the aforementioned helicopter unsteady flow field. The shed blade vortices in the rotor wake intersected with the rotor blade causing the BVI phenomenon, which significantly affects the blade airloads and results in the annoying and impulsive noise. The rotor-induced wake that interacts with the surrounding obstacles can typically degrade

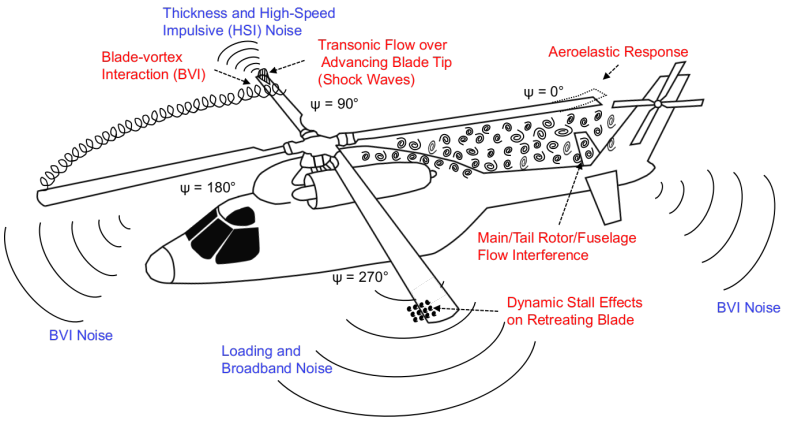

Figure 1.1: *Complex flow phenomena over the helicopter and aerodynamically generated noise emitted by the helicopter rotor, adapted from [1]*

the helicopter performance and creates a hazardous environment. The interference of the main/tail rotor/fuselage negatively influences the vehicle dynamics. For these reasons, a better understanding of the physics of rotor wake development is essential for improving the prediction of helicopter rotor aerodynamics and aeroacoustics.

Naturally, the vortical wake from the rotating blade consists of a shed vortex sheet and a concentrated blade tip vortex, as illustrated in Figure.1.2. Owing to the conservation of circulation, the vorticity generated by the circulation variations is shed and trailed into the wake, producing the vortex sheet. In particular, a high-strength trailing vortex sheet is created on the blade tip and rolls up quickly into a concentrated vortex due to the rapid changes of circulation over the spanwise orientation near the blade tip [2].

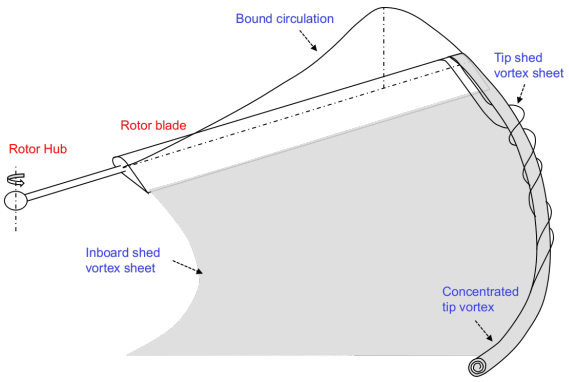

Figure 1.2: *Schematic showing the shed wake and concentrated tip vortex, adapted from [3].*

The geometry and strength of the rotor wake are highly dependent on the operating state of the helicopter. For example, in hover flight, see Figure 1.3a, the vortices form a radially axisymmetric helical wake and convect axially downward below the rotor disk. During this procedure, the tip vortices progressively contract radially and reach an asymptotic value of approximately $r/R = 0.78$. Meanwhile, the tip vortices descend axially with a relatively slow velocity and abruptly increase after the first blade passage due to the downwash passing the blade. In forward flight, see Figure 1.3b, the

rotor wake structures become more distorted and complicated due to the freestream component of the velocity at the rotor plane. The vortices trailed from the blade tips initially form as a series of interlocking epicycloids and convect below and behind the rotor. With the mutual interaction between the shedding filaments, some distortion of vortices appears mainly in the perpendicular plane of the rotor. At the same time, the tip vortices along the lateral edges of the wake gradually roll up into concentrated vortex bundles. In particular, the tip vortices that trail off the blades may interact with the following blades, resulting in the BVI phenomena, which is one of the distinguishing features of rotor wake in forward flight. It becomes more intense when the rotor is in low-speed descending flight where the vortices are convected downstream at relatively slower rates.

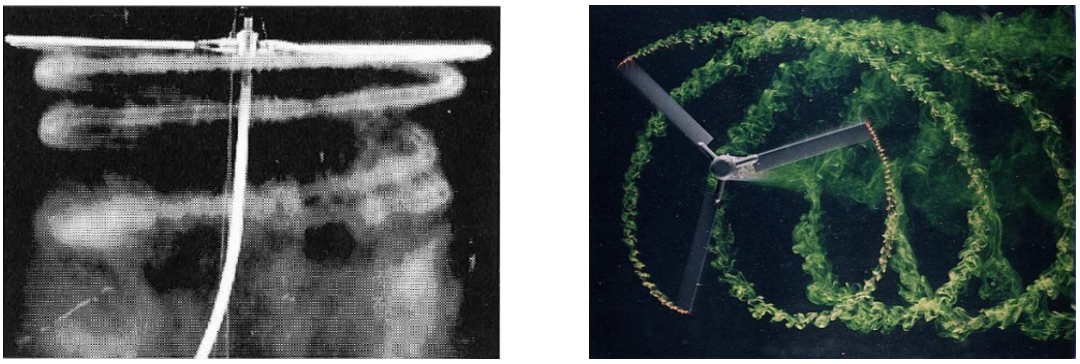

(a) *Wake visualization of a two-bladed rotor*

(b) *Wake visualization of a three-bladed rotor in forward flight*

Figure 1.3: *Rotor wake visualization for helicopter rotor in hover and forward flight [4].*

1.1.2 Physics of Rotor Aerodynamically Generated Noise Source

The complex aeromechanical environment contributes to tonal and broadband aerodynamically noise through several distinct noise mechanisms [1]. Figure 1.4 presents a typical rotor far-field noise spectrum. The tonal noise, also known as the harmonic or discrete frequency noise, consists of the deterministic noise sources, usually divided into thickness and loading noise, blade-vortex interaction noise, and high-speed impulsive noise. The broadband noise is the continuous component of the spectrum and contains the non-deterministic and non-periodic loading noise source caused by the turbulence flow over the blades, such as turbulence ingestion noise, blade-self noise, and blade-wake interaction noise.

In the broadband component, the interaction of the blades with the turbulence in the upcoming flow (atmosphere and rotor wake) is typically recognized as the most relevant mechanisms of turbulence ingestion noise and blade-wake interaction noise, respectively. Blade-self noise is related to the random pressure fluctuations on the blade surface result from turbulence within the attached and seperated boundary layer [6].

In terms of the tonal part, thickness noise arises from the fluid passing over the blade, while loading noise is generated by the unsteady aerodynamics act on the moving blade surface. Blade-vortex interaction noise is associated with the high-frequency pressure fluctuations on the blade surface produced by a shed tip vortex subsequently

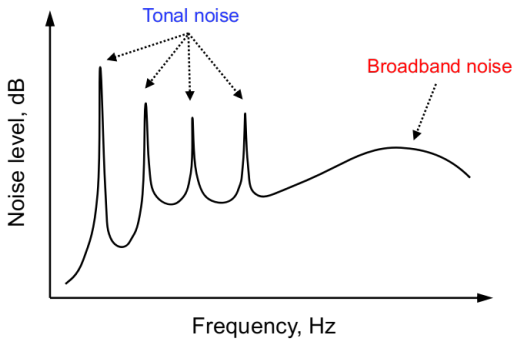

Figure 1.4: *Example of the typical spectrum of a rotor far-field noise, adapted from [5]*

impinging on the following blades. High-speed impulsive noise is engendered by the shock delocalization on the rotor advancing blade side when the blade is moving at high tip speeds. Generally, thickness noise and loading noise are classified as rotational noise, while blade-vortex interaction noise and high-speed impulsive noise are known together as impulsive noise. In both civilian and military operations of helicopters, the impulsive noise sources are the most annoying component and thus receive much attention from the helicopter community.

1.2 Literature Review

This section performs a literature survey to assess the current research status in rotor aerodynamics simulation and aeroacoustics prediction. In this effort, the present work overviews recent progress in modeling rotor wake with an emphasis on computational fluid dynamics (CFD) based techniques and in predicting rotor noise with an emphasis on integral methods.

1.2.1 Rotor Wake Modeling Techniques

Over the last decades, various techniques have been developed to model the rotor wake of helicopters. These approaches could be mainly divided into two categories: vortex wake methods based on vortex theory and CFD-based techniques. In the next, I will briefly overview the vortex wake methods and emphasize on the research with CFD approaches.

1.2.1.1 Vortex Wake Methods

The vortex wake methods include rigid wake models [7], prescribed wake models [8,9], and free-vortex wake models [10–13]. In rigid wake models, the trailed vortices are modeled as skewed helical filaments with the assumptions of no wake contraction, inviscid, and uniform flow field. This method is able to reasonably model the primary effects of wake skewness in forward flight with high efficiency, but the predicted wake geometries differ significantly from the experiment in edgewise flow due to the assumption of no wake contraction. For this reason, the prescribed wake models were developed using empirical expressions derived from experimental observations. In these methods, the locations of trailed vortices are modeled as a function of wake ages, con-

sidering the wake contraction effect. However, they do not offer much flexibility on rotor geometry, and the influence of actual induced flow velocities of the wakes and blade surfaces is not taken into account. In contrast, free-vortex wake models based on the potential flow assumption provide this sought-after flexibility because the formulation process does not require experimental data. Furthermore, the induced velocities are calculated through the Biot-Savart law. Nevertheless, the results of free-vortex wake models are generally sensitive to the empirical models of the tip vortex core structure and the viscous growth of the vortex core [11, 13]. Therefore, the free-vortex wake models cannot accurately model the true physics of the problem.

1.2.1.2 CFD-based Techniques

The numerical modeling of helicopter rotor wake garnered new development through CFD techniques which are capable of providing a complete description of a viscous, turbulent, compressible trailing vortex. In the later 1980s, the Euler and Navier-Stokes equations were start to introduced to simulate the helicopter rotor flow field [14–17]. However, initially, the Euler/Navier-Stokes equations were only used in the near-field around the rotor blades, the wake effects were still calculated using an external wake models. Thanks to the enormous advances of scientific computing capabilities in the 1990s, efforts were emerged to capture the rotor wake as a part of overall numerical solution without relaying on any external wake models [18, 19].

Over the last three decades, the application of CFD-based methods in helicopter rotor wake modeling has progressed tremendously. In recent years, primary research on rotor wake modeling has focused on obtaining high resolved vortex wake through different numerical approaches. Currently, there are four major ways of improving the vorticity preservation on helicopter rotor flowfield simulation: scale-resolving simulation (SRS), grid refinement, high-order scheme and vorticity confinement techniques. Each of these methods will be described briefly.

Scale-Resolving Simulation (SRS) Methods The scale-resolving simulation (SRS) methods are a class of models that could resolve at least a portion of the turbulence spectrum in at least a portion of the numerical domain [20]. Large Eddy Simulation (LES), developed for nearly six decades, is the first SRS method. In LES, the large energetic scales are resolved by implementing low-pass filtering on Navier-Stokes equations; the effect of unresolved small scales is usually accounted for using a subgrid-scale (SGS) model. From the principle idea of LES, it is very suitable for simulating helicopter rotor flow field, which highly depends on the vortices trailing from blade tips. However, when the wall-bounded flow is involved, the computational cost becomes prohibitively expensive, especially for high Re number situations, since a high resolution in both space and time is required near the wall. This makes LES impractical for most of the engineering flows. Table 1.1 outlines an estimation of the required computational power in Reynolds-Averaged Navier-Stokes (RANS) equations and LES simulations for a single turbomachinery blade with end-walls ($Re \approx 10^5$). It can be seen that the workload for LES is at least 5 orders of magnitude that of the RANS simulation even for such low Re number.

To eliminate the severe limitations of LES, a large variety of hybrid RANS-LES approaches emerged, where large scales are only resolved away from walls and the wall

Table 1.1: *Estimation of CPU resources required in RANS and LES simulations for a single turbomachinery blade with end walls [20]*

Method	Mesh number	Real time step	Pseudo time step	Workload ratio to RANS
RANS	$\sim 10^6$	$\sim 10^2$	1	1
LES	$\sim 10^8 - 10^9$	$\sim 10^4 - 10^5$	10	$\sim 10^5 - 10^7$

boundary layers are computed by a RANS method, such as Scale-Adaptive Simulation (SAS), Detached Eddy Simulation (DES), Wall Modeled LES (WMLES), . . .).

In the last decade, some of the hybrid RANS-LES models have been applied to the simulation of helicopter rotor flowfield for accurately resolving the vortical wake [21–24]. For example, Chaderjian and Ahmad [21] used DES model to study the wake of a UH-60 rotor. Meanwhile, the Automatic Mesh Refinement (AMR) technique was employed to reduce error from numerical diffusion. In this study, the vortical worms produced through a process of wake shear-layer entrainment into the tip vortices and vortex stretching were well resolved. Dehaeze *et al.* [23] explored the DES for the flowfields of the HART-II rotor in BVI condition. A grid size of 34.8 million nodes for the entire solution domain was created to compare the Spalart-Allmaras (SA) and DES turbulence models. The study found that DES results showed limited improvements in BVI predictions due to the unsatisfactory grid resolution. It suggested that further spatial and temporal refinement was required to access the fully potential of the DES method for rotor flows.

More recently, the Lattice-Boltzmann Method (LBM), an another branch of CFD method that solves the Boltzmann equation instead of the Euler or Navier-Stokes equations for numerical simulations of unsteady turbulent flows, has been used for helicopter rotor flows. For example, Romani *et al.* [25, 26] used PowerFLOW (a Lattice-Boltzmann/Very-Large-Eddy-Simulation (LB/VLES) based CFD solver) to calculate the flowfield of HART-II baseline configuration and full-scaled S-76 rotor. As shown in Figure 1.5, the scale-resolving characteristics of the LB/VLES method were demonstrated since many turbulence scales were well resolved in the advancing rotor side and downstream of the hub, and the amplitudes and phases of blade-vortex interaction behavior were well captured.

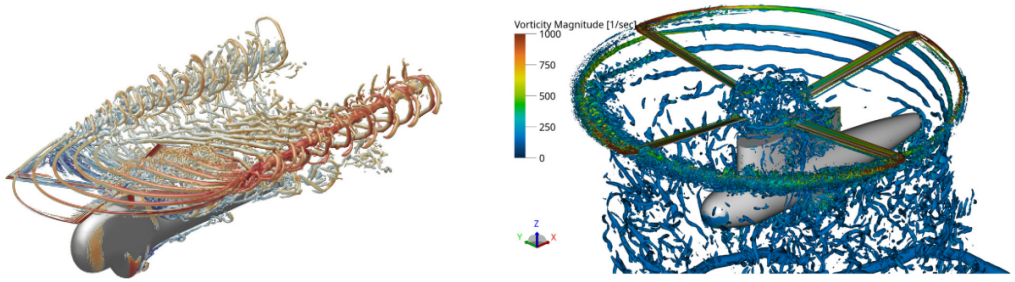

(a) *Wake structures of HART-II rotor baseline configuration [25]*

(b) *Wake structures of S-76 rotor in low speed forward flight condition [26]*

Figure 1.5: *Rotor wake visualization for helicopter rotor calculated by LBM/VLES method.*

Despite the fact that such approaches can yield very detailed rotor wake structures

and representative blade-vortex interactions, computational consumption increased significantly due to a large number of cells in the solution domain required for the simulation. This is a major constraint for practical engineering applications.

Grid Refinement Techniques In general, grid refinement is a class of techniques to reduce the error in solving partial differential equations (PDEs) by increasing the computational grid density in the region of interest. Depending on the way of refinement, these techniques fall into two categories: h-refinement and r-refinement. Furthermore, if these methods run automatically with the solution process, they result in the h-adaptive and r-adaptive.

The most extensively developed and widely used of these are h-refinement approaches, such as the AMR techniques, which locally refine the initially mesh by adding new grid points. The strategy for doing so is usually driven by a priori defined regions (shock positions, wake regions [27], ...) or a posteriori computed solutions (physical criteria [28, 29], error estimates of solutions [28], ...). So far, promising results were obtained through using some of the h-refinement approaches to capture the wake vortices in the simulation of helicopter rotor flows [21,22,30]. Despite a good track record in computation, there are some issues in the implementation and application of such methods. For instance, the additional grid points created during the refinement process constantly change the sparsity structure of the various matrices used in the calculation. For this reason, complex and evolving data structures are required to describe the mesh and its connectivity. In addition, the inclusion of newly generated grids leads to a decrease in computational efficiency.

r-refinement, also known as grid redistribution method, is an alternative procedure that maintains a fixed mesh topology and number of grid points in a constant connectivity structure and concentrates them in the desired area. A distinct advantage of this method is that the fixed grid points and topology retain the initial mesh decomposition operations, which is advantageous for parallel processes and computational efficiency. Additionally, the unchanged sparsity structures of matrices simplified the r-refinement approaches as there is no need to keep track of the node points with any form of nested data structure. However, the r-refinement method also gives rise to some new problems. For example, the refinement procedure is less robust than h-refinement due to the additional consideration of the orthogonality and smoothness of the grid. Moreover, although various methods of r-refinement have been proposed, almost all of them consider at most a two-dimensional (2D) refinement [31]. For these reasons, only a few r-refinement studies have been used for the simulation of helicopter rotor flows [32].

High-Order Schemes Practically, a numerical scheme could be considered as "high-order" if the solution error e in the functional approximation is proportional to the n-th ($n \geq 3$) power of mesh size h since most practically used CFD solvers in the aerospace community are second-order spatial accuracy [33, 34]. High-order schemes allow approximating the PDEs more accurately and possess superior wave propagation properties than lower-order schemes. When it comes to helicopter rotor flows, this could be translated to their capability of preserving blade tip vortices over long wake ages with less numerical dissipation. In addition, high-order schemes are less expensive than lower-order ones to achieve the same level of accuracy even though more complicated

operations are required for each degree of freedom (DOF). Over the last decades, so numerous and diverse efforts have been contributed to developing high-order schemes that a detailed survey on this topic is far beyond the scope of the present work. Instead, this section aims to provide a brief review of the application of modern high-order spatial schemes for the problems of helicopter rotor flow. More comprehensive surveys about high-order methods can be found in Ref [34–36].

The complex flow phenomena of helicopter rotor flow, such as dynamic stall, blade-vortex interaction, and shock-wave/boundary layer interaction, remain a major challenge for numerical approaches, especially the spatial discretization of convective terms, which is demonstrated to have a direct impact on vorticity preservation capability due to their dissipative nature. In general, high-order spatial schemes result in less numerical diffusion and therefore help to improve the spatial resolution to resolve the complex flow details. So far, two major classes of such schemes, including high-order Monotonic Upstream-centered Scheme for Conservative Law (MUSCL), high-order Essentially Non-Oscillatory (ENO)/ weighted ENO (WENO) schemes, become representative in numerical simulations of helicopter rotor flows. Table 1.2 outlines the high-order spatial schemes used by some well-known CFD codes for helicopter rotor analysis.

The MUSCL was initially constructed by B. Van Leer [53] for uniform grids within the framework of Finite-Volume (FV) Godunov-type schemes. The basic idea is to replace the piecewise uniform approximation of Godunov's method with a linear one to obtain the flow variables on the left and right sides of the cell face used to calculate the fluxes. For one-dimensional problems, the flow variables on the both sides of the cell interface can be written in the standard MUSCL form as

$$\begin{aligned}
\mathbf{F}_{j+1/2}^{L} &= \mathbf{F}_j + \left[\frac{k}{2}\left(\mathbf{F}_{j+1} - \mathbf{F}_j\right) + (1-k)\,\overrightarrow{\nabla}\mathbf{F}_j \cdot \overrightarrow{\mathbf{r}}_{f_j}\right] \\
\mathbf{F}_{j+1/2}^{R} &= \mathbf{F}_{j+1} + \left[\frac{k}{2}\left(\mathbf{F}_{j+1} - \mathbf{F}_j\right) + (1-k)\,\overrightarrow{\nabla}\mathbf{F}_{j+1} \cdot \overrightarrow{\mathbf{r}}_{f_{j+1}}\right]
\end{aligned} \tag{1.1}$$

where $\overrightarrow{\mathbf{r}}_{f_j}$ represents the vector from cell center j to face center $j+1/2$; $\mathbf{F}$ is the flow variables at the cell center or face center. This expression forms a one-parameter family known as the "k-schemes". By setting $k = 1/3$, a third-order MUSCL scheme is achieved, which becomes a popular choice for helicopter rotor flows [38, 40, 54, 55]. Such schemes were further extended to fourth-order spatial accuracy on the unstructured CFD method by adding a high-order correction obtained through successive differentiation to the right side of equation 1.1 in Ref [56]. Later, this fourth-order MUSCL scheme was implemented in the structured CFD method and demonstrated its capabilities in helicopter rotor flows [33].

The ENO/ WENO schemes are a class of high-order accurate Finite-Difference (FD) or FV numerical methods that preserve the non-oscillatory behavior in the vicinity of the discontinuity by using an adaptive local stencil to improve the resolution in the smooth region. The ENO schemes adaptively choose the smoothest stencil for approximation and reconstruction. In contrast, the WENO schemes extended the ENO schemes by replacing the stencil selection with a weighted combination associated with each candidate stencil, resulting in a smoother solution with better convergence properties. Since the first WENO scheme with three-order spatial accuracy was proposed by X.

Table 1.2: *Summary of high-order spatial schemes used in some well-known CFD codes for helicopter rotor flows*

CFD code	Organization	Grid type	Discretization method	High-order spatial scheme
HMB3	University of Glasgow	Structured	Finite volume	3^{rd}-order MUSCL [37, 38] 4^{th}-order MUSCL [33, 39]
CLORNS	Nanjing University of Aeronautics and Astronautics	Structured	Finite volume	3^{rd}-order MUSCL [40] 5^{th}-order WENO-Z [40]
OVERTURNS	University of Maryland	Structured	Finite difference	3^{rd}-order MUSCL [41, 42] 5^{th}-order WENO-M [43] 5^{th}-order CRWENO [42, 43]
OVERFLOW	NASA Langley	Structured	Finite difference	5^{th}-order WENO-JS [44] 4^{th}-order central difference [45] 6^{th}-order central difference [21]
FLOWer	DLR	Structured	Finite volume	5^{th}-order WENO-JS [46] 5^{th}-order CRWENO [47] 5^{th}-order WENO-Z [48, 49] 6^{th}-order WENO [50]
KFLOW	Konkuk University	Structured	Finite volume	5^{th}-order WENO-JS [51, 52]

Liu *et al.* [57], numerous studies have emerged for developing the WENO schemes. For example, G.S. Jiang and C.W. Shu [58] improved the WENO scheme to fifth-order accuracy by introducing a novel approach to smoothness measurement, resulting in the WENO-JS scheme. R. Borges *et al.* [59] proposed a new high-order smoothness indicator that further extended the WENO-JS scheme, providing the WENO-Z scheme, a new fifth-order WENO scheme with less dissipation and higher resolution. D. Ghosh *et al.* [43] used a solution-dependent combination of lower-order compact schemes to construct a fifth-order Compact-Reconstruction WENO (CRWENO) scheme with lower absolute errors and higher spectral resolution than the same order WENO schemes.

Vorticity Confinement Methods An alternative to the previously reviewed approaches based on CFD techniques is the vorticity confinement (VC) method proposed by Steinhoff and co-workers [60–63]. The VC is a concept that allows preventing a vortex from being inordinate diffusion by adding a particular designed anti-diffusion term into the standard Euler/Navier-Stokes equations. It has proved effective in simulating vortex-dominated flows, especially for cases without satisfactory mesh sizes. Currently, two formulations of VC methods have been developed and briefly referred to as VC1 [61] and VC2 [63].

In the first vorticity confinement (VC1) scheme, the VC term is derived from the first derivative of velocity. It transports vorticity in the direction of increasing vorticity magnitude gradient, counteracting the spreading effect due to the numerical dissipation. Over the past decades, the VC1 formulation became attractive in the simulation of vortex-dominated flows due to its algorithm simplicity and efficiency, especially for helicopter rotor flows. For instance, Steinhoff *et al.* [60] first applied the VC1 to a hovering HELIX I rotor flows and received a promising result. M. Biava and L. Vigevano [64] investigated the variations of confinement parameter on thrust coefficient for Onera 7A four-bladed rotor flows in both hover and forward flight. Even though the VC1 model was widely adopted, it suffers from two disadvantages. The first is related to a difficulty in the theoretical analysis of its properties, the singularity of VC1 term at the vortex center. The second concerns the conservation of the governing equations while using the VC1 term.

In order to correct the drawback of the VC1, the second vorticity confinement (VC2) formulation was later introduced [63]. The VC2 formulation is derived from the second derivative of velocity with no singular at the vortex core and with an exact conservative expression, which allows more detailed analytical investigations on its properties [65, 66], and makes it much easy to extend to higher-order schemes [67–69]. In recent years, the capabilities of VC2 formulation and its higher-order schemes on vorticity preservation and computational efficiency were well demonstrated from some studies [70–72] carried out in helicopter rotor flows.

Initially, the VC1 method was developed for incompressible flows. After several attempts [73, 74], G. Hu *et al.* [75] presented a more stable VC correction for compressible simulations by interpreting Steinhoff's VC1 formulation as a body force term and adding to both the momentum and energy equations. However, additional studies [65, 76] found that far better results could be obtained when the VC term was removed from the energy conservation equation. For this reason, M. Costes [65] suggested that the contributions of the VC term would only be treated as purely numerical

corrections to the momentum conservation equation rather than physical source terms. On this basis, the compressible VC1 and VC2 formulations were successfully applied to a wide range of cases.

Besides the compressible extensions of the VC formulations, another primary challenge is the determination of the confinement parameter ε, which controls the magnitude of the negative diffusion in the vorticity confinement, since a mistake in the choice of ε would result in the non-physical solutions and affect the stability of numerical simulation. To maintain dimensional consistency with the other conservation equation terms, three potential scale confinement parameters has been derived by R. Lohner *et al.* [77] through the dimensional analysis to ensure its dimension of velocity. M. Robinson [78] proposed a scaling expression based on the helicity by extending the Lohner's work. N. Butsuntorn and A. Jameson [79] further extended the helicity formulation of Robinson by including a non-dimensional scaling parameter based on the local mesh size. In most studies, the ε value comes from a trial and error procedure, which is less efficient. Several attempts have been put forward to remove the empiricism of confinement parameter selection. M. Costes and G. Kowani [65, 80] derived a dynamic confinement parameter related to the local vorticity. S. Hahn and G. Iaccarino [81] introduced a new adaptive VC parameter related to the difference between central and upwind discretisation of the convection terms. Nonetheless, this problem is still not completely resolved due to non-conservation of the VC2 scheme introduced by the ε value varying in space.

In spite of the number of researches employing VC to balance the excessive diffusion of vortical flows, there still remains an intrinsic issue. In most of these studies, the non-zero vorticity magnitude was used as the factor for vortex identification. It means that the vorticity confinement term was computed at each point in solution domain where the vorticity magnitude was not equal to zero. However, using vorticity magnitude to define a vortex structure is not adequate. It will not provide the correct results in the areas where the vorticity magnitude is non-zero but there is no vortex, like in the boundary layer, for instance. To alleviate this problem, R. Boisard and co-workers [71] used the Q criteria to avoid the application of over-confinement inside the boundary layer. Feder *et al.* [82] employed the λ_2 criterion as a limiter to restrict the vortices region in tracking the tip vortex of NACA0012 wing. M. Mohseni [83] introduced a class of hybrid methods that combine four different vortex feature detection approaches with the VC1 method and evaluated the performance of the hybrid techniques on the computational precision and efficiency with a 2D stationary single vortex.

1.2.2 Rotor Noise Prediction Approaches

Computational Aeroacoustics (CAA) is a multidisciplinary field that aims to analyze aerodynamically generated noise through a combination of numerical methods and aeroacoustics. In general, CAA can be classified into two categories: direct and hybrid methods [84]. Direct aeroacoustic methods solve the sound field directly from the governing equation of CFD. However, the underlying physics of the complex flow environment caused by helicopter rotors prevents direct aeroacoustic approaches from predicting the noise generated by helicopter rotors due to the dramatic computational expenses. In contrast, hybrid methods that separate the noise source computation and noise propagation have been able to effectively predict the rotor noise and gained pop-

ularity in helicopter rotor noise prediction.

In the hybrid method, the noise source is calculated by the CFD method described above, while noise propagation is solved by the acoustic method. There are two typical acoustic propagation methods: the differential methods and the integral methods. Differential methods, also known as linearized equations, include two widespread formulations, Linearized Euler Equations (LEE) [85–87] and Acoustic Perturbation Equations (APE) [88]. In principle, both LEE and APE methods are still time-dependent PDE systems. Furthermore, particular treatment should be considered for the discretization schemes to avoid dispersion and dissipation issues. Therefore, it is less preferred than integral methods due to their much higher computational time and resource demand for helicopter rotor noise prediction.

In integral methods, the Kirchhoff method [89,90], the Impermeable Surface Ffowcs Williams-Hawkings (IS-FWH) equation [91–93], and the Penetrable Surface Ffowcs Williams-Hawkings (PS-FWH) equation [25, 94] are the three most representative approaches. The IS-FWH equation is based on Lighthill's acoustic analogy [95]. It allows calculating the acoustic pressure signal at a far-field observer from the knowledge of the flow quantities on the blade surface and in the volume surrounding it. In this formulation, the noise may be interpreted as the sum of the thickness and loading source distributions over the control surface and a quadrupole nonlinear source distribution over the volume outside the control surface [1]. The IS-FWH equation is particularly suitable for predicting the subsonic rotor noise; however, when it comes to the transonic rotor noise prediction, the IS-FWH equation presents low-efficiency as the volume integration is time consuming and challenging to implement. The Kirchhoff method, which involves integration over a closed control surface around the source in the linear flow region, is more attractive in predicting transonic noise since no volume integration is required, but it is computationally demanding for the flow simulation, as the control surface must be placed sufficiently far from the source to ensure the linear wave propagation outside the control surface [96]. Furthermore, this approach does not provide any information about the noise generation mechanism. For these reasons, P.di Francescantonio [97] derived the PS-FWH equation and employed the Formulation 1A of Farassat [1], enabling the use of the FW-H equation on a penetrable control surface not required to be in the linear flow region. So far, the PS-FWH equation has proved to be successful in the prediction of helicopter impulsive noise, especially for the transonic rotor noise, because the nonlinear effects inside the control surface could be take into consideration.

In terms of the integral formulation, both the Retarded-Time and the Emission-Surface algorithms of the PS-FWH equation have been employed to rotor noise prediction. However, the Doppler singularity in the integral kernel prevents the Retarded-Time algorithm from obtaining a reliable prediction for transonic rotor noise. This problem may be bypassed via the adoption of the Emission-Surface algorithm, in which the Doppler term singularity no longer appears. Over the past decades, the Retarded-time algorithm has widely used for subsonic rotor noise prediction, while only few researches related to the Emission-Surface algorithm have been carried out for transonic rotor noise prediction, as the construction of the emission surface is a central difficulty. Only three emission surface construction methods are available in the literature: the Marching-Cube algorithm proposed by Brentner [98], the K-Algorithm devel-

oped by Ianniello [99–101] and the novel Emission Porous Surface (EPS) algorithm of Loiodice [102, 103].

The Marching-Cube algorithm is based on an iso-surface construction method, usually applied in computer graphics. By transforming the control surface discretization at each source time into a three-dimensional array, the emission surface modelling becomes equivalent to an iso-surface generation problem. L. Vendemini and L. Vigevano [104] described a detailed procedure of the Marching-Cube algorithm implementation. F. Farassat and K.S. Brentner [105] carried out the far-field approximation and the Marching-Cube algorithm into the IS-FWH equation to calculate the supersonic quadrupole noise. Ianniello instead proposed a different algorithm, known as the K-Algorithm, to construct the emission surface. Through a particular classification of the retarded spanwise stations and a data-adaptive procedure, the K-Algorithm is able to achieve an accurate emission surface reconstruction. Ref [106] gives a detailed description of the K-Algorithm and proposes the Emission-Surface based PS-FWH algorithm, which combines the K-Algorithm based Emission-Surface formulation with PS-FWH equation, to predict the UH-1H rotor HSI noise. Another recent Emission-Surface construction approach, which employs bifurcation analysis and an improved Retarded-Time algorithm, is developed by Loiodice *et al.* [102] and validated in Ref [103].

1.3 Research Objective

Accurate modeling of helicopter rotor aerodynamics and aeroacoustics remains challenging, as such rotors typically operate in highly unsteady flows, with rotating blades interacting with strongly non-uniform and turbulent flows. On the one hand, since the rotor vortical wake is among the most complex fluid dynamic structures in the helicopter unsteady flow field, the simulation of phenomena related to rotor wake, such as blade-vortex interaction, represents a major challenge. On the other hand, due to the distinct noise propagation mechanism, modeling impulsive rotor noise, such as blade-vortex interaction noise and high-speed impulsive noise, contributes to an additional challenge. For these reasons, developing a practical simulation framework that can effectively resolve most of the interested flow phenomena and accurately predict the annoying impulsive noise are essential for supporting the design process of the helicopter rotor.

Regarding to helicopter rotor aerodynamics, although the analytical, semi-empirical, and low-fidelity numerical approaches can quickly provide results suitable for performance analysis, they are poorly predictive as these models are insufficient to fully account for the complex flow phenomena described above. In contrast, the high-fidelity CFD simulations have gained popularity due to their capability of resolving most phenomena of interest. However, there is an inherent problem that those vortex features can be prematurely deformed and dissipated due to excessive numerical diffusion in the solution algorithm. This makes the employment of such techniques unsatisfactory.

From previous research works, it is learnt that four major classes of numerical methods, including SRS, high-order spatial schemes, vorticity confinement method, and grid refinement techniques, have emerged to help improve the capability of preserving vortices in CFD. However, even though these methods have shown significant improvements in vorticity preservation, some of them are often prohibitive for industrial ap-

plications due to the substantial computational time and resources. For example, SRS methods can provide a more detailed description of vortices but require large grid systems to exploit the full potential of this technique. Although the high-order spatial schemes are capable of avoiding excessive dissipation of the vortical structure with appropriate grid densities, the computation of high-order derivatives or the construction of stencils may result in additional computational costs. Regarding the grid refinement techniques, AMR, the most representative method for grid refinement, is also computationally expensive because of the additional grid points created in the refined region. On the contrary, the vorticity confinement and r-refinement methods present potentially advantageous computational efficiency for vorticity preservation since the grid system could be maintained at a moderate level without increasing the number of grid points in the region of interest. Therefore, this thesis pays special attention to these two efficient vorticity preservation techniques.

In the vorticity confinement method, previous studies suggest that the VC2 formulation performs better than the VC1 formulation, as the main shortcomings of the original VC1 have been corrected. Current research in VC2 formulation has focused on the extension of higher-order schemes. Although these studies applied the Q-criterion to avoid the application of confinement inside the boundary, further investigations are required to present the benefits of such treatment explicitly. Furthermore, it is necessary to systematically evaluate the performance of the VC2 formulation coupled with different vortex feature detection methods in three-dimensional (3D) vortex-dominated flows, particularly in helicopter rotor flows.

In previous studies, only some works on r-refinement techniques have been carried out for helicopter rotor flows due to their poor robustness and high complexity. Moreover, most of the r-refinement methods were proposed for 2D problems. For this reason, exploiting the 3D r-refinement method for helicopter rotor flows is meaningful.

In terms of helicopter rotor aeroacoustics, the subsonic rotor noise can be well predicted using the Retarded-Time-based IS-FWH equation. However, when it comes to transonic rotor noise, although the introduction of the PS-FWH equation is able to improve the predicted results, the inherent issue of Doppler term singularity of Retarded-Time algorithm leads to an unreliable solution, particularly when blade tip Mach number $M_T \geq 0.90$. In contrast, the Emission-Surface-based PS-FWH is ideal for predicting transonic rotor noise as the Doppler term singularity no longer appears. For this reason, applying the Emission-Surface-based PS-FWH equation is required to obtain reliable results for transonic rotor noise.

In light of these, the first objective of the present thesis is to construct a practical simulation framework for helicopter rotor aerodynamics and aeroacoustics that is able to simulate the complex flow phenomena around the rotor blades, such as blade-vortex interaction, and predict the rotor impulsive noise, including BVI noise and HSI noise. Specifically, the CFD solver ROSITA is coupled to a novel acoustic code capable of predicting BVI and HSI noise. The second objective is to assess the vortex feature-based second vorticity confinement model in 3D vortex-dominated flows, particularly helicopter rotor flows. The third objective is to develop a 3D r-refinement method and to explore its application to helicopter rotor flow.

1.4 Thesis Organization

In order to guide the reader through the remainder of this thesis, the organization of the subsequent chapters is briefly described below:

- **Chapter 2:** Introduces a computational framework primarily based on the coupling between the Navier-Stokes equations and the FW-H acoustic analogy for helicopter aerodynamic and aeroacoustic investigations. Firstly, a short description of CFD solver ROSITA is given. Then, mathematical and numerical formulations for both subsonic and transonic/supersonic rotor noise prediction are briefly derived. To numerically implement the transonic/supersonic formulations, the key procedure of emission surface construction is realized by the Marching-Cube algorithm. On this basis, the whole process of implementing the acoustic formulations is programmed as a numerical acoustic solver, which is able to handle both subsonic and transonic/supersonic rotor noise prediction. Afterward the details of the connection between CFD solver and acoustic solver are outlined. Finally, an improved high-efficiency rotor trim method is detailed.
- **Chapter 3:** Validates the simulation framework in Chapter 2. The validation work starts from each component of the simulation framework. An assessment of the Marching-Cube algorithm in emission surface construction is first performed. The Retarded-Time and Emission-Surface integral formulations are then verified by comparison with the analytical solutions. Next, the capability of the newly developed acoustic solver is validated by comparing to well-established acoustic solver solutions. Afterward, three well-documented rotor cases are used to validate the proposed rotor trim method. Finally, the integrated simulation framework is evaluated with HSI and BVI noise predictions.
- **Chapter 4:** Introduces a locally normalized vortex feature-based second vorticity confinement (VC2) model to improve the vortex resolution in aerodynamic wakes with a moderate computational cost. Systematically assessing such methods in 3D vortex-dominated flows reveals the necessity of coupling the vortex feature detection methods with the original VC2 formulation. In addition, the performances of these methods in helicopter rotor aerodynamics and aeroacoustic prediction are well demonstrated.
- **Chapter 5:** Explores the application of 3D r-refinement to helicopter rotor flows. First, Knupp's Jacobian-weighted elliptic mesh generation method is presented, and then, its extension to 3D problems is derived. Afterward, the preliminary validations for both 2D and 3D Jacobian-weighted elliptic methods are performed via some practical test examples.
- **Chapter 6:** Presents the conclusions and recommendations for future research.

CHAPTER 2

Helicopter Rotor Aerodynamic and Aeroacoustic Simulation Framework

This chapter describes a computational framework primarily based on the coupling between the Navier-Stokes equations and the FW-H acoustic analogy for helicopter aerodynamic and aeroacoustic investigations in this study. Firstly, a multi-block structured RANS solver ROSITA (Rotorcraft Software Italy), which is adopted to compute the near-field flow data for aerodynamic and aeroacoustic predictions, is briefly illustrated in *Section 2.1*. Secondly, in *Section 2.2*, the FW-H acoustic analogy, a common approach used to calculate far-field noise propagation for the flow solution provided by the Navier-Stokes equations, is detailed. Its integral formulations for both subsonic and trans/supersonic noise sources are presented, along with a description of the numerical implementations in the newly developed in-house acoustic code ROCAAP (Rotorcraft Code for AeroAcoustic Prediction). Afterwards a strategy to connect the CFD and acoustic approaches is proposed in *Section 2.3*. Finally, *Section 2.4* elaborates a high-efficiency trim approach adopted to assess the performance of the helicopter main rotor in forwarding flight accurately.

2.1 ROSITA CFD Solver

All flow simulations in this thesis are performed using the ROSITA solver, an in-house, multi-block, structured RANS solver [107]. It solves the Euler/Navier-Stokes equations in overset grid systems of moving multi-block grids. The one-equation SA turbulence model is coupled with RANS equations to model the turbulent behavior of the flow. Furthermore, the governing equations are formulated in terms of the absolute velocity, expressed in a relative frame of reference frame linked to each component grid to simplify the flow field solution in the overset grid system. The finite-volume formulations

could be written as:

$$\frac{\partial}{\partial t}\oint_{V_{ijk}} \mathbf{W}dV + \int_{S_{ijk}} (\mathbf{F_c}\cdot\mathbf{n} - \mathbf{v}\cdot\mathbf{n}\mathbf{W})dS - \int_{S_{ijk}} \mathbf{F_d}\cdot\mathbf{n}dS = \oint_{V_{ijk}} \mathbf{F_s}dV \tag{2.1}$$

with $\mathbf{W} = [\rho, \rho u, \rho v, \rho w, \rho e^t]^T$ denotes the vector of conservative variables inside the flow domain, $\mathbf{n}$ is the outward normal unit vector, $\mathbf{v}$ is the entrainment velocity vector. The expressions, $\mathbf{F_c}$ and $\mathbf{F_d}$, represent the convective flux tensor and diffusive flux tensor, respectively. V is the cell volume and S is the cell surface, $\mathbf{F_s}$ stands for the source term due to the movement of the relative reference frame.

In ROSITA, the space discretization leads to a system of ordinary differential equations for the rate of change of the conservative flow variables associated with the centers of the cell volumes, the equation (2.1) then reads:

$$\frac{d}{dt}(V\mathbf{W})_{ijk} + \mathbf{R}_{ijk} = 0 \tag{2.2}$$

where $\mathbf{R}_{ijk}$ stands for the flux balance across surface S_{ijk} of the hexahedral cell (i, j, k). The flux balance can be written as:

$$\mathbf{R}_{ijk} = (\mathbf{Q_c})_{ijk} - (\mathbf{Q_d})_{ijk} - (\mathbf{F_s})_{ijk} \tag{2.3}$$

where $(\mathbf{Q_c})_{ijk}$ is the convective flux balance (convective and pressure effects), $(\mathbf{Q_d})_{ijk}$ is the diffusive flux balance (viscous effects), $(\mathbf{F_s})_{ijk}$ is the source terms. The convective flux is approximated by the use of Roe-MUSCL 2nd-order discretization with a modified version of Van Albada limiter introduced by Venkatakrishnan [108]. The diffusive flux is calculated by a standard second-order central discretization; the components of stress tensor are discretized by the application of the Gauss theorem.

The time advancement is performed with a implicit dual-time method; the equation (2.2) can be replaced by an implicit 2nd-order backward differential formula:

$$\frac{3(V\mathbf{W})^{n+1}_{ijk} - 4(V\mathbf{W})^{n}_{ijk} + (V\mathbf{W})^{n-1}_{ijk}}{2\Delta t} + \mathbf{R}^{n+1}_{ijk} = 0 \tag{2.4}$$

where the state vector $\mathbf{W}^{n+1}_{ijk}$ is solved by sub-iterations in pseudo-time at each physical time step Δt, In sub-iteration step, a Generalized Conjugate Gradient (GCG) method, in conjunction with a Block Incomplete Lower-Upper (BILU) preconditioner, is implemented.

The moving Chimera technique based on the modified Chesshire and Henshaw algorithm [109] is used to compute the connectivity between the component grids. The domain boundaries with solid wall conditions are firstly identified, and all points in overlapping grids that fall close to these boundaries are marked as holes (seed points). Then, an iterative algorithm identifies the donor and fringe points and lets hole points grow from the seeds until they fill the regions outside the computational domain entirely. In addition, the Oct-tree and alternating digital tree data structure are adopted to speed up the donor searching process.

2.2 Aeroacoustic Approaches

This section describes the FW-H acoustic analogy used throughout this thesis to model the aerodynamically generated sound of rotors, with the flow solution on the control

surface provided by CFD computations. Two different integral formulations of the FW-H equation are adopted in this thesis. The first is the Retarded-time formulation, which is robust and efficient for subsonic conditions, and the second is the Emission-Surface formulation, which is perfectly suitable for transonic and supersonic noise source cases. In this section, a brief derivation of the FW-H equation and its two different integral formulations are presented first. Then, the numerical implementations are described, including the Marching-Cube (MC) algorithm to construct the retarded domain.

2.2.1 The Ffowcs Williams-Hawkings (FW-H) Equation

The Ffowcs Williams-Hawkings [95] (FW-H) equation is the most appropriate theoretical support for understanding the mechanisms of aerodynamically sound generation from bodies in complex motion [110], see Figure 2.1. Since the aeroacoustic and aerodynamic problems are built upon the same fundamental equations of mass and momentum conservation of a compressible fluid, the FW-H equation may be derived from the Navier-Stokes equations by assuming that the fluid inside the moving surfaces has the same states as the undisturbed medium. However, this assumption makes the flow parameters across the moving surfaces discontinuity. In 1969, Ffowcs Williams and Hawkings [95] firstly introduced the generalized function theory to address the derivatives of discontinuous functions in Navier-Stokes equations. After making use of the generalized functions, the continuity and momentum equations could be expressed as

$$\frac{\overline{\partial}\rho}{\partial t} + \frac{\overline{\partial}}{\partial x_j}(\rho u_j) = \rho_0 u_n \delta(f) + (\rho - \rho_0)(u_n - v_n)\delta(f) \tag{2.5a}$$

$$\frac{\overline{\partial}}{\partial t}(\rho u_i) + \frac{\overline{\partial}}{\partial x_j}(P_{ij} + \rho u_i u_j) = P'_{ij} n_j \delta(f) + \rho u_i (u_n - v_n)\delta(f) \tag{2.5b}$$

where $\overline{\partial}/\partial t$ and $\overline{\partial}/\partial x_j$ represent generalized derivatives; ρ is the fluid density and ρ_0 is the density of the undisturbed medium; the function f=0 stands for an integration control surface that encloses the noise generation region, see Figure 2.1; u_i and v_i are the local fluid and surface velocity components, respectively; $n_j = \partial f/\partial x_j$ is the component of the unit normal outwards to the control surface; $\delta(f)$ is the Dirac delta function; $P_{ij} = (p - p_0)\delta_{ij} - \tau_{ij}$ is the compressive stress tensor with τ_{ij} is viscous stress tensor, $P'_{ij} = (P_{ij} - P_0)\delta_{ij}$ is the pertubation stress tensor in each direction, δ_{ij} is the kronecker's delta.

Equations (2.5a) and (2.5b) can be rearranged into an inhomogeneous wave equation with two surface source terms and a volume source term by substracting the generalized partial derivative of (2.5b) with respect to the space variable x_i from the generalized time partial derivative of (2.5a), then give

$$\begin{aligned} \overline{\Box}^2 p' = & \frac{\partial}{\partial t}\{[\rho_0 v_n + \rho(u_n - v_n)]\delta(f)\} \\ & - \frac{\partial}{\partial x_i}\{[P'_{ij} n_j + \rho u_i (u_n - v_n)]\delta(f)\} \\ & + \frac{\overline{\partial}^2}{\partial x_i \partial x_j}[T_{ij} H(f)] \end{aligned} \tag{2.6}$$

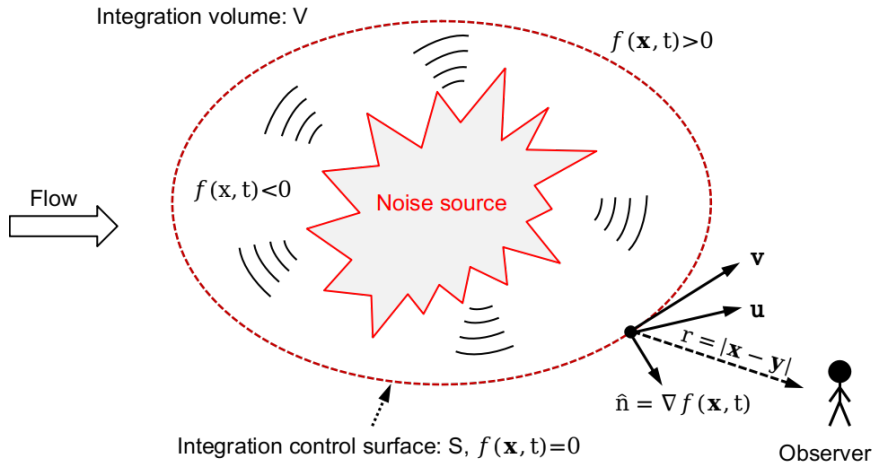

Figure 2.1: *Problem description of the FW-H acoustic analogy.*

which is the PS-FWH equation, where the generalized wave operator is represented by $\overline{\Box}^2 = (1/c_0^2)(\overline{\partial}^2/\partial t^2) - \overline{\nabla}^2$; $p' = p - p_0$ is the acoustic pressure; $T_{ij} = \rho u_i u_j + P_{ij} - c_0^2(\rho - \rho_0)$ is the Lighthill's equivalent stress tensor; $H(f)$ is the Heaviside function. The three terms on the right-hand side stand for monopole thickness, dipole loading, and quadrupole contributions, respectively.

In this equation, an artificial penetrable control surface is required to enclose the noise source, as well as all non-negligible quadrupole contributions inside the surface. In such a way, the quadrupole source term in equation (2.6) can be omitted. Practically, the computational efficiency would be significantly increased as no volume integration is needed.

For the control surface S coinciding with a solid surface, the non-penetration condition (u_n = v_n) is required, the equation (2.6) can be rewritten as the IS-FWH equation

$$\begin{aligned}\overline{\Box}^2 p' = &\frac{\partial}{\partial t}\{[\rho_0 v_n]\delta(f)\} - \frac{\partial}{\partial x_i}\{[P'_{ij} n_j]\delta(f)\} \\ &+ \frac{\overline{\partial}^2}{\partial x_i \partial x_j}[T_{ij} H(f)]\end{aligned} \tag{2.7}$$

In this case all three source terms at the right-hand side have a explicit physical meaning. The monopole or thickness term models the noise due to the fluid passes over the body, the dipole or loading term represents the noise generated by the unsteady forces on the body surface, the quadrupole term includes all the non-linearities (e.g. shocks, vorticity, turbulence, etc.) in the volume outside the control surface (f>0). In practice, the quadrupole term is always neglected if the non-linear effects are not significant.

Through the use of the free-space Green's function ($\delta(g)/4\pi r$ with $g = t - \tau - r/c_0$ and $r = |\mathbf{x} - \mathbf{y}|$) with the generalized inhomogeneous wave equation (2.6), an integral representation of the FW-H equation can be obtained:

$$4\pi\Phi(\mathbf{x}, t) = \int_{-\infty}^{t}\int_{-\infty}^{\infty} Q(\mathbf{y}, \tau)\frac{\delta(g)}{r}\delta(f)d\mathbf{y}d\tau \tag{2.8}$$

with the generic variable is expressed by $\Phi(\mathbf{x}, t)$, the generic source strength is rep-

resented by $Q(\mathbf{y}, \tau)$, the observer and source space-time variables are denoted respectively by $(\mathbf{x}, t)$ and $(\mathbf{y}, \tau)$. The limits of the integral are given below:

$$\begin{aligned}\int \cdots \, d\mathbf{y} d\tau &= \int_{-\infty}^{t} \int_{\mathbb{R}^3} \cdots \, d\mathbf{y} d\tau \\ &= \int_{-\infty}^{t} \int_{-\infty}^{\infty} \int_{-\infty}^{\infty} \int_{-\infty}^{\infty} \cdots \, dy_1 dy_2 dy_3 d\tau\end{aligned} \tag{2.9}$$

Afterward, three different integral formulations (Retarded-Time, Collapsing-Sphere, and Emission-Surface) can be derived in terms of the way to integrate the two Dirac delta functions $\delta(g)$ and $\delta(f)$. This thesis discusses Retarded-Time and Emission-Surface formulations due to their excellent behavior in predicting the solutions for subsonic and transonic/supersonic noise sources, respectively.

2.2.2 Subsonic Noise Source Formulation

The Retarded-Time formulation performs well for a body surface moving in subsonic regime. By employing the variable transformations $(y_3, \tau) \rightarrow (f, g)$ on equation (2.8), the generic form of Retarded-Time formulation can be expressed as [1]

$$4\pi\Phi(\mathbf{x}, t) = \int_{f=0} \left[\frac{Q(\mathbf{y}, \tau)}{r|1 - M_r|} \right]_{ret} dS \tag{2.10}$$

where $|1 - M_r|$ is known as the Doppler factor, dS is an element area of the control surface f = 0, the subscript ret stands for the retarded time. Therefore, the Retarded-Time integral formulation for the PS-FWH equation may be derived along the line of Farassat's 1 formulation as [111]

$$4\pi p'(\mathbf{x}, t) = 4\pi p'_T(\mathbf{x}, t) + 4\pi p'_L(\mathbf{x}, t)$$

$$\begin{aligned}4\pi p'_T(\mathbf{x}, t) &= \frac{\partial}{\partial t} \int_S \left[\frac{\rho_0 u_n + (\rho - \rho_0)(u_n - v_n)}{r|1 - M_r|} \right]_{ret} dS \\ 4\pi p'_L(\mathbf{x}, t) &= \frac{1}{c_0} \frac{\partial}{\partial t} \int_S \left[\frac{P'_{nr} + \rho u_r (u_n - v_n)}{r|1 - M_r|} \right]_{ret} dS \\ &\quad + \int_S \left[\frac{P'_{nr} + \rho u_r (u_n - v_n)}{r^2|1 - M_r|} \right]_{ret} dS\end{aligned} \tag{2.11}$$

where $P'_{nr} = P'_{ij}\widehat{n}_j\widehat{r}_i$, $M_r = M_i\widehat{r}_i$ is the local Mach number of the control surface elements in the radiation direction at retarded time instants τ. $\widehat{r}_i = r_i/r$ is the components of the unit distance r from source to observer. Subscripts T and L represent the thickness and loading noise sources, respectively.

Furthermore, taking the observer time derivative inside the first integral of equation (2.11), a more efficient and accurate formulation named Farassat's Formulation 1A for the PS-FWH equation may be obtained [111]:

$$
\begin{aligned}
4\pi p'_T(\mathbf{x},t) &= \int_S \left[\frac{\rho_0(\dot{U}_n + U_{\dot{n}})}{r|1-M_r|^2}\right]_{ret} dS \\
&\quad + \int_S \left[\frac{\rho_0 U_n(r\dot{M}_r + c_0(M_r - {M_i}^2))}{r^2|1-M_r|^3}\right]_{ret} dS \\
4\pi p'_L(\mathbf{x},t) &= \frac{1}{c_0}\int_S \left[\frac{\dot{L}_r}{r|1-M_r|^2}\right]_{ret} dS \\
&\quad + \int_S \left[\frac{L_r - L_M}{r^2|1-M_r|^2}\right]_{ret} dS \\
&\quad + \frac{1}{c_0}\int_S \left[\frac{L_r(r\dot{M}_r + c_0(M_r - {M_i}^2))}{r^2|1-M_r|^3}\right]_{ret} dS
\end{aligned}
\tag{2.12}
$$

where

$$
\begin{aligned}
U_i &= u_j + [(\rho/\rho_0 - 1)](u_j - v_j) \\
L_i &= P'_{ij}\widehat{n}_j + \rho u_i(u_n - v_n)
\end{aligned}
$$

All other variables have been introduced previously.

Although the Farassat Formulation 1 and 1A have been widely used in the prediction of rotor noise, the Doppler singularity in the integral kernel prevents them from obtaining a reliable noise prediction for transonic/supersonic moving sources, their applications are restricted to body surfaces moving in subsonic regime. In practice, it is necessary to switch to the formulation that is able to deal with the problems of the high-speed noise source without suffering from the Doppler singularity.

2.2.3 Trans/Supersonic Noise Source Formulation

Since Farassat's Formulation 1 and 1A can only be used in subsonic noise sources due to the intrinsic limitation (Doppler Singularity) of the Retarded-Time formulation, the Emission-Surface formulation becomes a perfect alternative method that is able to avoid the effects of Doppler singularity by introducing a much less restrictive condition in the Doppler factor. Therefore, the Emission-Surface formulation is the appropriate method for solving the problems of trans/supersonic noise sources.

The Emission-Surface algorithm can be derived by using the variable transformations $(y_3, \tau) \rightarrow (F, g)$ with $F(\mathbf{y}; \mathbf{x}, t) = f(\mathbf{y}, t - r/c)$, the generic form of Emission-Surface algorithm can be written as [1]

$$
4\pi\Phi(\mathbf{x},t) = \int_{F=0} \left[\frac{Q(\mathbf{y},\tau)}{r\Lambda}\right]_{ret} d\Sigma \tag{2.13}
$$

where $\Lambda = \sqrt{1 - 2M_n cos\theta + M_n^2}$, $M_n = \mathbf{M}\cdot\mathbf{n}$ and $\theta = arccos(\mathbf{n}\cdot\mathbf{r})$ is the Doppler term; Σ stands for the emission surface, a collection of points in space-time that emit

signals reach the observer at the same observer time. Hence, the Emission-Surface integral formulaion for the PS-FWH equation is expressed as

$$
\begin{aligned}
4\pi p'_T(\mathbf{x},t) &= \frac{\partial}{\partial t}\int_\Sigma \left[\frac{\rho_0 u_n + (\rho-\rho_0)(u_n-v_n)}{r\Lambda}\right]_{ret} d\Sigma \\
4\pi p'_L(\mathbf{x},t) &= \frac{1}{c_0}\frac{\partial}{\partial t}\int_\Sigma \left[\frac{P'_{nr}+\rho u_r(u_n-v_n)}{r\Lambda}\right]_{ret} d\Sigma \\
&\quad + \int_\Sigma \left[\frac{P'_{nr}+\rho u_r(u_n-v_n)}{r^2\Lambda}\right]_{ret} d\Sigma
\end{aligned}
\tag{2.14}
$$

2.2.4 Numerical Implementations

Based on the approaches discussed above, an in-house acoustic code ROCAAP (ROtorcraft Code for AeroAcoustic Prediction) is developed with the FORTRAN 90/95 code for helicopter aeroacoustic problems. It is capable of running parallel on clusters based on Message Passing Interface (MPI). ROCAAP numerically solves the PS-FWH equation with the Retarded-Time and Emission-Surface algorithm for noise sources moving in subsonic, transonic, and supersonic regimes.

2.2.4.1 Retarded-Time Algorithm

In the Retarded-Time algorithm, the observer time t is selected in advance. Then the emission times τ at all source panels are readily obtained by solving the retarded time equation $\tau - t + r/c_0 = 0$ with the bisection method since there will be only one τ for every observer time t when the noise sources move at subsonic speed. Afterwards the integrands for each source panel are integrated at relevant emission times with the Midpoint quadrature integration method (equation (2.15)) and summed to yield the acoustic pressure for a given observer location $\mathbf{x}$ and time t.

$$
\begin{aligned}
4\pi p'(\mathbf{x},t) &= \frac{1}{c_0}\frac{\partial}{\partial t}\sum_{i=1}^{N_{quad}} \left[\frac{Q_1(\mathbf{y}_i, t-r_i/c_0)}{r_i|1-M_r|_i}\right]_{ret} \Delta S_i \\
&\quad + \sum_{i=1}^{N_{quad}} \left[\frac{Q_2(\mathbf{y}_i, t-r_i/c_0)}{r_i^2|1-M_r|_i}\right]_{ret} \Delta S_i
\end{aligned}
\tag{2.15}
$$

2.2.4.2 Emission-Surface Algorithm

For the Emission-Surface algorithm, the MC algorithm, which could find the multiple roots for retarded time equation and connect several disjoint pieces, is first applied with the PS-FWH equation to construct the emission surface Σ and perform the integration in equation (2.14).

The MC algorithm was initially developed in computer graphics to construct high-resolution isosurfaces from scalar volume datasets. Brentner [98] first adopted this method to construct the emission surface in the IS-FWH equation. The implementation of the MC algorithm in PS-FWH equation is displayed in Figure 2.2 and subsequently outlined as follows:

- **Step 1:** Discretize the control surface to a set of 3D cubes in the space-time domain, in which the surface is spatially parameterized in i and j direction, and the source time array is assigned to k direction.
- **Step 2:** Compute the observer time of each cube vertex via the Retarded-Time equation, $t = \tau + r(\mathbf{x}, \mathbf{y}, \tau)/c_0$ and mark each vertex as 0 or 1 through the comparison with respect to the given observer time. Result in a binary format for each cube by combining these labels in sequence from v1 to v8.
- **Step 3:** Convert the binary data to the decimal for identifying the intersected edges and the number of triangles at each cube from the modified look-up tables suggested by Montani [112].
- **Step 4:** Assemble the triangles in each cube by calculating the intersections in each edge with the linearly interpolation method.

This procedure is repeated for each observer time; a set of triangles constructs the emission surface. With the MC algorithm and the Midpoint quadrature integration method, the equation (2.14) can be rewritten as:

$$\begin{aligned} 4\pi p'(\mathbf{x}, t) = & \frac{1}{c_0}\frac{\partial}{\partial t}\sum_{i=1}^{N_{tri}}\left[\frac{Q_1(\mathbf{y}_i, t - r_i/c_0)}{r_i \Lambda_i}\right]_{ret}\Delta\Sigma_i \\ & + \sum_{i=1}^{N_{tri}}\left[\frac{Q_2(\mathbf{y}_i, t - r_i/c_0)}{r_i^2 \Lambda_i}\right]_{ret}\Delta\Sigma_i \end{aligned} \tag{2.16}$$

where the time derivative is calculated by a second-order finite difference over the observer time.

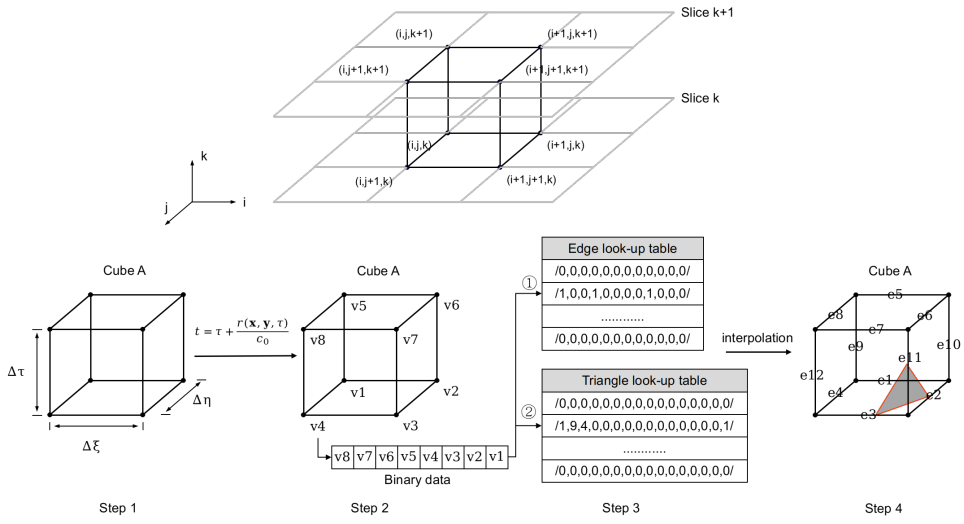

Figure 2.2: *The steps of the MC algorithm for the emission surface construction*

2.3 Connection of CFD Method and Acoustic Approach

Unlike other CFD/PS-FWH hybrid methods, the grid indices in an overset, multi-block grid system are disorderly distributed within each block, so that it is difficult to specify

a particular layer of the grid system as the control surface. To overcome this feature, a cylindrical permeable control surface, which should enclose most of the noise source, is automatically generated with minimal choices from the user, who needs to specify only simple geometrical parameters (radius, height, and grid dimensions). In order to quantify the dimension of the cylindrical control surface, an ordered pair S_{cs}, which evaluates how far the permeable control surface is from the blade surface, is considered as:

$$S_{cs} = (|\Delta y_r|/c, |\Delta x_t|/c) \tag{2.17}$$

where $|\Delta y_r|$ represents the maximum radial extension at the blade section center, $|\Delta x_t|$ represents the spanwise extension outward to the blade tip section, and c is the blade section chord, as sketched in Figure 2.3. It is defined that the circle collapses to the airfoil surface when $|\Delta y_r|/c = 0.5$: in this case, the noise prediction is provided by the IS-FWH equation.

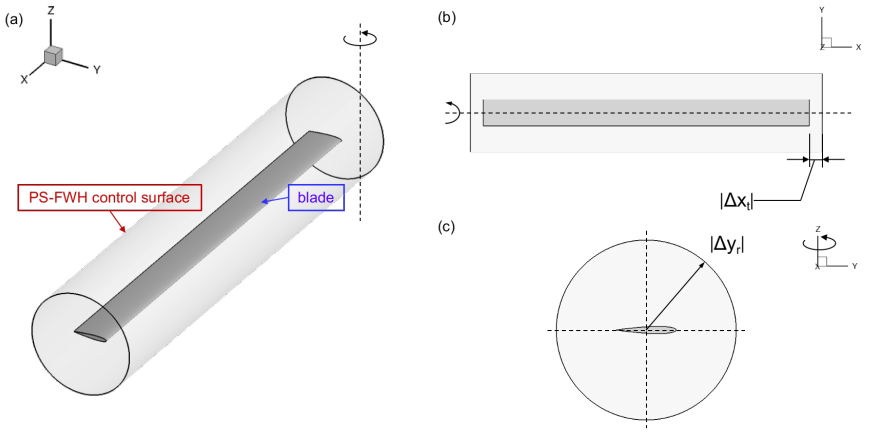

Figure 2.3: *Control surface arrangement from different views. a) isometric view; b) top view; c) side view*

An algorithm of extracting the control surface from the CFD overset, multi-block, structured grid system is presented, in which the Oct-tree search algorithm and a modified Chesshire and Henshaw algorithm [109] are used to detect the donor cells in the grid system and to interpolate the flow variables on the control surface.

The implementation of the control surface extraction algorithm within ROSITA is described by referring to a simple two-dimensional example (see Figure 2.4), consist of a cartesian CFD mesh (in red) and a circular control surface grid (in black).

The algorithm proceeds automatically, for a given number N_s of control surfaces, via four main steps. After completion, each of the N_s control surfaces cell contains the conservative flow variables required by noise prediction. An identification array `ICHIM_CS` is used to label each of the N_c CFD grid cell centroids. The algorithm is summarized as follows::

- **Step 1: Initialization:** The first step is to initialize the identification array `ICHIM_CS`. Considering all points P of the $n-th$ CFD grid ($1 < n < N_c$), `ICHIM_CS(P,n)` is set to `0`.

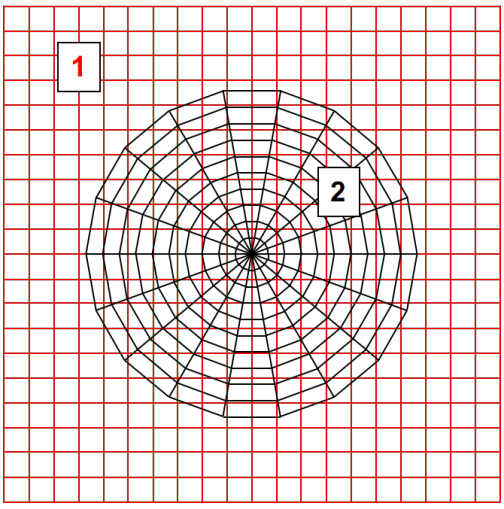

Figure 2.4: *A simple 2D grid system with control surface*

- **Step 2: Find parents:** Step 2 identifies the parent grids for $s-th$ control surface grid point Q; a parent grid is a CFD grid from which point Q may be interpolated. During the Step 2 a list of valid cells is produced for subsequent use by donor finding. At the end of this step, the entries in the identification array will be:

$$\texttt{ICHIM\_CS}(\texttt{P},\texttt{n}) = \begin{cases} 0, & \text{if point P is a } \textbf{normal point} \\ -\texttt{s}, & \text{if point P is a } \textbf{valid point} \text{ for the control surface s} \end{cases}$$

- **Step 3: Find donors:** Step 3 is finding the base donor point from the parent grids for the control surface grid interpolation. The valid points marked from the previous step are examined in sequence: for the 'target' points Q (see Figure 2.5), a test is made to check if a hexahedral cell of valid donor points exists so that the solution can be interpolated. In this step, the Oct-tree fast searching algorithm is implemented to speed up the process. At the end of this step, the entries in the identification array change to:

$$\texttt{ICHIM\_CS}(\texttt{P},\texttt{n}) = \begin{cases} 0, & \text{if point P is a } \textbf{normal point} \\ -\texttt{s}, & \text{if point P is a } \textbf{valid point} \\ \texttt{s}, & \text{if point P is a } \textbf{base donor point} \text{ due to control surface s} \end{cases}$$

- **Step 4: Promote points:** Step 4 promotes the left valid points to normal points. The final entries of the identification array is :

$$\texttt{ICHIM\_CS}(\texttt{P},\texttt{n}) = \begin{cases} 0, & \text{if point P is a } \textbf{normal point} \\ \texttt{s}, & \text{if point P is a } \textbf{base donor point} \text{ due to control surface s} \end{cases}$$

- **Step 5: Interpolation:** Step 5 is to interpolate the flow variables on the control surface with the base donor points marked from the previous steps. A trilinear interpolation is carried out to obtain the CFD data on the acoustic control surfaces for the PS-FWH equation.

Figure 2.6 presents a control surface extraction test for the two-bladed rotor in hover, the donor cells of the cylindrical control surfaces are shown.

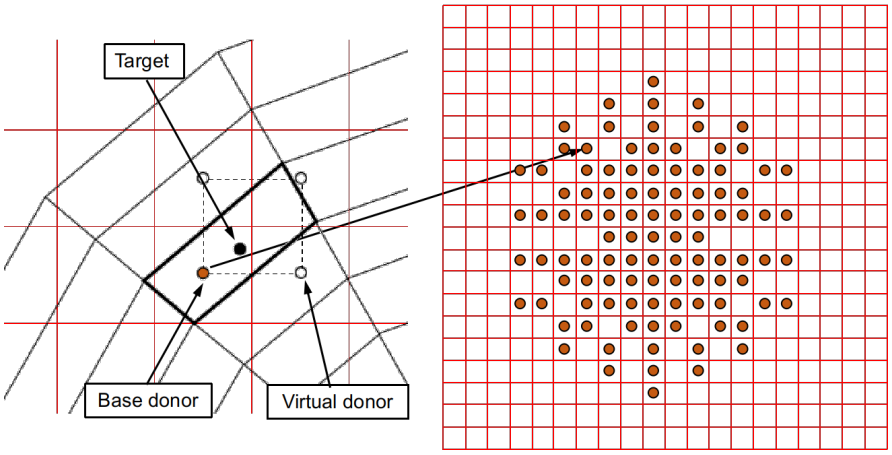

Figure 2.5: *Search donor points*

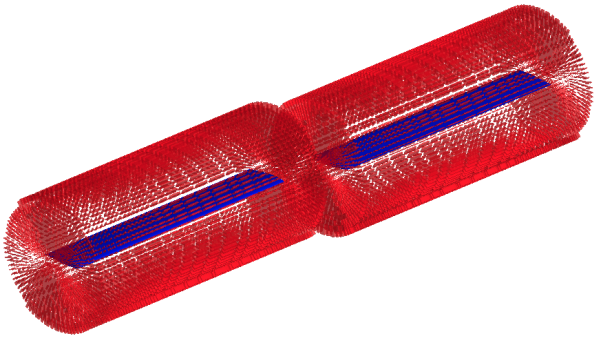

Figure 2.6: *The extraction algorithm applied to the two-bladed rotor (donor cells in red)*

2.4 High-Efficiency Helicopter Main Rotor Trim method

In the numerical simulations of helicopter rotor forward flight cases, since the nature of asymmetrical air-loads of the main rotor leads to undesired moments with respect to the rotor hub, the trimming process is required to correlate the predicted thrust and moments better with the target data. However, the simulation with the rotor control settings obtained from flight experiments or wind-tunnel tests always lead to an incompletely trimmed state. It is necessary to employ a trimming method to improve the accuracy of helicoptor rotor aerodynamics prediction.

In helicopter rotor analysis, the blade pitching, flapping and lead-lag motions are commonly described by the following Fourier series as a function of the azimuth angle ψ :

$$\begin{cases} \theta(\psi) = \theta_0 + \theta_{1c}\cos(\psi) + \theta_{1s}\sin(\psi) + ... \\ \beta(\psi) = \beta_0 + \beta_{1c}\cos(\psi) + \beta_{1s}\sin(\psi) + ... \\ \delta(\psi) = \delta_0 + \delta_{1c}\cos(\psi) + \delta_{1s}\sin(\psi) + ... \end{cases} \tag{2.18}$$

where the θ_0 is the collective pitch angle, β_0 is the blade coning angle. In the present study, only the first harmonic term is considered. In general, the blades are assumed to move 'rigidly', and the blade flapping and lead-lag motions are ignored. Therefore, the rotor trimming state is affected by three independent control settings: collective pitch angle θ_0, lateral cyclic pitch angle θ_{1c}, and longitudinal cyclic pitch angle θ_{1s} and the trim equations can be expressed as:

$$\begin{cases} C_T(\theta_0, \theta_{1c}, \theta_{1s}) = C_T^{target} \\ C_{Mx}(\theta_0, \theta_{1c}, \theta_{1s}) = 0.0 \\ C_{My}(\theta_0, \theta_{1c}, \theta_{1s}) = 0.0 \end{cases} \tag{2.19}$$

Recently, two methods have been employed for the rotor trim computation. The first approach is called the CFD based trim method, which applies the CFD method and the Newton-Raphson iteration method to calculate the trim variables. Although this method is proved to be effective and is commonly used in many studies [25,51,94,113], it shows the low efficiency as the high-fidelity solver has to be run three additional revolutions to compute the Jacobi matrix for each trim cycle. The second approach, which known as the delta trim method [114, 115], offers more efficiency way because the CFD solver used for computing the Jacobi matrix is replaced by a simplified aerodynamic model.

In this work, a multi-dimensional delta trim method is introduced to model the trimmed rotor in forwarding flight conditions. As illustrated in Figure.2.7, the trimming process consists of two stages. In the preliminary stage, the coarse grid system with coarse temporal resolution is used to calculate the low precision control settings. Subsequently, the accurate control angles of the fine grid with satisfactory temporal resolution can be determined at the accurate stage by using the low precision pitch angles as input. The delta trim method is composed of the ROSITA solver and the Blade Element Theory (BET) code. The full descriptions are given subsequently.

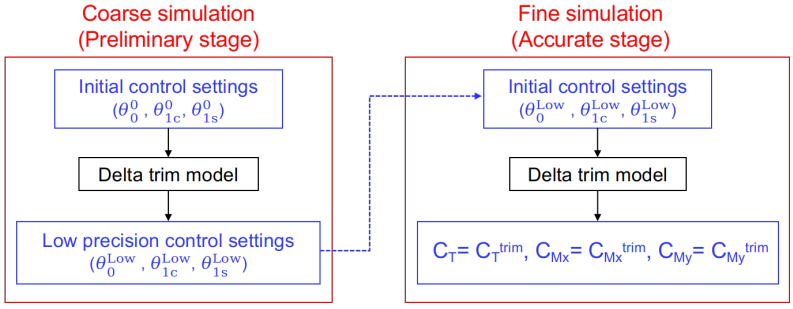

Figure 2.7: *The overview of the multi-dimensional trimming process*

2.4.1 Blade Element Theory

As known, the BET is a simplified aerodynamic model in helicopter rotor analysis. It is assumed that the sectional airloads at each blade element are produced by a two-dimensional airfoil. Rotor aerodynamic forces and moments can be obtained by integrating the airloads of each blade section over the spanwise direction and averaging the results over a rotor revolution. To account for the mutual interaction between adjacent blade elements, an induced inflow model is introduced to correct the angle of attack of each airfoil section. With these treatments, the BET code is able to evaluate the aerodynamic performance of rotor with a certain precision and high efficiency, which makes it favourable for calculating the Jacobian matrix in the trimming process. To illustrate this, a sketch of the BET model is presented in Figure 2.8, and a brief introduction follows.

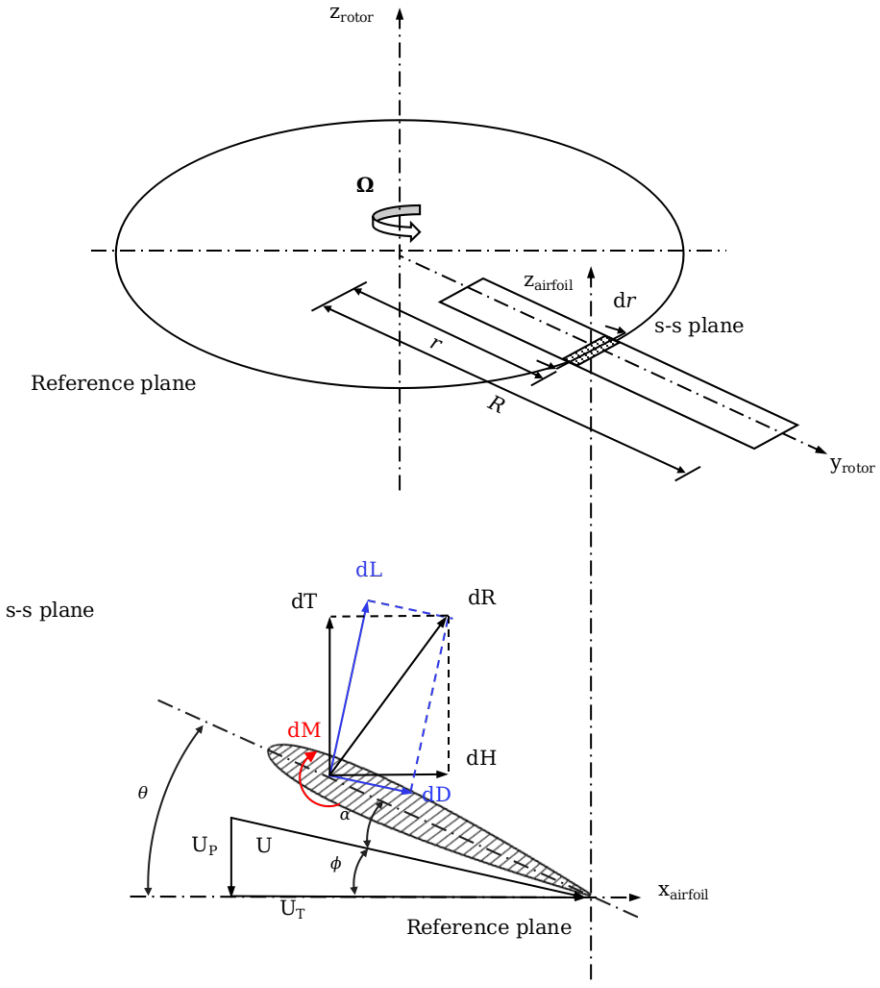

Figure 2.8: *Illustration of the blade element theory*

The elementary contributions to the blade lift dL and drag dD are written as

$$\begin{cases} dL = \frac{1}{2}\rho C_L({U_P}^2 + {U_T}^2)cdr \\ dD = \frac{1}{2}\rho C_D({U_P}^2 + {U_T}^2)cdr \end{cases} \tag{2.20}$$

where the lift and drag coefficients of the airfoil section, C_L and C_D, can be obtained through interpolation from a pre-prepared airfoil .C81 table or steady linearized aerodynamic theory. The inflow velocity components U_P and U_T are expressed by

$$\begin{cases} U_P = \Omega r + \mu\Omega R\sin\psi \\ U_T = \lambda\Omega R + r\frac{d\beta}{d\psi} + \mu\Omega R\sin\beta\ \cos\psi \end{cases} \tag{2.21}$$

Here, Ω represents the angular velocity, μ is the advanced ratio, R is the rotor radius, ψ is the azimuth angle, β is the flap angle, λ stands for the inflow ratio, which can be expressed as the sum of induced inflow ratio λ_i and climbing inflow ratio λ_c.

In this work, the Drees linear inflow model [116] is employed to calculate the induced inflow ratio

$$\begin{cases} \lambda_i = \lambda_0\left(1 + k_x\frac{r}{R}\cos\psi + k_y\frac{r}{R}\sin\psi\right) \\ \lambda_0 = \frac{C_T}{2\sqrt{\mu^2+\lambda^2}} \end{cases} \tag{2.22}$$

where the inflow coefficients k_x and k_y are defined by

$$\begin{cases} k_x = \frac{4}{3}\left((1-1.8\mu^2)\sqrt{1+\left(\frac{\lambda}{\mu}\right)^2} - \frac{\lambda}{\mu}\right) \\ k_y = -2\mu \end{cases} \tag{2.23}$$

The incremental thrust dT of each narrow blade element can be expressed as function of induced inflow angle ϕ by projecting the dL and dD to the direction perpendicular to the rotor disk plane.

$$\begin{cases} dT = dL\cos\phi - dD\sin\phi \\ \phi = \tan^{-1}(\frac{U_P}{U_T}) \end{cases} \tag{2.24}$$

By integrating dT over the rotor disk, the thrust T, the rolling moment M_x and the

pitching moment M_y will be

$$\begin{cases} T = \dfrac{N_b}{2\pi}\int_0^{2\pi}\int_0^R dT d\psi \\ M_x = \dfrac{N_b}{2\pi}\int_0^{2\pi}\int_0^R r\sin\psi\, dT d\psi \\ M_y = -\dfrac{N_b}{2\pi}\int_0^{2\pi}\int_0^R r\cos\psi\, dT d\psi \end{cases} \tag{2.25}$$

where N_b refers to the number of blades. The non-dimensional results follow the rules

- Thrust coefficient C_T: multiply for $\dfrac{1}{\rho\pi\Omega^2 R^4}$
- Moment coefficient C_m: multiply for $\dfrac{1}{\rho\pi\Omega^2 R^5}$

2.4.2 Delta Trim Method

The delta trim method is an incremental coupling algorithm that couples the CFD and BET approaches to calculate the sensitivity derivatives. In summary, in an iterative fashion, the approach completely substitutes the CFD computed airloads with BET solutions in the Jacobian matrix computation, resulting in a high-efficiency trimming procedure. The implementation details are outlined in Figure 2.9 and summarized in 6 steps.

- **Step 1: Initialize the control settings:** the initial control angles (θ_0, θ_{1c}, θ_{1s}) could be set with the test data or estimated using the following equations given by Steijl et al [37].

$$\begin{cases} \theta_0 = \dfrac{6C_T^{target}}{a\sigma}\left(\dfrac{1+3\mu^2/4}{1-\mu^2+\dfrac{9}{4}\mu^4}\right) - \dfrac{3}{2}\lambda\left(\dfrac{1-\mu^2}{1-\mu^2+\dfrac{9}{4}\mu^4}\right) \\ \lambda = -\sqrt{\dfrac{\sqrt{\mu^4+{C_T}^2}-\mu^2}{2}} \end{cases} \tag{2.26}$$

  where σ is the rotor solidity, a is the lift-curve slope equal to 5.7, μ is the advance ratio, and λ denotes the inflow ratio. With this formula, both the initial cyclic pitch angles (θ_{1c}, θ_{1s}) are set to be zero.

- **Step 2: Initial calculation with CFD solver:** Two or three revolutions are performed by the unsteady CFD simulation to obtain the initial values of thrust and moment coefficients: $C_{T_0}^{CFD}$, $C_{mx_0}^{CFD}$ and $C_{my_0}^{CFD}$, where the superscript CFD represents the CFD solver in the outer loop and the subscript 0 indicates that the trim cycle number is equal to zero.

- **Step 3: Inner loop with BET solver:** Computing the Jacobian matrix using the BET solver. A small increment δ is added to each control setting, and then

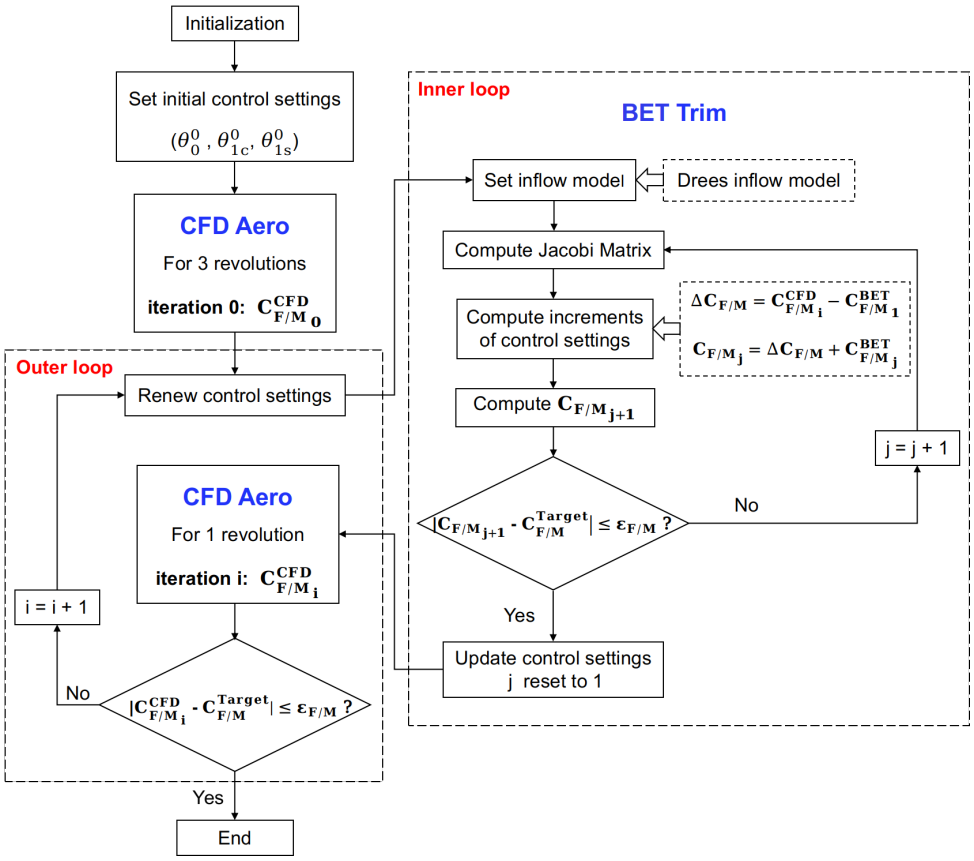

Figure 2.9: *Delta trimming procedure*

the forward difference scheme is adopted to calculate the partial derivatives in the Jacobian matrix (the derivatives of θ_0 are taken as an example).

$$\begin{cases} \dfrac{\partial C_{Tj}}{\partial \theta_0} \approx \dfrac{C_{Tj}^{BET}(\theta_0+\delta,\theta_{1c},\theta_{1s}) - C_{Tj}^{BET}(\theta_0,\theta_{1c},\theta_{1s})}{\delta} \\ \dfrac{\partial C_{Mxj}}{\partial \theta_0} \approx \dfrac{C_{Mxj}^{BET}(\theta_0+\delta,\theta_{1c},\theta_{1s}) - C_{Mxj}^{BET}(\theta_0,\theta_{1c},\theta_{1s})}{\delta} \\ \dfrac{\partial C_{Myj}}{\partial \theta_0} \approx \dfrac{C_{Myj}^{BET}(\theta_0+\delta,\theta_{1c},\theta_{1s}) - C_{Myj}^{BET}(\theta_0,\theta_{1c},\theta_{1s})}{\delta} \end{cases} \tag{2.27}$$

where the superscript BET represents the BET solver in the inner loop and the subscript j denotes the inner loop number.

- **Step 4: Update control settings:** the control angles are calculated by the Newton's iteration method, and the increment of control settings at each inner loop

becomes:

$$\begin{bmatrix} \Delta\theta_0 \\ \Delta\theta_{1c} \\ \Delta\theta_{1s} \end{bmatrix} = \begin{bmatrix} \frac{\partial C_T}{\partial\theta_0} & \frac{\partial C_T}{\partial\theta_{1c}} & \frac{\partial C_T}{\partial\theta_{1s}} \\ \frac{\partial C_{Mx}}{\partial\theta_0} & \frac{\partial C_{Mx}}{\partial\theta_{1c}} & \frac{\partial C_{Mx}}{\partial\theta_{1s}} \\ \frac{\partial C_{My}}{\partial\theta_0} & \frac{\partial C_{My}}{\partial\theta_{1c}} & \frac{\partial C_{My}}{\partial\theta_{1s}} \end{bmatrix}^{-1} \cdot \begin{bmatrix} C_T^{target} - (\Delta C_T + C_{T_j}^{BET}(\theta_0, \theta_{1c}, \theta_{1s})) \\ -(\Delta C_{Mx} + C_{Mx_j}^{BET}(\theta_0, \theta_{1c}, \theta_{1s})) \\ -(\Delta C_{My} + C_{My_j}^{BET}(\theta_0, \theta_{1c}, \theta_{1s})) \end{bmatrix} \tag{2.28}$$

$$\begin{cases} \Delta C_T = C_{T_i}^{CFD}(\theta_0, \theta_{1c}, \theta_{1s}) - C_{T1}^{BET}(\theta_0, \theta_{1c}, \theta_{1s}) \\ \Delta C_{Mx} = C_{Mx_i}^{CFD}(\theta_0, \theta_{1c}, \theta_{1s}) - C_{Mx1}^{BET}(\theta_0, \theta_{1c}, \theta_{1s}) \\ \Delta C_{My} = C_{My_i}^{CFD}(\theta_0, \theta_{1c}, \theta_{1s}) - C_{My1}^{BET}(\theta_0, \theta_{1c}, \theta_{1s}) \end{cases} \tag{2.29}$$

- **Step 5: Update thrust and moment coefficients with BET solver:** Perform a BET computation with the updated control angles. The inner loop is about to the end and the inner loop number j will be reset to 1 if the discrepancy between the computed results and the target values is less than the pre-defined convergence criteria, otherwise return to **Step 3** with the updated trim variables: $\theta_0, \theta_{1c}, \theta_{1s}$

$$\begin{cases} \theta_0 = \theta_0 + \Delta\theta_0 \\ \theta_{1c} = \theta_{1c} + \Delta\theta_{1c} \\ \theta_{1s} = \theta_{1s} + \Delta\theta_{1s} \end{cases} \tag{2.30}$$

- **Step 6: Update thrust and moment coefficients with CFD solver:** Run the CFD solver for one revolution with the updated control settings obtained in **Step 5** and compare the calculate thrust and moment coefficients $C_{T_i}^{CFD}$, $C_{mx_i}^{CFD}$ and $C_{my_i}^{CFD}$ with the target values. The trim procedure stops if the convergence criteria are satisfied, otherwise repeats **Step 3** to **Step 5**. In the present work, the convergence criteria are given as follows:

$$\begin{cases} |C_T - C_T^{target}| \leq 0.01 \cdot C_T^{target} \\ |C_{Mx} - C_{Mx}^{target}| \leq 1 \times 10^{-5} \\ |C_{My} - C_{My}^{target}| \leq 1 \times 10^{-5} \end{cases} \tag{2.31}$$

CHAPTER 3

Numerical Validation

The partial content of this chapter is published in Jinbin Fu, Luigi Vigevano. **Aeroacoustic modelling of helicopter transonic rotor noise**. *Aerospace Science and Technology*. (122)2022, 107430. DOI: 10.1016/j.ast.2022.107430.

It is mandatory for any newly developed computational tool to go through the validation procedure. The current chapter focuses on the numerical validation of the acoustic methods, trim algorithm, and simulation framework introduced in the previous chapter.

The validation work starts from each component of the simulation framework. An evaluation of the MC algorithm in emission surface construction is performed first. Numerical calculations are then carried out using the ROCAAP code to validate the ability to produce good acoustic predictions. Afterward, three well-documented rotors, the AH-1G, AH-1/OLS and HART-II, are adopted to validate the rotor trim method. Finally, the assessment work for the integrated simulation framework is exploited with transonic and BVI noise predictions.

3.1 Validation of the Aeroacoustic Approaches

This section validates the ROCAAP code for aeroacoustic predictions. In the Retarded-Time algorithm, the control surface can be naturally applied for integrating the FW-H equation without additional transformations. However, in the Emission-Surface algorithm, the numerical construction of the emission surface might be difficult due to the appearance of unconnected patches caused by the multiple emission times when the sources are moving supersonically. Therefore, firstly, a scaled UH-1H rotor planform that rotates both in subsonic and transonic-supersonic regimes and a supersonic rotating cylindrical strip are employed to demonstrate the validity of the MC algorithm in constructing emission surfaces. A static 3D monopole source case is then considered for

testing the implemented approaches by comparing the calculated results to analytical solutions. At last, the preliminary validation is carried out using the two-blade UH-1H rotor with a simpified aerodynamic model [117].

3.1.1 Rotational Blade Planform

A rotational blade planform is used as a validation case for the emission surface construction. As shown in Figure 3.1 The blade planform is the $1/7$-scale UH-1H rotor model with a radius of 1.045m and the aspect ratio of AR = 13.71. It is operated from a subsonic region, $M \approx 0.2$ at the blade root up to a supersonic regime, $M \approx 1.5$ at the blade tip. Far-field observer lies at the rotor disc plane at 3.09 rotor radii away from the rotor hub. The blade mesh is composed of upper and lower surfaces with a dimension of 10×20 (number of nodes at each section $\times$ number of sections).

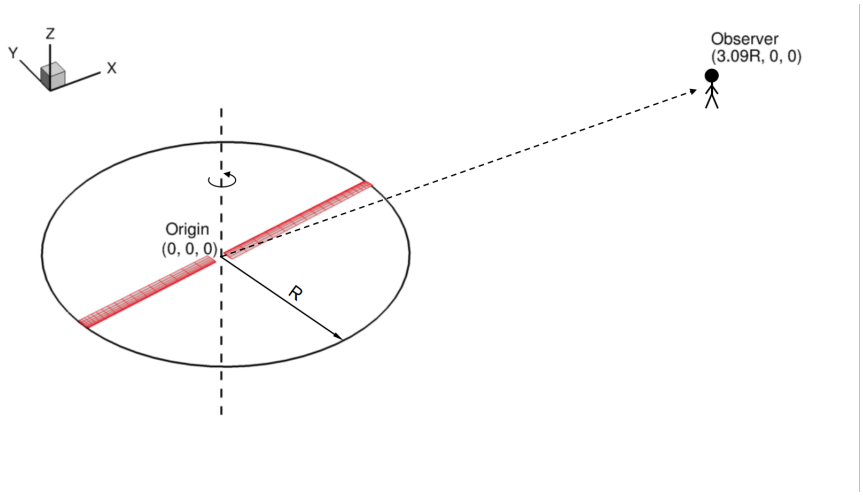

Figure 3.1: *The test configuration for a rotational blade planform.*

The emission surface shapes at two subsequent observer time steps (t = 0.02572s and 0.02586s) are illustrated in Figure 3.2, where the surface is rendered with the value of the emission time τ. In Figure 3.2a, emission surface consists of two branches, which are moving towards the sonic circle of $M_r = 1$; afterward, the two components are merged together and form a "wing-like" shape (Figure 3.2b), which is the union of all retarded position of the blade planform grid points. A qualitative comparison on the construction of the emission surface is carried out with a similar case calculated by Loiodice [102]. The emission surface predictions from Ref [102] at two similar observer time instants are presented in Figure 3.2c and 3.2d. It is clear that the predicted emission surfaces have the similar transformation shapes as in past study [102], which means that the emission surfaces are constructed correctly with the use of the MC algorithm.

3.1.2 The Λ Singularity

The singular behavior of the Λ term of equation (3.1) is an issue of interest for transonic noise predictions. It is recognized as the primary source for the infinite pulses in the predicted noise signals. From the mathematical point of view, Λ = 0 occurs when the

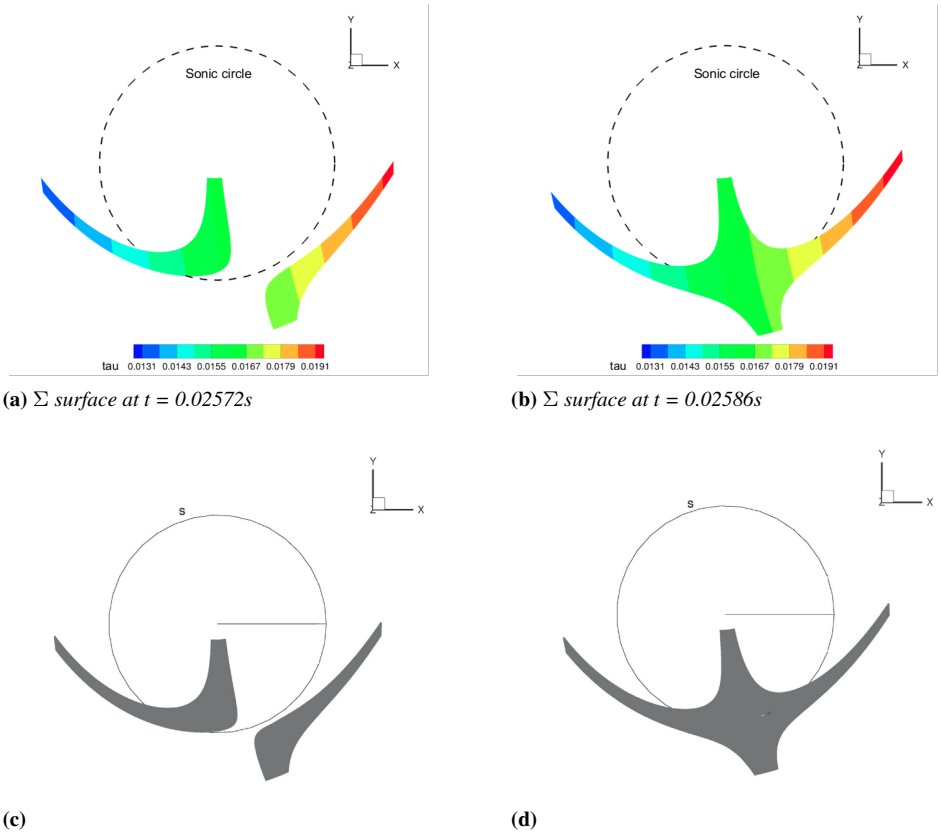

(a) Σ *surface at t = 0.02572s*

(b) Σ *surface at t = 0.02586s*

(c)

(d)

Figure 3.2: *Emission surface of rotating blade planform at* $M_T = 1.5$ *for two subsequent observer instants. (a), (b) results calculated by present method. (c), (d) results calculated by Loiodice [102].*

control surface grid geometric and kinematic data satisfied the following conditions:

$$\begin{cases} \mathbf{M}\cdot\mathbf{n} = +1; & \mathbf{n}\cdot\mathbf{r} = +1 \quad \Rightarrow \Lambda = 0, \\ \mathbf{M}\cdot\mathbf{n} = -1; & \mathbf{n}\cdot\mathbf{r} = -1 \quad \Rightarrow \Lambda = 0 \end{cases} \tag{3.1}$$

which is less restrictive than the condition of Doppler singularity in Retarded-Time formulation, $\mathbf{M}\cdot\mathbf{r} = 1$.

In this section, a rotational cylindrical strip is used to clarify different behavior of the Doppler singularity between the Emission-Surface formulation and the Retarded-Time formulation. The strip is rotating along the z axis with a Mach number of M_T = 1.1 at the center of the strip. The cylindrical strip geometry is displayed in Figure 3.3a, the rotational radius $R_T = 1.1c_0/\Omega$ (c_0 = 340 m/s, Ω = 340 rad/s), the strip radius and width are d_{cyl} = 0.44 m and $w_{cyl} = d_{cyl}/5$, respectively. Figure 3.3b depicts the test configuration, in which the observer is located at $\mathbf{x}_{ob}$ = (5,0,0) m, line p1 and p2 represent the tangents to the circular trajectory passing through the observer, t1 and t2 are the critical lines in radial direction perpendicular to lines p1 and p2. By approaching the line t2, a critical configuration of emission surface can appear due to Λ being close to zero at the leading or trailing edge of the strip (see Figure 3.4, the contour on the emission surface refer to the $[1/\Lambda]$ value). Whereas, no critical emission surface configuration can occur when approaching line t1, since $\mathbf{M}\cdot\mathbf{n}$ and $\mathbf{n}\cdot\mathbf{r}$ always have opposite signs.

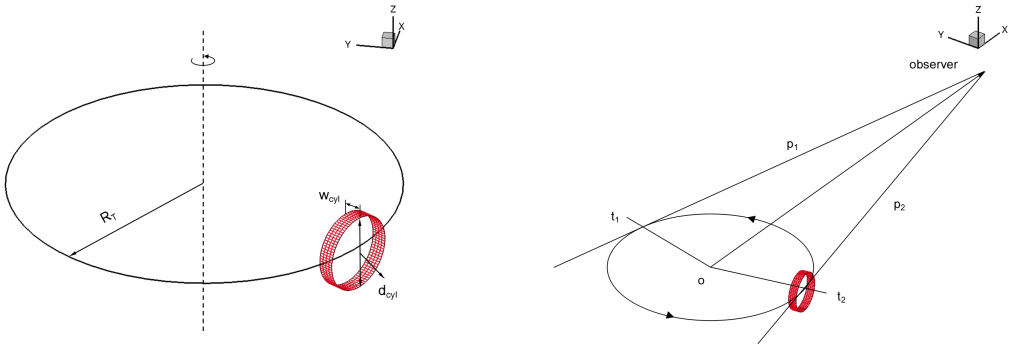

(a) *Geometry*

(b) *Test configuration with observer position*

Figure 3.3: *Cylindrical strip configuration.*

The time history of the $[1/\Lambda]_{max}$ term is presented in Figure 3.5a to show the Λ singularity behavior within the period of revolution. The two peak values, which are the undesirable solutions due to the absolute value of Λ being close to zero, simultaneously corresponding to the critical configurations as illustrated in Figure 3.4 and the conditions given in equation (3.1). To compare with the Doppler singularity, Figure 3.5b shows the $[1/|1 - M_r|]_{max}$ time history, exhibiting multiple pulse points with the magnitude of 10^5 times of $[1/\Lambda]_{max}$, the maximum value appears at almost the same time instant of the first cusp point in Figure 3.5a. The comparison of the $[1/\Lambda]_{max}$ and $[1/|1 - M_r|]_{max}$ time histories indicates that the Emission-Surface algorithm is much more robust than the Retarded-Time formulation and does not need to resort to a de-singularization procedure.

Figure 3.6 shows the time evolution of the computed emission surface, corresponding to the "U" shape variation of $[1/\Lambda]_{max}$ from time steps (a to (f in Figure 3.5a. The first frame (Figure 3.6a) and the last frame (Figure 3.6f) depict the critical stages in which the Λ is approaching singularity. It can be seen from Figure 3.6, the two emission surface branches are travelling towards each other. After few instants, the two branches come in contact (Figure 3.6b), then merge to a single large cylindrical strip (Figure 3.6c). In Figure 3.6d and Figure 3.6e, the larger cylindrical strip is divided into two branches again, and the $[1/\Lambda]_{max}$ gradually reaches to the peak value (Figure 3.6f).

Loiodice [102] and Ianniello [101] also calculated a similar cylindrical strip. A quantitative comparisons of the emission surface maximum $[1/\Lambda]$ time evolution are shown in Figure 3.5a. The agreement between calculated data and the results reported by Loiodice [102] and Ianniello [101] is reasonably good.

3.1.3 Comparison with Analytical Solutions

A stationary permeable spherical control surface with unit radius and a centered monopole noise source is used to test the Retarded-Time and Emission-Surface algorithms by comparing it with the analytical solution. In this study, the spherical control surface is uniformly discretised in the spherical coordinates using variables Θ and Ψ with four different grid resolutions ($N_\Theta \times N_\Psi$ = 9×18, 12×24, 18×36 and 36×72); the period of noise source is discretized with NRT = 60, 120, 240 time steps. The observer

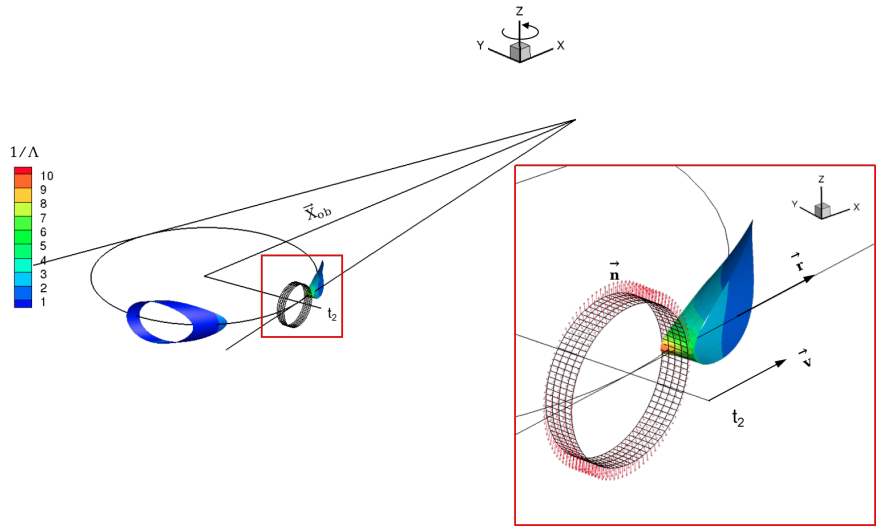

(a) *High* $1/\Lambda$ *value at the leading-edge*

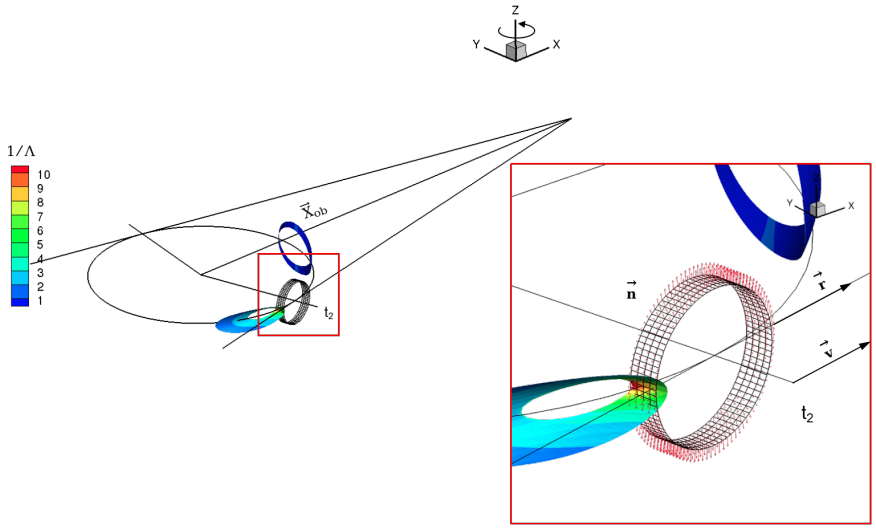

(b) *High* $1/\Lambda$ *value at the trailing-edge*

Figure 3.4: *Two critical regions of the cylindrical strip (the emission surface colored by the* $1/\Lambda$ *value).*

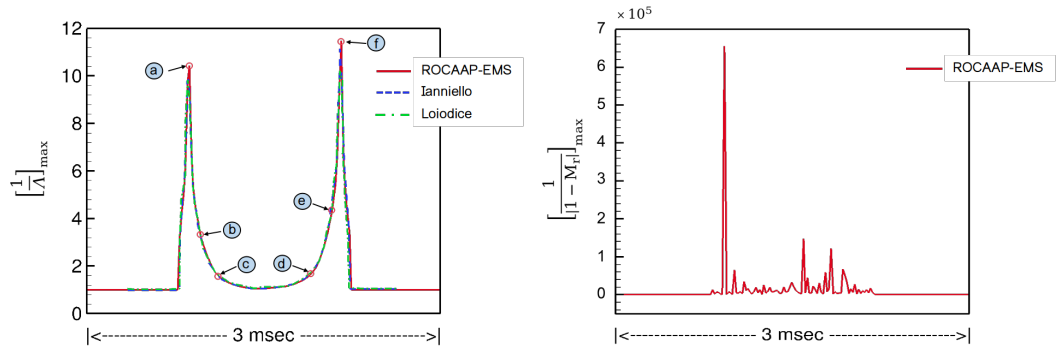

(a) *The* $[\frac{1}{\Lambda}]_{max}$ *value*

(b) *The* $[\frac{1}{|1-M_r|}]_{max}$ *value*

Figure 3.5: *Time history of the integral kernel term.*

is located at $\mathbf{x}_o = [5, 0, 0]$. A schematic of the test configuration is shown in Figure 3.7.

The monopole noise source, which located at the center of the defined spherical control surface, is represented by a simple harmonic velocity potential function:

$$\phi(\mathbf{x}, t) = \frac{A}{4\pi r} e^{i\omega\left(t - \frac{r}{c_0}\right)} \tag{3.2}$$

with the velocity potential amplitude A = 1 m^2/s^{-1}, angular velocity $\omega = 100\pi\ rad/s$, distance of observer position and monopole source point $r = 5\ m$.

With the equation (3.2), the analytical induced solution of acoustic pressure p', density ρ' and velocity $\mathbf{u}$ are expressed as

$$\begin{aligned} p'(\mathbf{x}, t) &= -\rho_\infty \frac{\partial \phi}{\partial t} \\ \rho'(\mathbf{x}, t) &= \frac{p'}{{c_0}^2} \\ \mathbf{u}(\mathbf{x}, t) &= \nabla \phi(\mathbf{x}, t) \end{aligned} \tag{3.3}$$

In order to measure the difference between numerical and analytical solutions to assess the implementation of the Retarded-Time and Emission-Surface algorithms, a generic parameter, ε, is defined as follows.

$$\varepsilon = \frac{\sum_{i=1}^{N_t} \sum_{j=1}^{N_x} |P_N(x_j, t_i) - P_A(x_j, t_i)|}{\sum_{i=1}^{N_t} \sum_{j=1}^{N_x} |P_A(x_j, t_i)|} \tag{3.4}$$

where $P_N(x_j, t_i)$ and $P_A(x_j, t_i)$ are the computed and exact solutions at the observer position x_j and at the observer time instant t_i. N_t and N_x are the number of observer times and positions, respectively. In addition, since the spherical control surface is uniformly discretized, the grid cell size values h corresponding to the above-defined grid space discretization are in order: h = $\pi/9, \pi/12, \pi/18, \pi/36$.

In the Retarded-Time algorithm, the defined spherical control surface can directly apply to the noise calculation without any transformation. However, the Emission-Surface algorithm predicts the noise by transforming the original control surface into

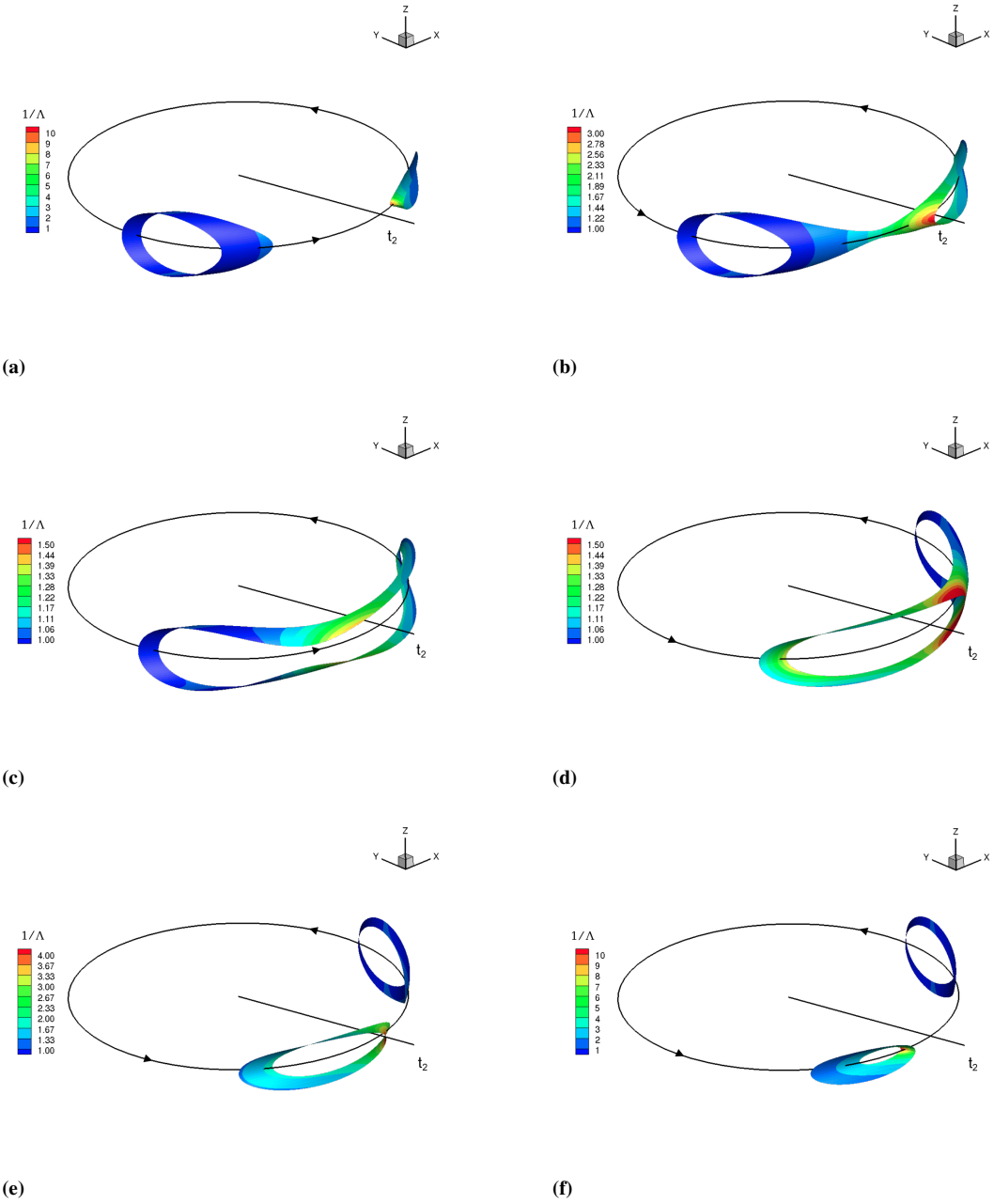

Figure 3.6: Σ *surface of rotating cylindrical strip for six subsequent observer instants.*

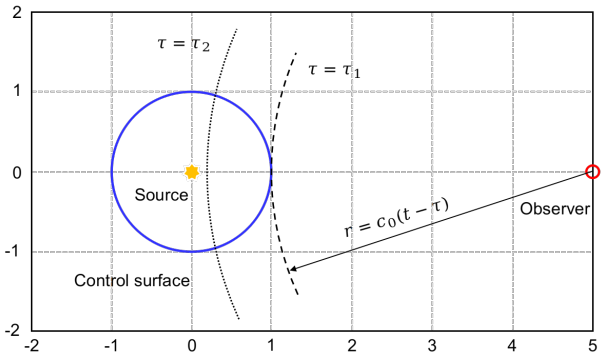

Figure 3.7: *The test configuration for a spherical surface.*

the emission surface using the MC algorithm. In this case, the ratio, $\eta = S_{MC}/S_E$, is employed as an evaluation criterion to evaluate the precision of emission surface reconstruction with S_{MC} marching cube emission surface area and S_E exact emission surface area. The exact area of the sphere is $S_E = 4\pi = 12.5664$.

Since the spherical control surface is steady, the emission surface coincides with the permeable control surface. Figure 3.8 presents the emission surface corresponding to the sphere at three subsequent observer time instants in the absolute reference frame and the MC domain. The surface is rendered with the value of the emission time τ. Observing Figure 3.8a, the emission surface Σ is only a part of the sphere and then gradually grows to the entire sphere over time; see Figure 3.8c and Figure 3.8e. This is because the radius of the collapse sphere, $r = c_0(t - \tau)$ (where $-\infty < \tau \leq t$), increases with the observer time. Figure 3.8b, 3.8d and 3.8f correspond to the emission surface evolution in the MC domain. It can be seen that the emission surface grows from two disjoint patches to a continuous surface with observer time increases. Based on above, the calculated emission surface areas for the sphere with four different grid resolutions at three circumstances of time discretization are presented in Table 3.1. It is evident that the MC algorithm correctly constructs the emission surface of a stationary spherical permeable surface.

Table 3.1: *η value of four different grid resolution spherical permeable surfaces under three temporal discretisations.*

NRT	Grid resolution			
	9×18	12×24	18×36	36×72
60	0.9286	0.9579	0.9806	0.9949
120	0.9316	0.9614	0.9819	0.9952
240	0.9360	0.9640	0.9832	0.9955

Figure 3.9a compares the acoustic results of the Emission-Surface algorithm with the four different grid resolution permeable control surfaces and the exact solution. A reasonably good agreement with minor discrepancies close to the peaks of the signal is observed. The slight inaccuracy is progressively eliminated as the finer resolution grid is employed. In Figure 3.9b, the numerical errors for four grid levels with three spatial discretizations are plotted on a logarithmic scale to understand the order of accuracy of both Retarded-Time and Emission-Surface algorithms. The errors are shown to drop

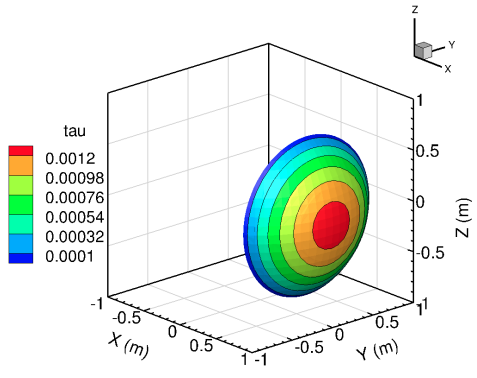

(a) *t = 0.01307 s, AF*

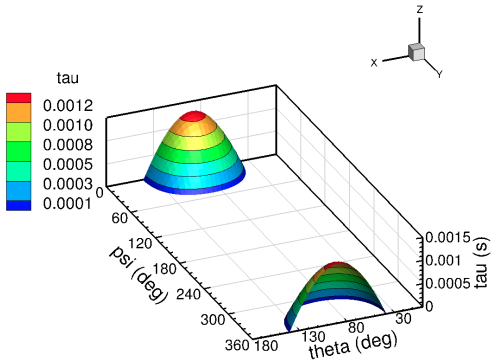

(b) *t = 0.01307 s, MC*

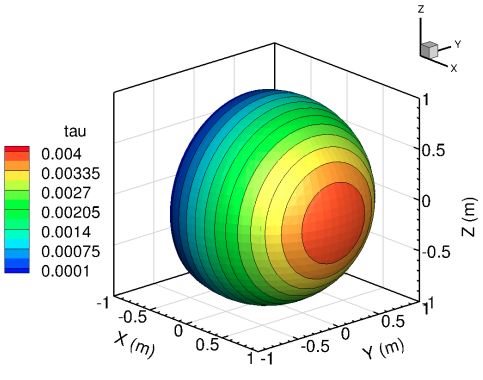

(c) *t = 0.01573 s, AF*

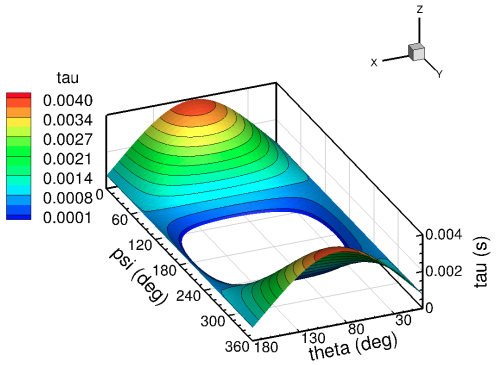

(d) *t = 0.01573 s, MC*

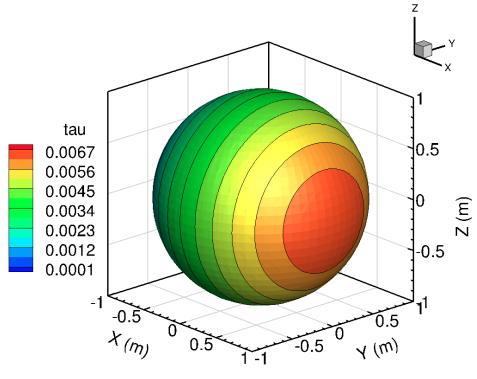

(e) *t = 0.0184 s, AF*

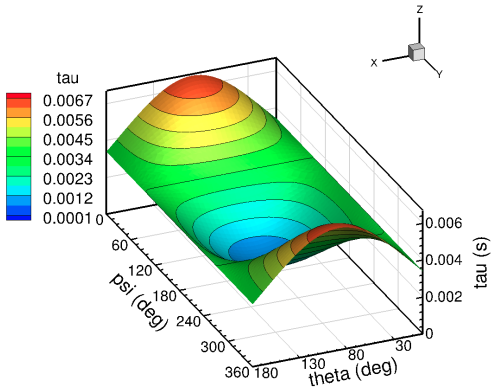

(f) *t = 0.0184 s, MC*

Figure 3.8: *Σ surface of a stationary permeable spherical surface for different observer time instants in AF and MC domains.*

in a similar second-order manner as the spatial discretization is refined, which is consistent with the accuracy of the Midpoint quadrature integration method used in both two integral algorithms. It demonstrates that the theoretical precision of the integration method is preserved.

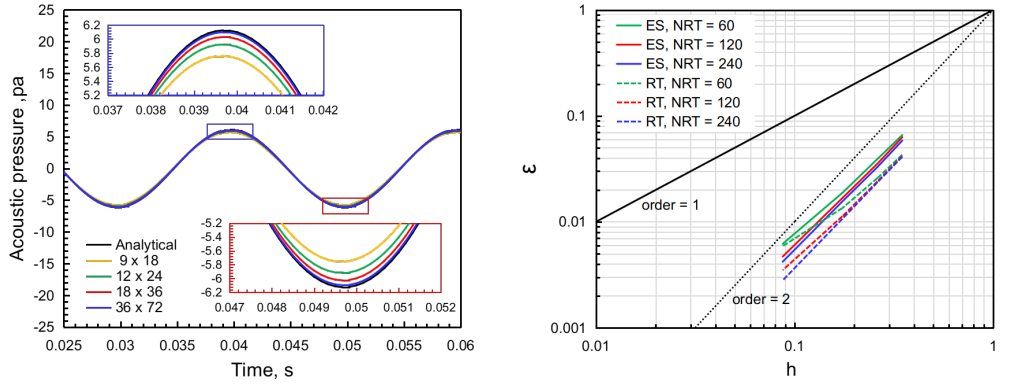

(a) *Time histories of the acoustic pressure with NRT=120*

(b) *Numerical error in acoustic pressure for the both Emission-Surface and Retarded-Time algorithms*

Figure 3.9: *Numerical results of the monopole source with 4 different grid resolution control surfaces.*

3.1.4 Comparison with WOPWOP Solutions

A 1/4-scale UH-1 main rotor in forwarding flight, used by Brentner [117] for the validation of the WOPWOP code, is now taken into account to preliminary validate the implemented acoustic methods in ROCAAP. The geometric parameters are outlined in Table 3.2. In this case, the aerodynamic pressure is assigned on the blade surface by combining the airfoil aerodynamic look-up table and analytic airfoil theory; the blade kinematics are prescribed by a truncated Fourier series up to the second harmonics. Therefore, with the non-penetration condition ($u_n = v_n$) imposed on the blade surface, equation (2.11) and (2.14) lead to the impermeable formulations, as follows:

Table 3.2: *Geometric properties of the 1/4-scale UH-1 main rotor [117].*

N_b	2
Blade planform	Rectangular
Blade section	NACA0012
R	1.829 m
c	0.1334 m
θ_{tw}	Linear, $-10.9°$
R_c	$0.155R$

$$4\pi p'(\mathbf{x},t) = \frac{1}{c_0}\frac{\partial}{\partial t}\int_S \left[\frac{\rho_0 c_0 u_n + P'_{nr}}{r|1-M_r|}\right]_{ret} dS + \int_S \left[\frac{P'_{nr}}{r^2|1-M_r|}\right]_{ret} dS \tag{3.5}$$

$$4\pi p'(\mathbf{x},t) = \frac{1}{c_0}\frac{\partial}{\partial t}\int_\Sigma \left[\frac{\rho_0 c_0 u_n + P'_{nr}}{r\Lambda}\right]_{ret} d\Sigma + \int_\Sigma \left[\frac{P'_{nr}}{r^2\Lambda}\right]_{ret} d\Sigma \tag{3.6}$$

The operation conditions are listed in Table 3.3. Two examples are considered for the validation. The first example uses a forwarding flight UH-1 rotor with a medium advance ratio, the overall noise is dominated by the thickness noise since the observer is located in the tip path plane (TPP) of the rotor. In the second case, the forwarding flight UH-1 rotor with a lower advance ratio is employed, the loading noise dominates the overall noise as the mircophone is located below the rotor just outside the right side of the rotor.

Table 3.3: *Operation conditions of the 1/4-scale UH-1 main rotor [117].*

Case Name	Example 1	Example 2
μ	0.205	0.123
α_s	8.85°	8.00°
Ω	1296 RPM	1296 RPM
c_0	340 m/s	340 m/s
ρ_0	1.234 kg/m^3	1.234 kg/m^3
θ_0	13.82°	13.53°
θ_{1c}	2.20°	1.61°
θ_{1s}	−1.47°	−1.44°
β_0	2.75°	2.75°
β_{1c}	−1.50°	0.27°
β_{1s}	1.18°	0.01°
$\mathbf{x}_{obs}$	[3.21, −2.16, −0.30]	[0.41, −0.68, −0.72]

Numerical results of ROCAAP code with both Retarded-Time and Emission-Surface algorithms are compared with the experimental data and WOPWOP solutions, as shown in Figure 3.10. As expected, the thickness and loading noise dominate the acoustic signals for Example 1 and 2 cases, respectively. Moreover, solutions of Retarded-Time and Emission-Surface algorithms are almost overlapped for both example cases, except for some discrepancies in the peaks of Example 1. As plotted in Figure 3.11, these differences could be attributed to the large deformed emission surface Σ generated by the advancing blade surface when the observer position is located at the rotor TPP plane. To sum up, the capabilities of the ROCAAP code to predict the noise generated by the helicopter rotor are preliminarily validated through good correlation with experimental data and WOPWOP results.

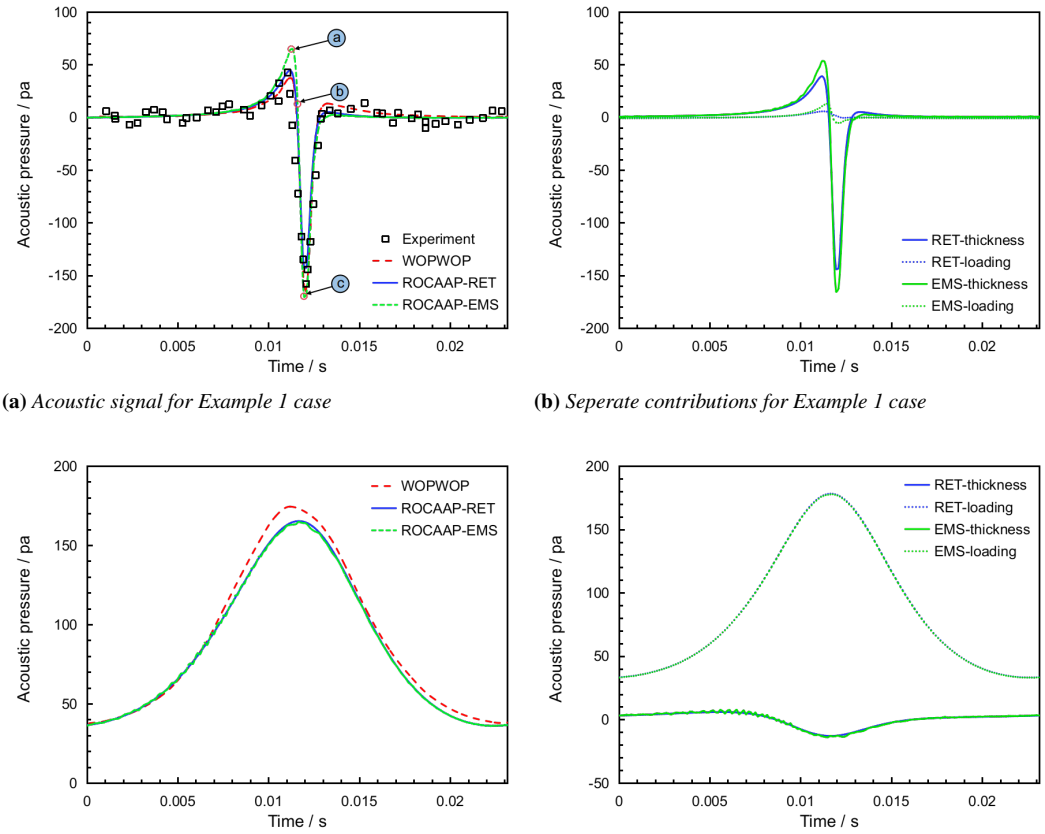

(a) *Acoustic signal for Example 1 case*

(b) *Seperate contributions for Example 1 case*

(c) *Acoustic signal for Example 2 case*

(d) *Seperate contributions for Example 2 case*

Figure 3.10: *Acoustic pressure of UH-1 rotor, numerical results are compared with experimental and WOPWOP data.*

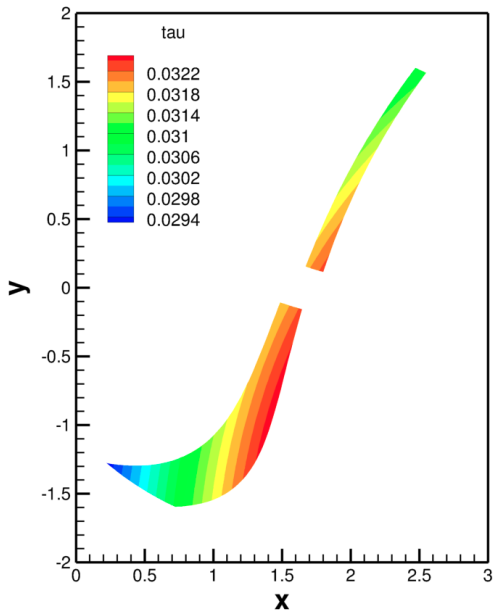

(a) Σ *surface at t = 0.04518 s*

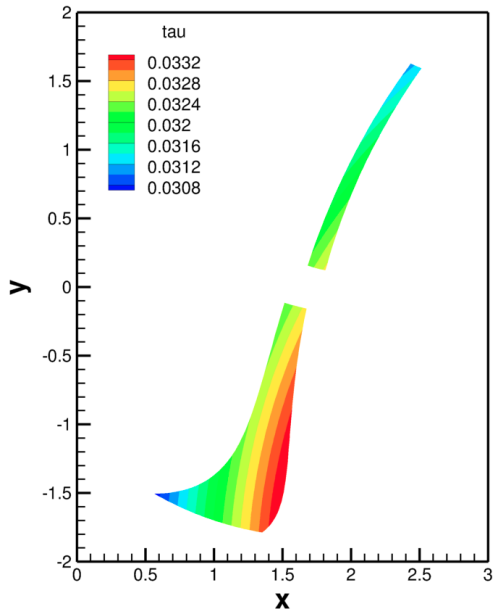

(b) Σ *surface at t = 0.04557 s*

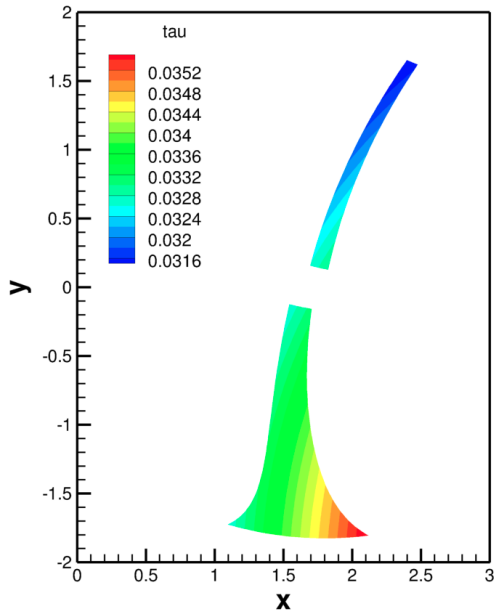

(c) Σ *surface at t = 0.04596 s*

Figure 3.11: *Emission Surface for Example 1 case at three observer time instants, corresponding to the tag (a to (c in Figure 3.10a.*

3.2 Evaluation of the Rotor Trim Method

This section aims to validate the trim method for the helicopter main rotor in forwarding flight conditions. Three representative forwarding flight helicopter rotors are simulated in this regard: AH-1G, AH-1/OLS and HART-II main rotors. At first, a mid-fidelity Panel/Viscous Vortex Particle Method (VVPM) solver [118] is adopted to fast simulate the AH-1G rotor to preliminary validate the original delta trim method. After that, the CFD solver ROSITA, together with the multi-dimensional delta trim methods, are performed to simulate the AH-1/OLS and HART-II rotor cases to assess the effectiveness and efficiency of the presented trim method.

3.2.1 AH-1G Main Rotor

In Ref. [119], a fight test referring to an AH-1G cobra helicopter was conducted by NASA Ames Research Center to investigate helicopter rotor tip aerodynamics and acoustics. The AH-1G main rotor has two untapered, rectangular linear twisted blades with a symmetric the Operational Load Survey/Tip Aerodynamics and Acoustics Test (OLS/TAAT) airfoil. The geometric properties of the AH-1G main rotor are shown in Table 3.4. In the aerodynamic phase of testing, several thrust coefficients are specified with adjusted blade control angles. Therefore, it is well suited to evaluate the trim methods.

Table 3.4: *Geometric properties of the full-scale AH-1G main rotor [119].*

N_b	2
Blade planform	Rectangular
Blade section	OLS/TAAT
R	6.7 m
c	0.7283 m
θ_{tw}	Linear, $-10.0°$
R_c	$0.154R$

The low-speed case which correlated to test point 2157 is employed. The rotor operated at an advance ratio of 0.19 and blade tip Mach number of 0.65. The measured time-averaged rotor thrust coefficient C_T equals 0.00464. This work uses a panel/VVPM solver developed by Zhu [118] for preliminarily validating the original delta trim method. Each blade is modeled with a dimension of 41×17 (number of nodes at each section $\times$ number of sections), the azimuthal angle increment is $3°$. During the computation, the precone and shaft angles were set to 0.00, the flight test control angles were used as an initial estimation for the rotor trim.

Figure 3.12 illustrates the trimming convergence history of the original delta trim method. It can be seen that the trim method has reached the convergence value after four cycles. It is evident that the original delta trim method is more efficient than the traditional Newton-Raphson iterative trim method [51] because the aerodynamic solver only needs to run once per trimming cycle in the delta trim method; in contrast, this solver has to be run at least five times for each trimming cycle in traditional Newton's iterative trim method.

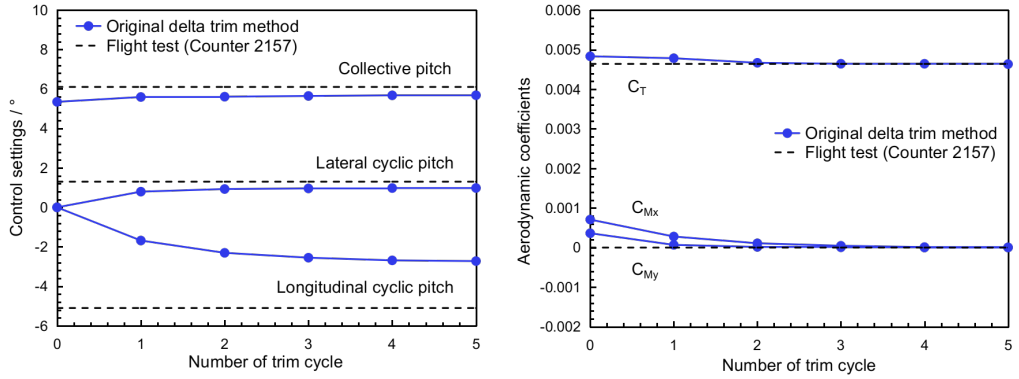

(a) *Trim variables* **(b)** *Airloads*

Figure 3.12: *Convergence history of trimming process.*

Table 3.5 reports the trimmed results. Figure 3.13 presents the variation of blade normal force coefficients at four radial positions over one revolution. The results calculated with trimmed control settings are compared with flight test data [119] and the untrimmed solution (the results computed using the flight test control parameters). The plot shows that the trimmed solution achieves a good correlation with the test data. Based on the above, the effectiveness and efficiency of the original delta trim method are well demonstrated.

Table 3.5: *Blade harmonics for the AH-1G rotor.*

Case Name	Counter 2157	Original delta trim method
θ_0	$6.00°$	$5.68°$
θ_{1c}	$1.70°$	$0.98°$
θ_{1s}	$-5.50°$	$-2.72°$
β_0	$0.0°$	$0.0°$
β_{1c}	$2.13°$	$2.13°$
β_{1s}	$-0.15°$	$-0.15°$

3.2.2 AH-1/OLS Main Rotor

The OLS/TAAT [120] in the German-Dutch Wind Tunnel (DNW) is considered to validate the multi-dimensional trim method. The experiment involved a $1/7$-scaled AH-1 helicopter main rotor. More descriptions about the rotor geometry and test conditions are reported in Table 3.6. The blade motion given by the experiment is expressed as follows:

$$\begin{aligned} \theta(\psi) &= 6.14 + 0.9\cos(\psi) - 1.39\sin(\psi) \\ \beta(\psi) &= 0.5 - 1.0\cos(\psi) \end{aligned} \tag{3.7}$$

For the CFD simulations, a moving embedded grid system was designed for the present study to simulate the motion of rotor blades in forwarding flight. It consisted of a far-field background grid (FG), a near-field background grid (NG), a wake grid

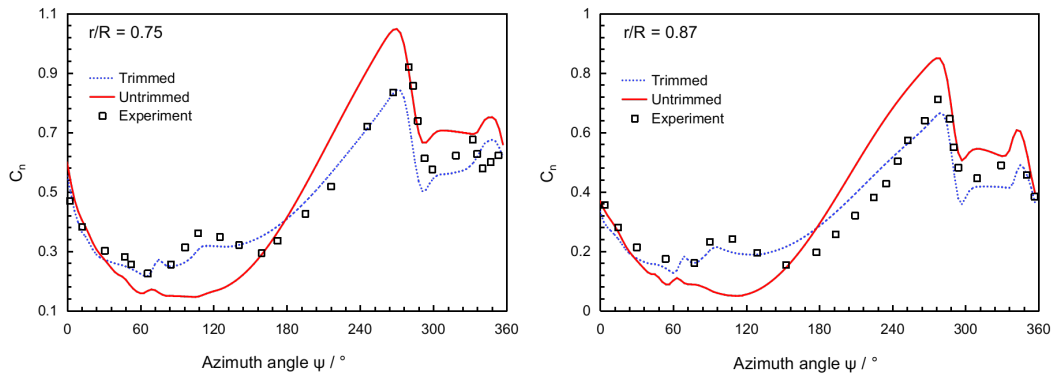

(a) $r/R = 0.75$ **(b)** $r/R = 0.87$

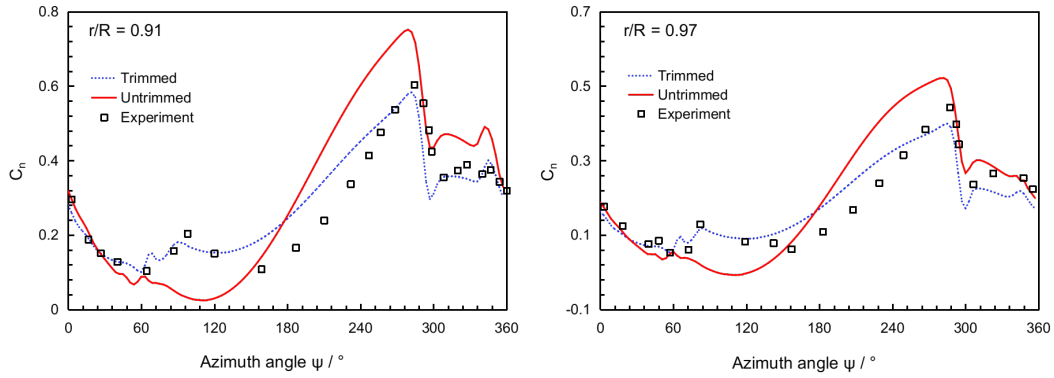

(c) $r/R = 0.91$ **(d)** $r/R = 0.97$

Figure 3.13: *Sectional normal force coefficients variation for AH-1G main rotor.*

Table 3.6: *Geometric properties and test conditions of the AH-1/OLS main rotor [120].*

N_b	2
Blade planform	Rectangular
Blade section	BTH-540
R	0.958 m
c	0.1039 m
θ_{tw}	Linear, $-8.2°$
R_c	$0.182R$
Test point	10014
μ	0.164
α_s	$0°$
ω	235.7 rad/sec (M_T = 0.664)
C_T^{target}	0.0054
C_{Mx}^{target}	0.00
C_{My}^{target}	0.00

(WG), and two identical body-fitted blade grids (BG), as illustrated in Figure 3.14. The far-field grid was generated to represent the flow domain far from the rotor, where outer boundaries were located 2R (above), 4R (below), and 5R (radial) away from the blade hub. The near-field grid was created to model the flow region close to the blades. The wake grid was built to capture the rotor wake. The body-fitted grid was modeled with a C-H topology with a non-slip boundary condition on the blade surface. The wall distance of the first layer of body surfaces was set to $1 \times 10^{-5}c$ so that the y^+ value was less than 1.

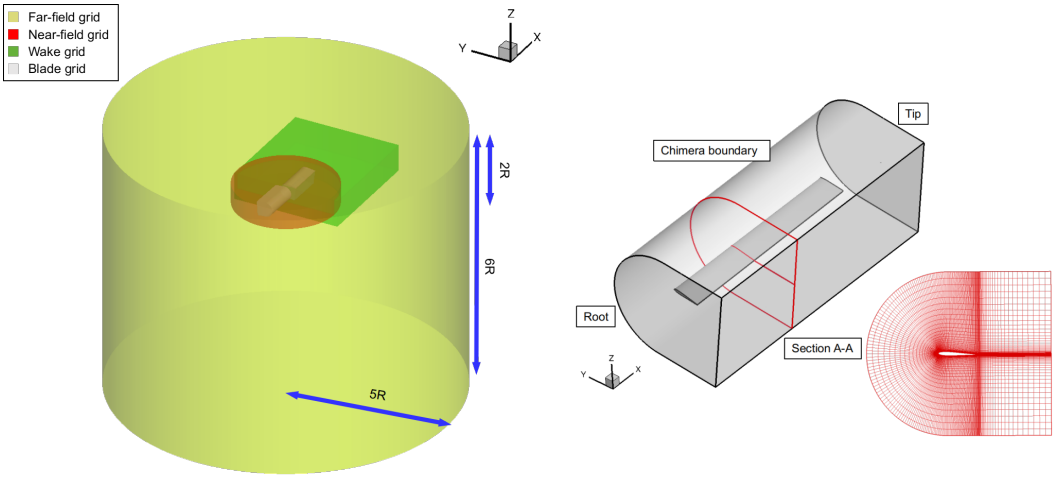

Figure 3.14: *Computational domain and detailed view of AH-1/OLS rotor blade grid.*

Two Chimera grid systems with the same geometry and topology, increasing the mesh size from 6.9 to 9.5 million, are employed to validate the multi-dimensional delta trim method, and labeled coarse, medium, respectively. The medium grid system uses the same blade grid as the coarse grid system but finer background and wake grids.

In detail, the blade grid has the grid cells of 292 (chordwise) $\times$ 132 (spanwise) $\times$ 60 (normal). The different background and wake grid spatial resolution details are summarized in Table 3.7 and Table 3.8, respectively.

Table 3.7: *Details of the background grids (t: circumferential, r: radial, z: normal, minimum spacing is outlined in terms of the airfoil section chord c).*

Mesh	N_{tot}	N_t	N_r	N_z	Δt	Δr	Δz	Label
FG1	1520640	288	63	66	0.11	0.5	0.5	Coarse
FG2	2585088	288	84	88	0.11	0.25	0.25	Medium
NG1	336960	360	36	16	0.09	0.4	0.4	Coarse
NG2	1020600	360	72	30	0.09	0.2	0.2	Medium

Table 3.8: *Details of the wake grids (minimum spacing is outlined in terms of the airfoil section chord c).*

Mesh	N_{tot}	N_X	N_Y	N_Z	ΔX	ΔY	ΔZ	Label
WG1	314184	114	106	26	0.3	0.3	0.3	Coarse
WG2	1113600	174	160	40	0.2	0.2	0.2	Medium

In this case, the original and the multi-dimensional delta trim methods are investigated. The difference between them, as listed in Table 3.9, lies on whether the additional coarse simulation is employed or not. The detailed iteration process results of the multi-dimensional method are reported in Table 3.10. The trimming process converges after four preliminary stages and two accurate stages. In contrast, four accurate stages are required for the original delta trimming procedure, as shown in Figure 3.15. The comparison of the CPU time cost for two trim methods are given in Table. 3.11. All simulations were performed on 80 cores of the high performance cluster of Politecnico di Milano, CFDHUB, made up of Intel Xeon Gold 6248 CPU with speed of 2.50GHz. Although the multi-dimensional trimming calculation requires more trim cycles to achieve convergence than the original trim method, it presents a higher computational efficiency due to the additional coarse simulation employed in the preliminary stage.

Table 3.9: *Test matrix for trim method investigation.*

Delta trim method	Grid system	Temporal resolution	Simulation type
Original	FG2 + NG2 + WG2 + BG	1° /step	Fine simulation
Multi-dimensional	FG1 + NG1 + WG1 + BG	4° /step	Coarse simulation
	FG2 + NG2 + WG2 + BG	1° /step	Fine simulation

The C_p distributions over the radial position of r/R = 0.955 at 0°, 90°, 135° and 180° azimuths are displayed in Figure 3.16, where the results with the untrimmed and trimmed control settings are compared against the measured data [121]. An evident improvement for the C_p predictions is observed in the results calculated using the trimmed control settings, particularly for the data on the leading edge of the blade upper surface, indicating that the proposed multi-dimensional delta trim method is effective.

Table 3.10: *Detailed iteration process of the multi-dimensional delta trim method.*

Trim stage	Trim cycle	Control settings			Aerodynamic coefficients		
		θ_0	θ_{1c}	θ_{1s}	C_T	C_{Mx}	C_{My}
Preliminary	0	6.14	0.9	-1.39	5.66E-03	1.95E-05	3.15E-04
	1	5.84	1.58	-1.31	5.44E-03	2.44E-06	8.41E-05
	2	5.79	1.76	-1.29	5.49E-03	2.46E-05	-1.74E-06
	3	5.68	1.73	-1.31	5.42E-03	1.31E-05	-1.75E-05
	4	5.67	1.68	-1.34	5.40E-03	8.75E-06	-9.97E-06
Accurate	0	5.67	1.68	-1.34	5.30E-03	7.14E-06	-1.31E-05
	1	5.82	1.67	-1.42	5.47E-03	6.36E-06	-8.52E-06
	2	5.72	1.63	-1.40	5.40E-03	-1.62E-06	6.64E-06
Trimmed results		5.72	1.63	-1.40	5.40E-03	-1.62E-06	6.64E-06

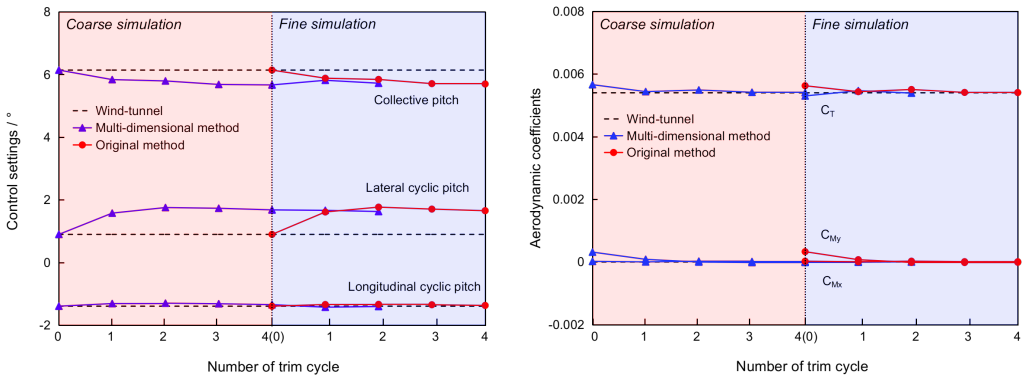

(a) *Control settings, θ_0, θ_{1c}, θ_{1s}*

(b) *Thrust and moment coefficients, C_T, C_{Mx}, C_{My}*

Figure 3.15: *Convergence history of trimming variables.*

Table 3.11: *CPU run-time of two trim methods for AH-1/OLS rotor.*

Delta trim method	Total CPU time, [h]	Relative CPU time
Original	11062 (4 trim cycles)	1.00
Multi-dimensional	9758 (6 trim cycles)	0.88 (-12 %)

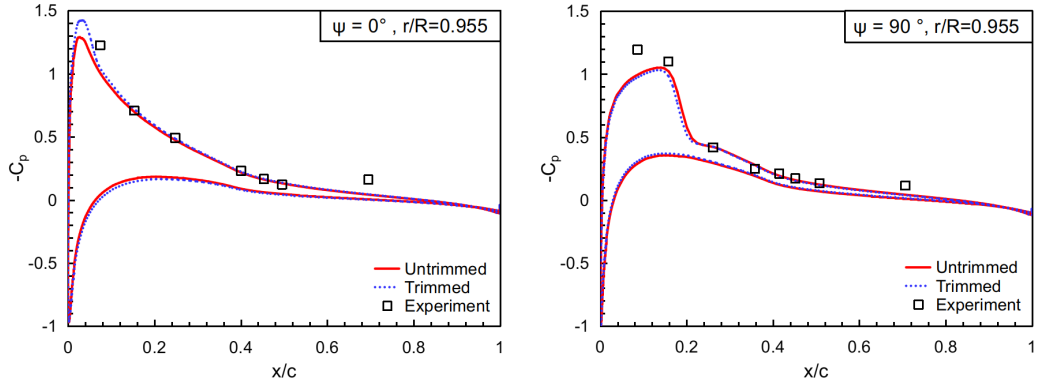

(a) $\Psi = 0°$ **(b)** $\Psi = 90°$

(c) $\Psi = 135°$ **(d)** $\Psi = 180°$

Figure 3.16: *Pressure coefficient comparisons on different blade cross-section at r/R = 0.955 for various azimuth angles.*

3.2.3 HART-II Main Rotor

Within the framework of the second Higher Harmonic Control Acoustic Rotor Test (HART-II), a highly instrumented 40% Mach scaled Bo-105 rotor test was conducted in the open 8 m $\times$ 6 m test section of the German-Dutch Wind tunnel (DNW) [122]. The aim of the HART-II program was to study the rotor wake and its development within the entire rotor disk. The baseline (BL) case of the HART-II experiment is employed as it is a descending flight dominated by BVI phenomena. More descriptions about the rotor geometry and test conditions are reported in Table 3.12.

Table 3.12: *Geometric properties and test conditions of the HART-II main rotor [122].*

N_b	4
Blade planform	Rectangular
Blade section	NACA23012mod
R	2.0 m
c	0.121 m
θ_{tw}	Linear, $-8.0°$
R_c	$0.22R$
Test point	Baseline (BL)
μ	0.15
α_s	$4.5°$
ω	109 rad/sec (M_T = 0.64)
T^{target}	3300 N
M_x^{target}	20 N· m
M_y^{target}	-20 N· m

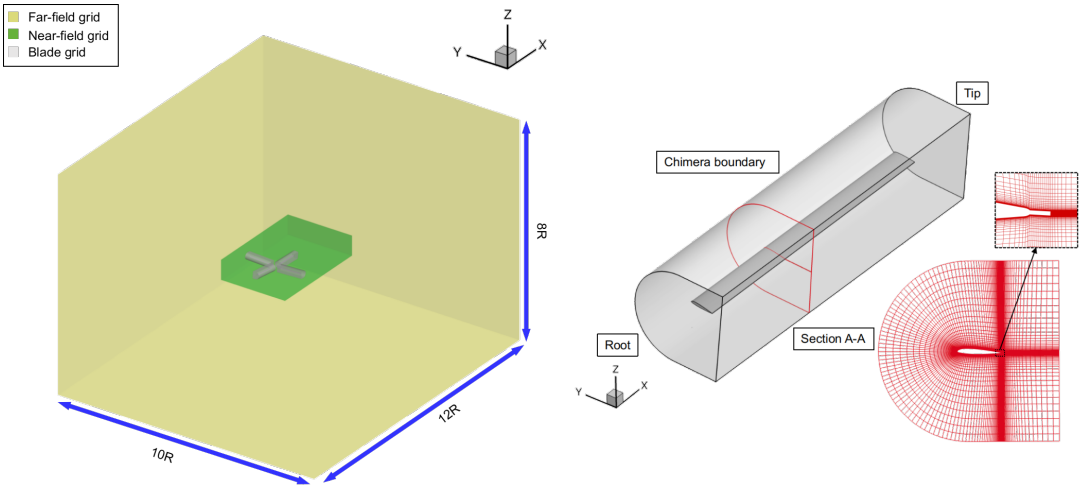

Figure 3.17: *Computational domain and detailed view of the HART-II rotor grid.*

The grid discretization is achieved using a multi-block overset grid system with Chimera technology. The grid system includes a far-field background grid, a near-field background grid, and four identical body-fitted blade grids, as depicted in Figure 3.17.

The far-field background grid is created to represent the flow domain far from the rotor. A uniform Cartesian grid is built as the near-field background grid to model the flow region close to the blades, as well as to capture the rotor wake. The body-fitted grid is created with a C-H topology type with a non-slip boundary condition on the blade surface. The wall distance y^+ value of the first layer of blade surfaces is set to less than 1.

The multi-block structured grid system for the HART-II rotor has a total of 12.6 million cells with 0.9 million cells for the far-field background grid, 6.7 million cells for the near-field background grid, and 1.2 million cells for each of the body-fitted blade grid. Meanwhile, a coarse grid system with 7.5 million cells is created for the trim process, where the far-field background grid of 0.6 million cells and the near-field background grid of 2.0 million cells. In detail, the blade grid has the grid cells of 173 (chordwise) $\times$ 125 (spanwise) $\times$ 50 (normal). The detailed grid information for background grids is summarized in Table 3.13.

Table 3.13: *Details of the background grids (t: circumferential, r: radial, z: normal, minimum spacing is outlined in terms of the airfoil section chord c).*

Mesh	N_{tot}	N_X	N_Y	N_Z	ΔX	ΔY	ΔZ	Label
FG1	573056	88	88	74	0.3	0.3	0.3	Coarse
FG2	925552	102	102	88	0.2	0.2	0.2	Medium
NG1	1992000	250	166	48	0.248	0.248	0.248	Coarse
NG2	6732000	374	250	72	0.165	0.165	0.165	Medium

For this example, all simulations were performed on 80 cores of the high performance cluster of Politecnico di Milano, CFDHUB, made up of Intel Xeon Gold 6248 CPU with speed of 2.50GHz. Table 3.14 reports the test matrix of trim method investigation for the HART-II example. Table 3.15 compares the experimental control settings and those obtained by the trim procedure. It is observed that the trimmed lateral (θ_{1c}) and longitudinal (θ_{1s}) pitch cyclic angles show good agreement with the experimental data [122], but the collective pitch angle (θ_0) is underpredicted. This may be related to the blade elastics that are not taken into account. As the trim process is managed by the BET code, the trim results are post-processed and calculated by the CFD code at each trim cycle. It should be mentioned that the BET trimmed values exactly match the trim target values at the end of trimming.

The convergence history of trim process is plotted in Figure 3.18. Table 3.16 outlines the CPU time cost for two trim methods. Although the current multi-dimensional delta trim method takes more trim cycles to achieve convergence than the original delta method, it saves approximately 31% of CPU hours as the coarse simulation is employed.

Figure 3.19 shows the trimmed behavior of CFD computations on Mach-scaled, sectional normal force C_nM^2 obtained at 87% radial station (r/R=0.87) with respect to the measurements reported in [122] and the untrimmed results computed using the experimental trim angles. As expected, the general shape of the trimmed solution is correlated much better with the experimental data than the untrimmed results, although some details of the measurements [122] are still not well reproduced due to the coarseness of the employed grid system and the neglected blade elastics. Overall the trimmed

Table 3.14: *Test matrix for trim method investigation.*

Delta trim method	Grid system	Temporal resolution	Simulation type
Original	FG2 + NG2 + BG	1° /step	Fine simulation
Multi-dimensional	FG1 + NG1 + BG	4° /step	Coarse simulation
	FG2 + NG2 + BG	1° /step	Fine simulation

Table 3.15: *Blade harmonics for the HART-II rotor.*

Case name	Baseline (BL)	Present calculation
θ_0	3.8°	2.24°
θ_{1c}	1.92°	2.03°
θ_{1s}	−1.34°	−1.28°
T	3300 N	3315.6 N
M_x	20 N·m	26.8 N·m
M_y	-20 N·m	-21.5 N·m

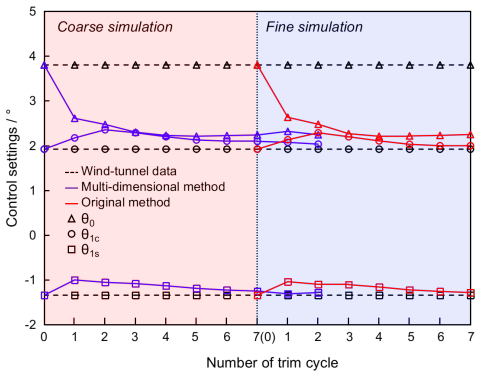

(a) *Control settings, θ_0, θ_{1c}, θ_{1s}*

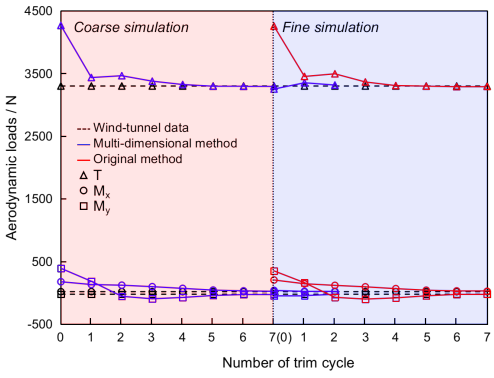

(b) *Thrust and moments, T, M_x, M_y*

Figure 3.18: *Convergence history of trimming variables.*

Table 3.16: *CPU run-time of two trim methods for HART-II rotor.*

Delta trim method	Total CPU time, [h]	Relative CPU time
Original	20846 (7 trim cycles)	1.00
Multi-dimensional	14305 (9 trim cycles)	0.69 (-31 %)

control settings could provide a satisfactory result for the simulation of the HART-II rotor in BL condition and thus can be used for further investigations.

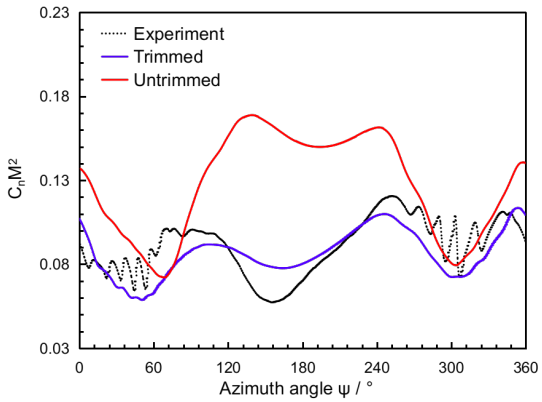

Figure 3.19: *Comparison of $C_n M^2$ variations with experiment for trimmed and untrimmed solutions.*

3.3 Validation of the Helicopter Rotor Simulation Framework

The previous sections validated every component of the helicopter rotor aerodynamic and aeroacoustic simulation framework. In this section, the objective is to evaluate the ability of the integrated framework to predict the two most representative noise sources (HSI, BVI) in helicopter rotor aeroacoustics.

3.3.1 Transonic Rotor Noise Prediction

HSI noise is the primary source for helicopter rotor noise generation in transonic conditions. It is characterized by the quadrupole volume term in the FW-H equation. The intensity of HSI noise is closely related to the size and extension of the supersonic flow pocket, which appears at the blade tip region when the tip Mach number M_T is greater than the airfoil critical Mach number M_c. The supersonic pocket extends to the far-field beyond the sonic cylinder and connects the blade to the supersonic region when shock delocalization occurs. In such situations, the integration control surface should extend as far as possible from the blade tip and enclose all the quadrupole sources in the supersonic region. The Retarded-Time formulation (Equation (2.11)) of PS-FWH equation is well suitable for weak shock delocalization cases (see Ref [123]) but it becomes unusable for strong shock delocalization cases due to the acoustic integral singularity. As previously mentioned, the Emission-Surface formulation (Equation (2.14)) can avoid the effects of Doppler singularity by introducing a much less restrictive condition in the Doppler factor and give more accurate results for the cases with strong shock delocalization.

In Ref [124], an experimental set-up from the NASA Anechoic rotor hover test chamber was conducted to investigate the HSI phenomenon. The experiment refers to a UH-1H rotor in hover condition, where the blade tip Mach number is similar to the M_T values on the advancing side achieved in high-speed forward flight. The UH-1H rotor has two straight, untwisted blades with NACA0012 airfoil section. The blade span is 1.045 m and the airfoil chord is 0.07623 m. Five test conditions with blade tip Mach number ranging from 0.85 to 0.95 were employed in the experiment. The acoustic signals were measured in the rotor disc plane. This experiment is characterized by shock delocalization phenomena and can thus be considered a very suitable dataset for transonic rotor noise prediction. In the present work, three test conditions with M_T = 0.85, 0.88, and 0.95, which respectively corresponds to no delocalized shock, weak delocalized shock, and strong delocalized shock phenomena (Figure 3.20), are used for the transonic rotor noise prediction. The noise prediction is carried out with the observer is located at 3.09 radii away from the rotor hub, laying in the rotor disc plane.

3.3.1.1 CFD Grid Sensitivity Study

The acoustic prediction is much dependent on the aerodynamic results in any CFD/FW-H hybrid method. Hence, the grid sensitivity study is performed first to obtain the grid-independent solutions. Three different blade grid resolutions with M_T = 0.85, 0.88 and 0.95 are adopted for the grid sensitivity analysis. The details of the blade grids are summarized in Table 3.17. The results are compared in terms of Cp distributions along selected blade cross-sections. Figure 3.21 shows that sufficiently converged results

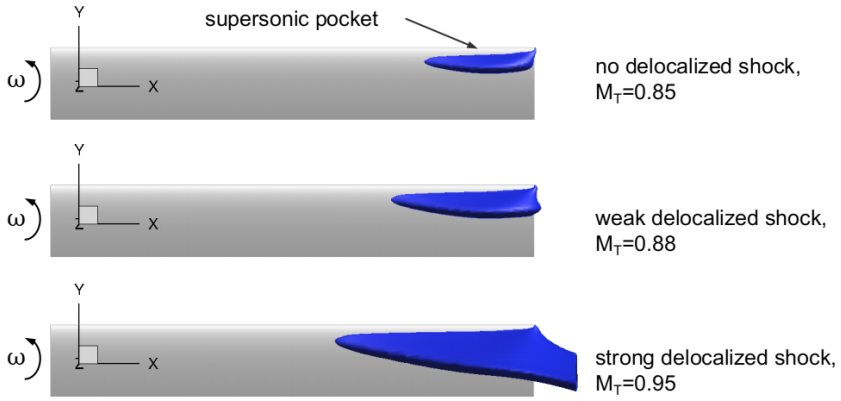

Figure 3.20: *Shock delocalization phenomena.*

are obtained with the medium grid, which is therefore used for the transonic noise prediction to guarantee precision and computational efficiency simultaneously.

Table 3.17: *Summary of the blade grids, employed for the UH-1H hovering rotor simulations*

Mesh	Blade elements				Volume cells (10^6)
	Upper	Lower	Span	Total	
Coarse	61	61	59	13942	1.7
Medium	89	89	59	19038	2.6
Fine	100	100	70	23680	3.9

3.3.1.2 Noise Prediction of M_T = 0.85 and 0.88 Cases

Two permeable control surfaces with different sizes are employed for assessing the sensitivity to the extension of the control surface. Regarding M_T = 0.85 and 0.88 cases, the control surface may be put not far away from the rotor blade as the shock delocalization phenomenon is weak. Hence, the two control surfaces employed are $S1_{cs} = (1.0, 0.5)$ and $S2_{cs} = (1.5, 0.75)$. Figure 3.22 compares the noise predictions with two permeable control surfaces and experimental data [125]. These two control surfaces are seen to predict similar results with minor discrepancy. It is demonstrated that the far-field noise predictions are not very sensitive to the choice of the numerical integration surface for both blade tip Mach numbers. Overall, the computed results have good agreement with the experimental noise measurements, although a slightly underpredicted negative peak pressure appears for the weak delocalized shock case (M_T = 0.88).

3.3.1.3 Noise Prediction of M_T = 0.95 Case

When it comes to the significant shock delocalization case (M_T = 0.95), the integration control surface should be placed far away from the blade to enclose all the transonic flow regions. In order to analyze the sensitivity of the numerical solution provided by

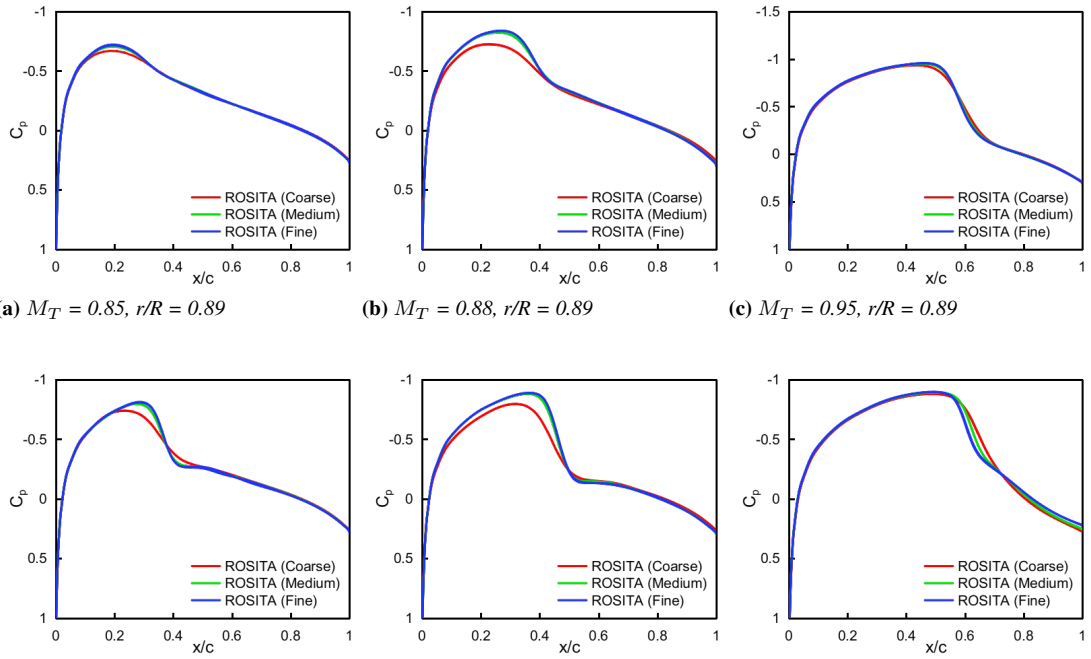

(a) M_T = 0.85, r/R = 0.89 **(b)** M_T = 0.88, r/R = 0.89 **(c)** M_T = 0.95, r/R = 0.89

(d) M_T = 0.85, r/R = 0.96 **(e)** M_T = 0.88, r/R = 0.96 **(f)** M_T = 0.95, r/R = 0.96

Figure 3.21: *Cp distributions on two blade cross-sections for UH-1H rotor in hover mode.*

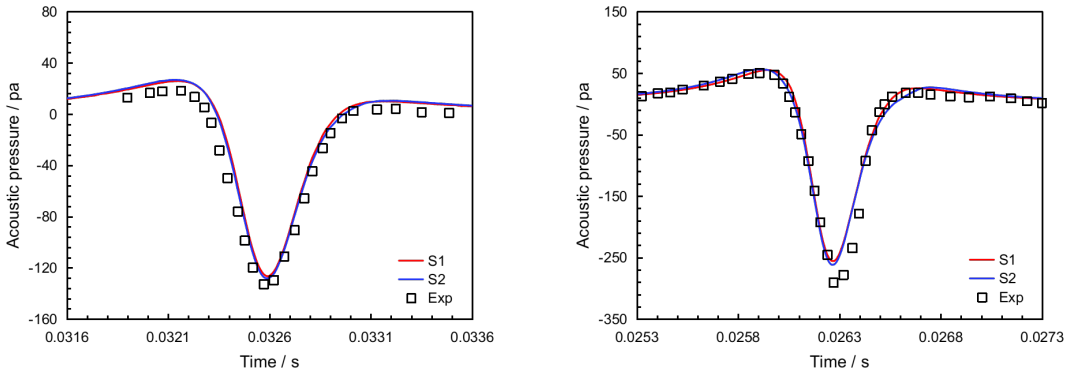

(a) M_T = 0.85 **(b)** M_T = 0.88

Figure 3.22: *Predicted acoustic pressure comparison of different permeable control surfaces and experimental results.*

the MCES algorithm to the extension of control surface, six noise predictions with different sizes of control surface are carried out, as presented in Figure 3.23. The control surface $S_{cs} = (0.5, 0)$ corresponds to the blade surface, the noise prediction is exactly provided by the IS-FWH formulation. Some undesirable impulses appeared on the predicted waveform as the control surface moves away from the blade. Further increasing the size of the control surface, these fluctuations are eliminated and the convergence of the result is reached with the control surface $S_{cs} = (7.5, 1.25)$. These undesirable peaks may be due to the Λ singularity behavior.

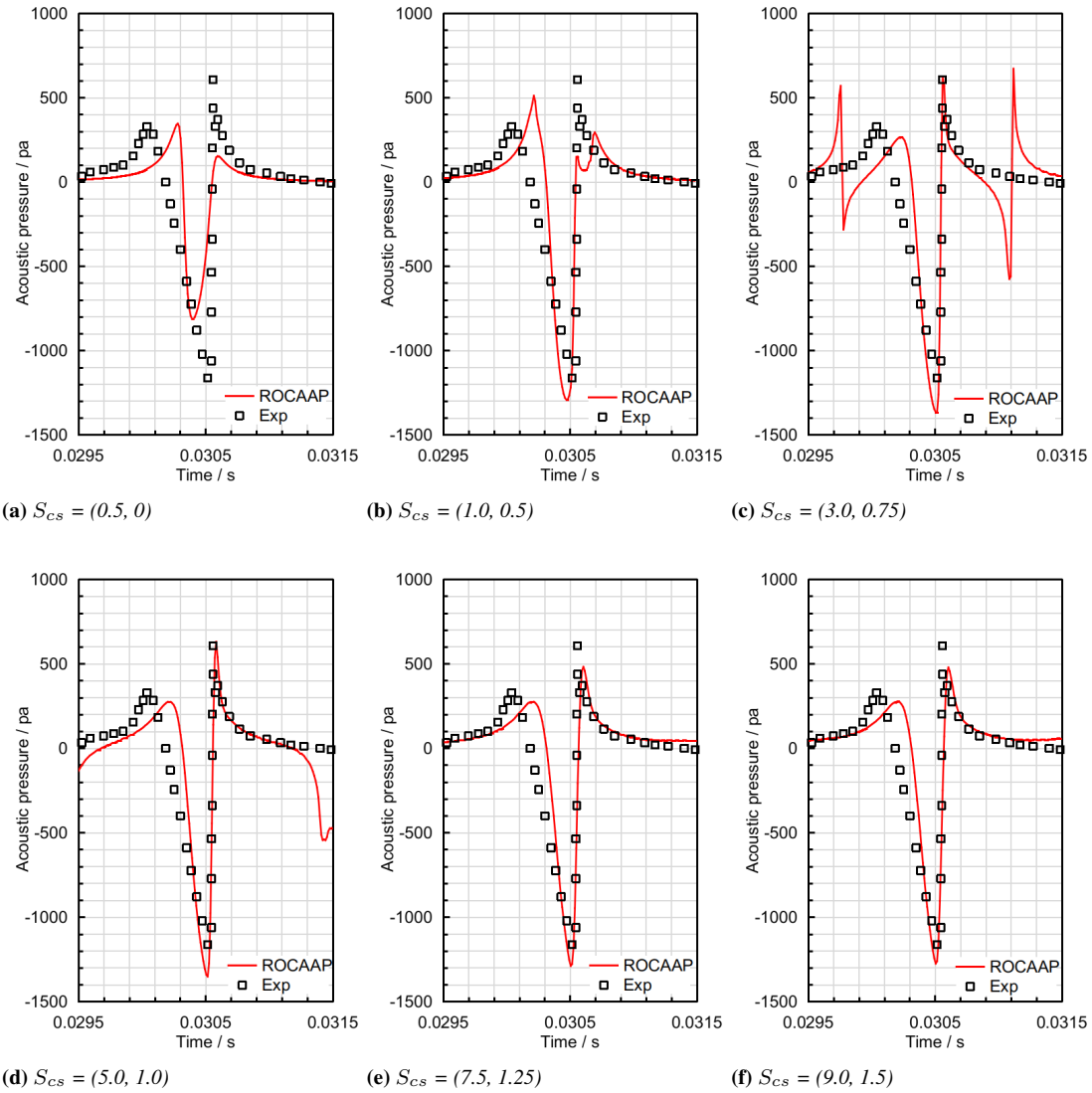

(a) S_{cs} = *(0.5, 0)* **(b)** S_{cs} = *(1.0, 0.5)* **(c)** S_{cs} = *(3.0, 0.75)*

(d) S_{cs} = *(5.0, 1.0)* **(e)** S_{cs} = *(7.5, 1.25)* **(f)** S_{cs} = *(9.0, 1.5)*

Figure 3.23: *Comparisons of the numerical prediction with respect to the extension of control surface for strong shock delocalization case, M_T = 0.95.*

In Figure 3.24, the predictions are compared with the experimental data [125] and the solutions of K-Algorithm [101] and EPS method [102]. The results agree overall with the measurements and the solutions calculated by the other two formulations. However, it may be observed that the negative peak pressure and the slope in the first

pressure drop exhibit a slight difference. These differences may be attributed to the CFD input data because the CFD grid was not refined in the direction of the delocalized supersonic region. Nevertheless, the predicted noise signals show good agreement with the experiment in terms of the typical asymmetric waveform and the negative peak pressure. It is confirmed that the presented helicopter simulation framework is capable of capturing both good peaks and shapes in the acoustic signal of the transonic rotor noise when the high shock delocalization occurs.

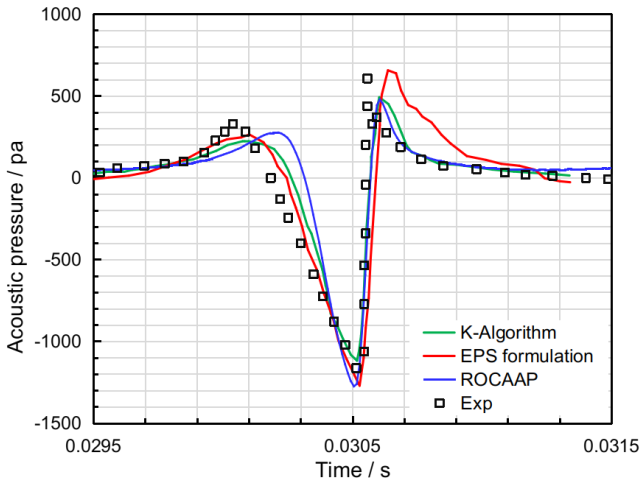

Figure 3.24: *Noise prediction comparisons of different methods for M_T = 0.95.*

3.3.2 BVI Noise Prediction

This part mainly concentrates on assessing the integrated framework to predict helicopter rotor BVI noise. In what follows, the acoustics of the AH-1/OLS rotor at 10014 test point [120] will be presented. This test condition is characterized by a low-speed descending flight with strong BVI phenomena and can thus be considered very suitable case for BVI rotor noise prediction.

The microphone locations in the AH-1/OLS acoustic test are shown in Figure 3.25. Mic $\#2$, $\#6$, and $\#8$ are placed in the rotor disk plane at $3.44R$ from the rotor hub to measure the HSI noise signal; the azimuths are $180°$, $150°$ and $210°$, respectively. Mic $\#3$, $\#7$, and $\#9$ are installed $30°$ below the rotor disk plane with 3.44 radii away from the rotor hub for BVI noise measurement; the azimuths are $180°$, $150°$ and $210°$, respectively. The coordinates for each microphone position are reported in Table 3.18. In this part, we are only interested in the observer positions for BVI noise measurement.

The trimmed control settings for the test point 10014 were calculated on different grid discretizations in section 3.2.2. The present work applied the medium resolution grid with the trimmed values to obtain the input data for noise prediction. The ROSITA CFD solver is run for four revolutions with a small temporal resolution of $0.25°$ azimuth increment (1440 steps per rotor revolution) to capture the highly unsteady airloads.

As previously stated, the Retarded-Time formulation is suitable for subsonic noise source cases. Therefore, this formulation is applied in the present case for BVI noise prediction. The predicted results are compared with the experimental measurements

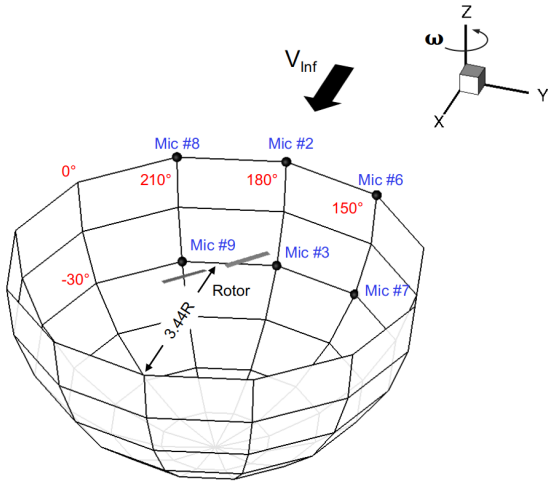

Figure 3.25: *Microphone positions in the AH-1/OLS acoustic test [120].*

Table 3.18: *Coordinates of microphones in the AH-1/OLS acoustic test [120].*

Microphone	X (m)	Y (m)	Z (m)	Noise type
#2	-3.295	0.0	0.0	
#6	-2.854	1.648	0.0	HSI noise
#8	-2.854	-1.648	0.0	
#3	-2.854	0.0	-1.648	
#7	-2.472	1.427	-1.648	BVI noise
#9	-2.472	-1.427	-1.648	

[120]. Figure 3.26 shows the acoustic predictions with the impermeable data surface ($S_{cs} = (0.5, 0.0)$) and the permeable data surface ($S_{cs} = (1.0, 0.5)$) at the microphone positions of $\#3$, $\#7$, $\#9$. In all three positions, the permeable surface results compare slightly better with the experimental data than the impermeable surface results. Both calculations could predict the general shape of the noise signal but miss the high-frequency BVI oscillations. The discrepancies may be attributed to the over-diffused vortices in the rotor wake because the grid resolution is not satisfactory enough.

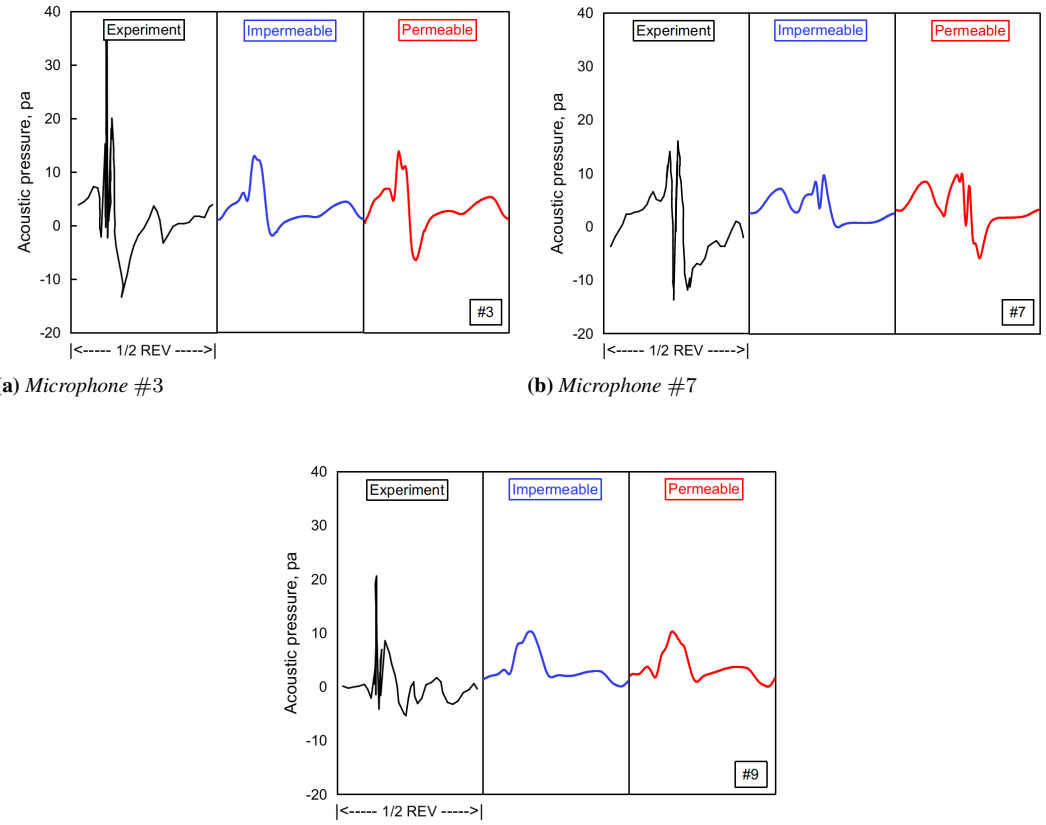

(a) *Microphone* $\#3$

(b) *Microphone* $\#7$

(c) *Microphone* $\#9$

Figure 3.26: *Predicted acoustic pressure at three microphone positions compared with experiment of the AH-1/OLS main rotor [120]. The plots showcase the computed acoustic pressure with impermeable and permeable control surfaces.*

3.4 Summary

This chapter presented the validations of acoustic methods, rotor trim method and integrated simulation framework. The main conculsions can be drawn as follows:

- In the Emission-Surface formulation, the ability of Marching-Cube algorithm on emission surface construction is well demonstrated through the supersonic rotational blade planform and the transonic cylindrical strip.
- The ROCCAP validation results on the non-realistic stationary spherical surface

and two-bladed UH-1 forwarding flight case have shown very good agreement with analytical solution and WOPWOP results, respectively.

- The multi-dimensional delta trim method was first examined. The trim method is capable of obtaining the control angles with prescribed target thrust and moments for the helicopter rotor in forwarding flight conditions. With the multi-dimensional trim method, the efforts required to reach the trimmed state were significantly reduced with respect to the original trim method. This tool was used throughout the thesis to assist in simulating the helicopter forwarding flight cases to validate the BVI noise prediction.
- The simulation framework for helicopter rotor aerodynamics and aeroacoustics were validated. The PS-FWH equation with MC Emission-Surface formulation was first developed and was proven well-suited for helicopter transonic rotor noise prediction. The Retarded-Time formulation was successfully applied to BVI noise prediction and obtained the general shape of the noise signals. Overall, the proposed CFD/PS-FWH framework has shown good capability for helicopter rotor HSI and BVI noise prediction.

CHAPTER 4

Vortex Feature-Based VC2 Model Development and Applications

The partial content of this chapter is published in Jinbin Fu, Yi Yuan, Luigi Vigevano. **Numerical investigations of the vortex feature-based vorticity confinement models for the assessment in three-dimensional vortex-dominated flows**. *Meccanica*. (57)2022: 1657-1676. DOI:10.1007/s11012-022-01525-5.

This chapter introduces a locally normalized vortex feature-based VC2 model to improve the vortex resolution in aerodynamic wakes with moderate computational cost. In this method, the VC2 scheme with two well-known vortex feature detection methods (non-dimensional Q criterion, non-dimensional λ_2 criterion) is employed to counterbalance the truncation error introduced by the numerical discretization of the convective term. The flow applications of the underlying model to four benchmark cases are presented in section 4.3. Then, section 4.4 gives the acoustic analysis of the results obtained with this model. The original VC2 method and the two vortex feature-based vorticity confinement methods are briefly referred as OVC2, FVC2-Q, and FVC2-L2.

The key results and novelties of this chapter are the detailed assessment of the vortex feature-based VC2 models for three-dimensional vortex-dominated flows, particularly helicopter rotor flows, in terms of both aerodynamics and aeroacoustics.

4.1 Description of Original VC2 Model

In the past, Steinhoff proposed two famous vorticity confinement schemes, called VC1 [61] and VC2 [63], respectively. In this work, the VC2 scheme, which has the advantage of making momentum conservative and not singular at the vortex center, is adopted for the preservation of vorticity in vortex-dominated flows.

The implementation of the VC2 scheme is based on the experience accumulated

with the VC1 scheme, that is, the confinement term is added to the momentum equation alone as a body force term $\boldsymbol{F_b}$. This approach is preferred because far better results are obtained when the vorticity confinement term is removed from the energy conservation equation [65]. The expression of $\boldsymbol{F_b}$ may be written as:

$$\begin{aligned} \tilde{\omega} &= \mid \boldsymbol{\omega} \mid + \epsilon \\ \boldsymbol{w} &= \frac{\boldsymbol{\omega}}{\tilde{\omega}} \left[\frac{\sum_{n=1}^{N} (\tilde{\omega}_n)^{-1}}{N} \right]^{-1} \\ \boldsymbol{F_b} &= \nabla \times \varepsilon \boldsymbol{w} \end{aligned} \tag{4.1}$$

where the quantity ϵ is a small positive value to prevent division by 0 in $\boldsymbol{w}$. The vector $\boldsymbol{w}$ can be interpreted as the locally normalized vorticity vector multiplied by the harmonic mean of vorticity magnitude. The harmonic mean is calculated over a localized stencil of N cells; for a uniform hexahedral mesh, N = 7, which involves the center cell and six neighboring cells. ε is the confinement parameter which is a positive coefficient. The ε values used in this work come from a trial and error procedure. The vorticity magnitude is defined as follows:

$$\omega_x = \frac{\partial w}{\partial y} - \frac{\partial v}{\partial z}, \;\; \omega_y = \frac{\partial u}{\partial z} - \frac{\partial w}{\partial x}, \;\; \omega_z = \frac{\partial v}{\partial x} - \frac{\partial u}{\partial y} \tag{4.2}$$

$$\mid \boldsymbol{\omega} \mid = \sqrt{\omega_x^2 + \omega_y^2 + \omega_z^2} \tag{4.3}$$

With the expression of $\boldsymbol{F_b}$, the modified source term $\overline{\boldsymbol{F}}_{\boldsymbol{s}}$ for the compressible confinement formulation is modified as:

$$\overline{\boldsymbol{F}}_{\boldsymbol{s}} = \begin{bmatrix} 0 \\ \boldsymbol{F_s} - \rho \cdot \boldsymbol{F_b} \\ 0 \end{bmatrix} \tag{4.4}$$

4.2 Feature Detection of Vortical Flow Regions and Cut-Off

In this section, two well-known vortex feature detection methods are introduced: Q-criterion, and λ_2-criterion methods. Both methods are presented in non-dimensional forms by imposing a normalization with the local shear-strain rate. The vortex feature detection approaches establish a threshold function, $f_{threshold}$, for identifying the vortex. This function is evaluated at each grid cell, and a vortex is recognized if the $f_{threshold}$ value overtakes a predetermined value.

4.2.1 Non-Dimensional Q

Ref [126] identified the vortex structure in flow regions with a positive second Galilean invariant (Q) of velocity gradient tensor $\nabla \boldsymbol{u}$. Q is expressed as the difference of Frobenius norm between the asymmetric tensor Ω and symmetric tensor S with the following

expression:

$$Q = \frac{1}{2}\left(\| \Omega \|_F^2 - \| S \|_F^2\right) \tag{4.5}$$

where S and Ω can be respectively written as

$$S = \frac{1}{2}\left[\nabla \boldsymbol{u} + (\nabla \boldsymbol{u})^T\right]; \quad \Omega = \frac{1}{2}\left[\nabla \boldsymbol{u} - (\nabla \boldsymbol{u})^T\right] \tag{4.6}$$

As the Q value is still dependent on the local characteristic length and velocity, a suitable non-dimensional form is obtained by dividing the equation (4.5) by $\| S \|_F^2$. The resulting threshold function becomes

$$f_{threshold} = \frac{1}{2}\left(\frac{\| \Omega \|_F^2}{\| S \|_F^2} - 1\right) \tag{4.7}$$

According to the criterion, vortices are identified where the value of the threshold function $f_{threshold}$ is greater than zero.

4.2.2 Non-Dimensional λ_2

The λ_2 criterion for the identification of vortex was first proposed by Ref [127]. By neglecting the viscosity and transient terms, the incompressible Navier-Stokes equation turned into an eigenvector-eigenvalue problem as

$$[S^2 + \Omega^2 - \lambda_i I]X_i = 0 \tag{4.8}$$

The λ_2 criterion evaluates the second largest eigenvalue of the symmetric tensor $S^2 + \Omega^2$, namely λ_2. A vortex is then detected with the condition of $\lambda_2 < 0$. Similar to the non-dimensional Q criterion, $\| S \|_F^2$ is used to normalize the non-dimensional λ_2 criterion. The threshold function can be written as

$$f_{threshold} = -\frac{\lambda_2}{\| S \|_F^2} \tag{4.9}$$

where a vortex is obtained with a positive threshold value ($f_{threshold} > 0$). In this work, since the $S^2 + \Omega^2$ is real and symmetric, the eigenvalues can be readily calculated by the non-iterative algorithm, presented in Ref [128].

4.2.3 Application of the Cut-Off

In original VC2 model, the non-zero vorticity magnitude is used as the factor for vortex identification. It means that the VC term is computed at each point in solution domain where the vorticity magnitude is not equal to zero. However, using vorticity magnitude to define a vortex structure is not adequate. It will not provide the correct results in the areas where the vorticity magnitude is non-zero but there is no vortex, like in the boundary layer, for instance. To eliminate this problem, the aforementioned vortices identification criteria are employed to avoid the application of confinement inside the boundary layer.

The activation of the VC2 model is managed by flagging cells in which the $f_{threshold}$ overtakes a predefined cut-off value f_0. That can be expressed as:

$$\beta_{\mathtt{ijk}} = \begin{cases} 1, & f_{threshold} > f_0 \\ 0, & \text{otherwise} \end{cases} \tag{4.10}$$

Afterward the VC2 source term with application of the cut-off may be rewritten as

$$[F_b]_{ijk} = \beta_{ijk} \left[\nabla \times \varepsilon \boldsymbol{w}\right]_{ijk} \tag{4.11}$$

For all computations in this paper, the dimensional cut-off value is set to f_0 = 0.5.

4.3 Flow Applications

This section considers three practical test cases to analyze the VC2 model with different vortex feature detection formulations in detail. In the first two cases of the NACA0015 wing and the Caradonna-Tung hovering rotor, the performance of the original and the vortex feature-based VC2 models are evaluated in terms of aerodynamic prediction, vorticity preservation, computational stability, and computational efficiency. The last part contains the solutions of the HART-II rotor flow in low-speed descending flight.

4.3.1 Three-Dimensional NACA0015 Wing

The flow around the NACA0015 wing with square tips is now considered to demonstrate the performance of the implemented VC models with the Navier-Stokes equations. Numerical simulations without any VC models are also undertaken for comparison.

The determination of the value of the confinement parameter ε is the critical issue in applying the VC models for a given discretization, a too large constant ε value may lead to some robustness problems in the simulation. On the other side, a small value may have an insignificant effect on the vorticity confinement. In this work, the ε values were carefully determined by a trial and error procedure, seeking, for the given discretization, the largest value which allows to obtain a reduction of the residuals of at least three orders of magnitude. The values so obtained were considered as reference values.

In Ref [129], an experimental campaign was conducted in the 7×10-Foot subsonic wind tunnel at NASA Ames to measure the NACA0015 wing pressure and trailing vortex. The experiment refers to a NACA0015 wing with aspect ratio of $AR = 6.6$ and chord length of $c = 0.52m$ at different operation conditions. In this work, the selected test case is operated under the condition of $\alpha = 12°$, $M = 0.1235$, and $Re = 1.5 \times 10^6$.

The computational domain for the study of the NACA0015 wing case is shown in Figure 4.1. In stream-wise direction, the inflow section was located at $12c$ from the leading edge of the wing, the outflow section was placed at a distance of $19c$ from the trailing edge of the wing. The far-field boundary was extended up to $9c$ from the wingtip in the spanwise direction and to $7c$ from the wing surface in the normal direction. The overset grid system using the Chimera technology was adopted to discrete the computational domian. It consists of a background grid, a vortex grid and a near-body wing grid (see Figure 4.2). The background grid was discretised with an H topology. An intermediate vortex grid was extended up to $6c$ from the trailing edge to maintain the integrity of the stream-wise vortex. The near-body wing grid was built with a C-H topology. The wall distance of the first layer of body surfaces was set to $1 \times 10^{-5}c$ so that the y^+ value was less than 1. A non-slip boundary condition was applied on the NACA0015 wing surface. The zipped-grid technique [130] was employed on overlapping surface grids to deal with the wing root configuration with no gap between the wing root section and the wind tunnel wall.

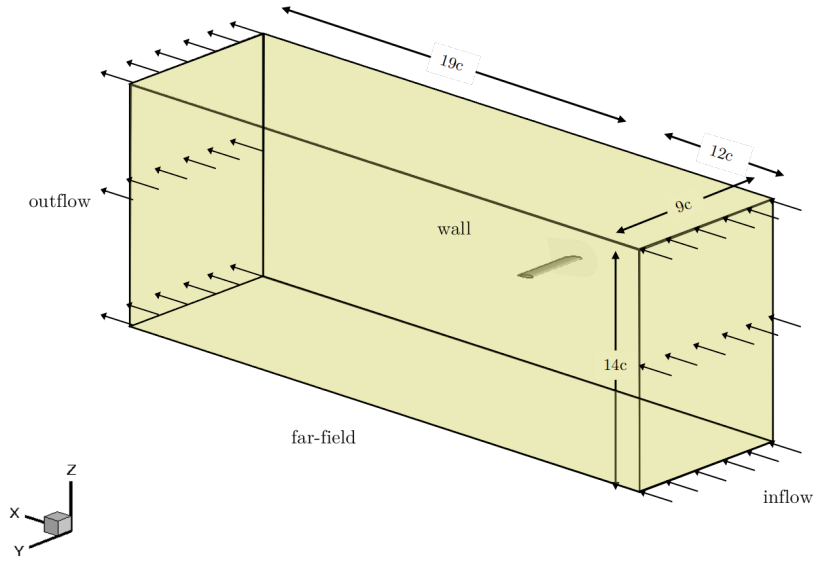

Figure 4.1: *Computational domain for NACA0015 wing case.*

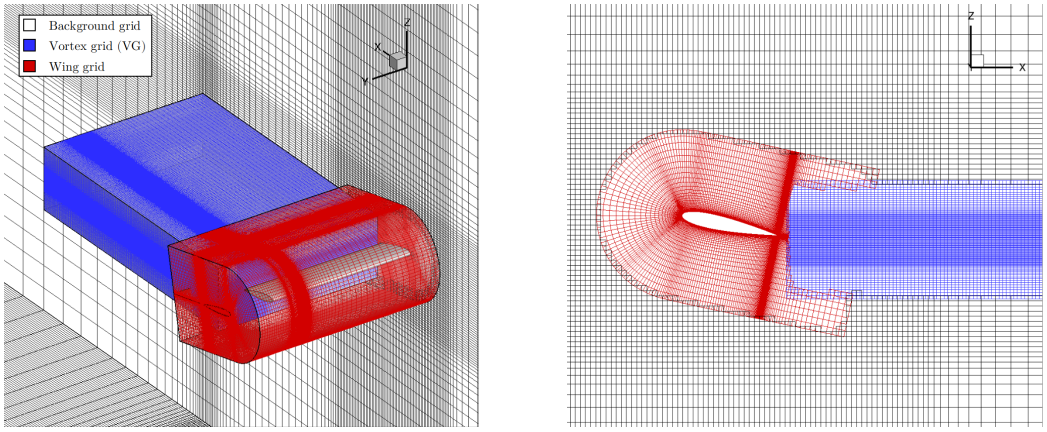

(a) *Overset grid system* **(b)** *Cross-section view of the overset grid system*

Figure 4.2: *The computational grid of the NACA0015 wing case.*

To account for the grid spatial resolution effects on aerodynamic loads prediction, different wing meshes on the same geometry and topology were employed with cell densities increasing from 1.33 to 5.96 million. Details of grid discretization information are reported in Table 4.1 for background and vortex meshes and in Table 4.2 for wing mesh.

4.3.1.1 Grid Sensitivity Study

A grid sensitivity study was conducted first for the wing mesh with three different grid spatial resolutions, namely coarse, medium and fine (see Table 4.2). The simulations

Table 4.1: *Details of the background and vortex grids (Minimum spacing is outlined in terms of airfoil section chord c).*

Mesh	N_{tot}	N_X	N_Y	N_Z	ΔX($\times 10^{-3}$)	ΔY($\times 10^{-3}$)	ΔZ($\times 10^{-3}$)
Background	1545480	159	108	90	50	50	52
Vortex	2528800	160	145	109	37.5	7.5	7.5

Table 4.2: *Details of the wing grid (ξ: chord-wise, ζ: span-wise, η: normal, minimum spacing is outlined in terms of airfoil section chord c.)*

Mesh	N_{tot}	N_ξ	N_ζ	N_η	$\Delta\xi(\times 10^{-3})$	$\Delta\zeta(\times 10^{-3})$	$\Delta\eta(\times 10^{-3})$
Coarse	1333504	220	124	40	1.8	0.15	0.01
Medium	3556000	300	165	60	1.02	0.1	0.01
Fine	5957951	358	181	75	0.6	0.05	0.01

were performed at two test conditions with $\alpha = 8^\circ$ and 12° to assess the accuracy of the predicted aerodynamic loads. A quantitative analysis of the grid sensitivity of the solutions is reported in Figure 4.3. In this figure, C_L and C_D values are compared with the data measured from wind tunnel [129]. The comparisons show that all computed C_L values are slightly lower than the experimental data, small differences between CFD results can be appreciated for the C_L values. However, the C_D value computed by the coarse grid is significantly different from the results of the medium and fine grids. A weak sensitivity on the grid resolution can be observed for the computed C_L and C_D values, especially for the medium and fine grids. Therefore, the spatial discretization of the medium grid can be considered for further analysis to guarantee precision and computational efficiency simultaneously.

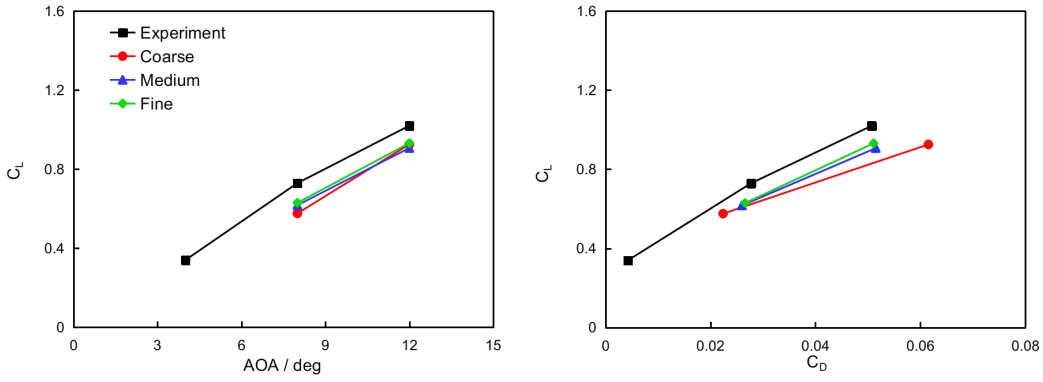

(a) C_L - AOA **(b)** C_L - C_D

Figure 4.3: *Grid sensitivity study.*

4.3.1.2 Effect on Computational Stability

Regarding the stability of each VC model, Figure 4.4 shows the convergence histories of flow solution residual at ε = 0.002, 0.005 and 0.02, as well as the lift coefficient at ε = 0.02. The data of the non-VC model case is used for comparison. All flow solutions

were simulated using the RANS equations, coupled with the Spalart-Allmaras turbulence model. The governing equations were integrated with the implicit dual-time stepping method of ROSITA, using a pseudo-time Courant-Friedrichs-Lewy (CFL) number equal to 3.0. From Figure 4.4a to 4.4c, it is observed that the residuals of the OVC2 model go up as the value of the confinement parameter ε increases. It indicates that the stability of the OVC2 model case gradually worsens as the ε value is increasing. In contrast, the stability of the calculations carried out with two vortex feature-based VC2 (FVC2-Q and FVC2-L2) models could be better preserved for all tested ε values, although there are minor differences between them when $\varepsilon = 0.02$. More detailed stability behavior of VC models on the C_L characteristic is plotted in Figure 4.4d. In this example, an irregular oscillation can be observed with the OVC2 model, whereas the cases with the two vortex feature-based VC models provide periodic solutions. This discrepancy of the convergence history expresses a potential advantage of the vortex feature-based VC models in maintaining the robustness of the original ROSITA solver. From above analysis, the reference value of the confinement parameter ε could be determined: $\varepsilon_o = 0.002$ for the OVC2 model, $\varepsilon_o = 0.02$ for both the FVC2-Q and FVC2-L2 models.

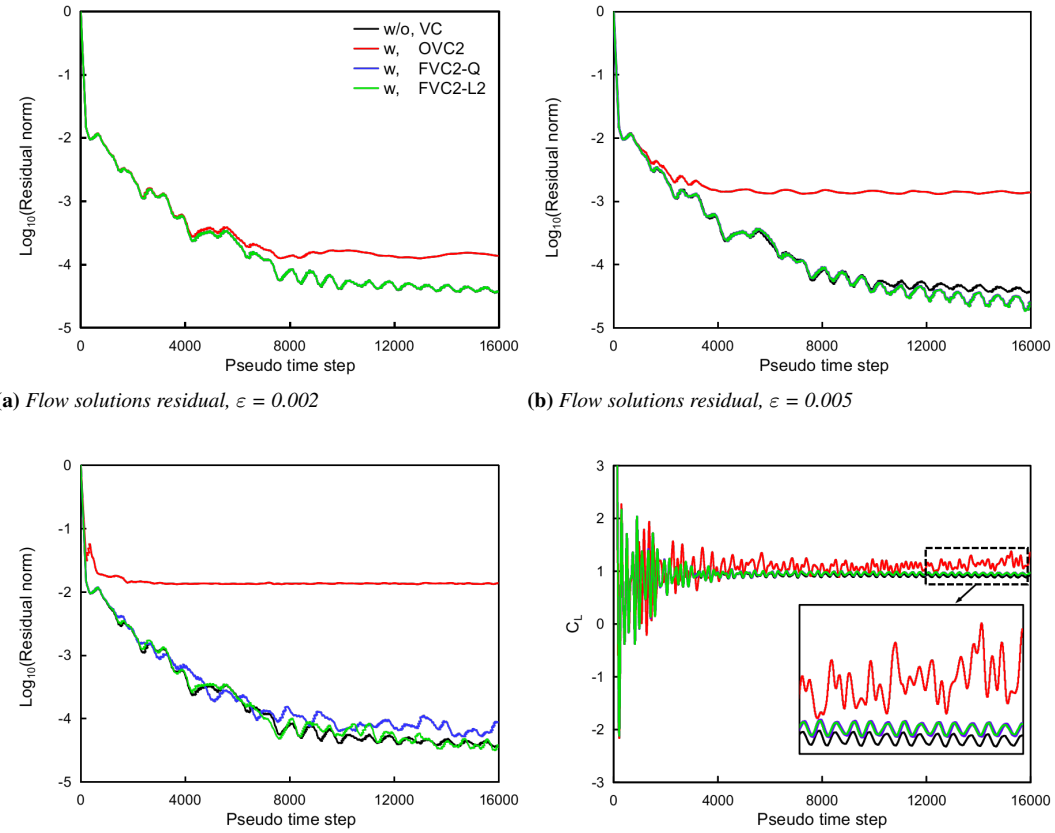

(a) *Flow solutions residual, $\varepsilon = 0.002$*

(b) *Flow solutions residual, $\varepsilon = 0.005$*

(c) *Flow solutions residual, $\varepsilon = 0.02$*

(d) *Lift coefficient, $\varepsilon = 0.02$*

Figure 4.4: *Convergence history of the NACA0015 wing for the cases with and without VC models.*

4.3.1.3 Influence on Aerodynamic Loads Prediction

Different VC models have been tested to check the consistency of the aerodynamic loads (C_L, C_D, and C_M), when the reference ε parameters were applied. Due to the slightly oscillation behavior of the solutions, an average procedure was activated over 250 pseudo time steps at the end of the calculations.

In Figure 4.5, the computed sectional distribution of the aerodynamic loads along the wing span are compared against the measured wind-tunnel data [129]. It appears that, for the reference ε value, although a good prediction of the sectional C_L distribution is obtained by the OVC2 model case, the C_D distribution is overestimated and the C_M distribution is underestimated due to the application of confinement inside the boundary layer. Nevertheless, two vortex feature-based VC2 models provide more acceptable and robust results with minor discrepancies between them and with the simulation without VC. These improvements may be explained as the over-confinement in the boundary layer region is avoided by introducing the vortex feature-detection methods.

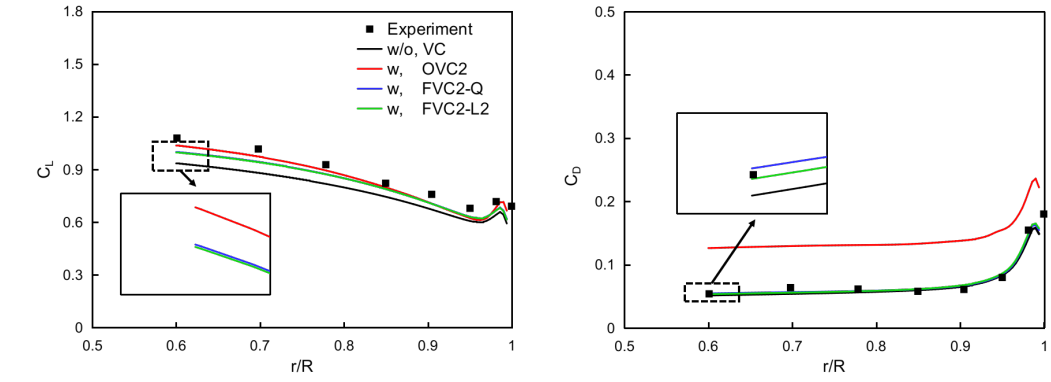

(a) C_L **(b)** C_D

(c) C_M

Figure 4.5: *Effect of different VC models on wing span aerodynamic loads.*

4.3.1.4 Effect on Vorticity Preservation

The contours of vorticity are plotted at five chordwise stations (x/c = 0.05, 0.25, 0.45, 0.65, 0.85), as illustrated in Figure 4.6. Figure 4.7 presents the formation procedure of

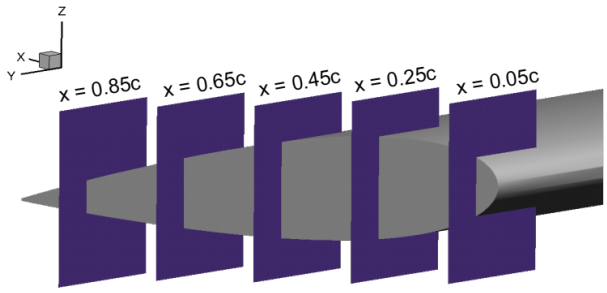

Figure 4.6: *Vorticity contour plots at five chordwise stations.*

wing-tip vortex structures at the onset phase calculated by different VC models with the reference ε value and non-VC model with $\varepsilon = 0.0$. Two strong vortex systems, one from the suction side of the wing-tip and the other associated with the pressure side of the wing-tip, are shown. The improvement of vorticity for both two vortex systems could be seen from the solutions of the OVC2, FVC2-Q, and FVC2-L2 models. Meanwhile, compared with the OVC2 model case, the vortex feature-based VC2 models present better behavior of vorticity preservation.

Figure 4.8 shows iso-surface of Q criterion at Q = 0.8 with the reference ε used. It is clear that the stream-wise vortex shedding from the wing-tip is preserved much better by the vortex feature-based VC2 models. In addition, the FVC2-L2 model provides an almost identical distance of the downstream tip vortices with the FVC2-Q model. As for the OVC2 model case, although the downstream tip vortices are preserved better than the non-VC model, the vortices diffused much faster than the vortex feature-based VC2 models.

The normalized z-velocity through the wingtip vortex core is one of the indices to evaluate the performance of the VC models. The velocity profile is extracted by a line passing through the vortex core parallel to the span-wise direction, as indicated by Figure 4.9. Figure 4.10 further quantify the improvement of the VC models on vorticity preservation by comparing the swirl velocity profile recorded at two- and four-chord lengths downstream of the trailing edge with measurements. As state previously, the OVC2 model presents the improved velocity profile but a fast diffusion downstream. In contrast, the vortex feature-based VC2 models are able to offer more desirable values. In addition, the improvement in the predicted maximum z-velocity for the vortex feature-based VC2 models are apparent with respect to the non-VC model. For example, at two chords downstream, the solutions of the FVC2-Q and FVC2-L2 models have increased the maximum z-velocity value by 43.9% and 44.3%, respectively, compared with the non-VC model. At location of four chords downstream, the increase becomes 32.4% and 33.1%, respectively. It can be said that the vortex feature-based VC2 models have somehow more robust values than the OVC2 model. Furthermore, these results demonstrate that the vortex feature-based VC2 approaches have better performance on vorticity preservation than the OVC2 model.

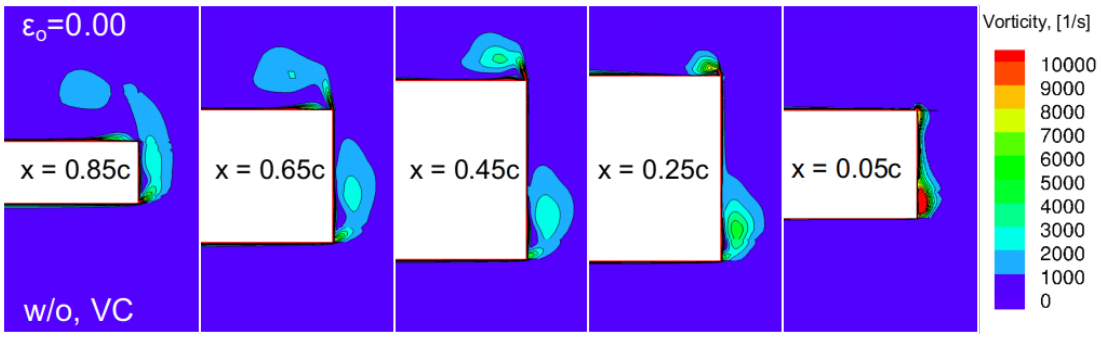

(a) *w/o, VC model, ε = 0.0*

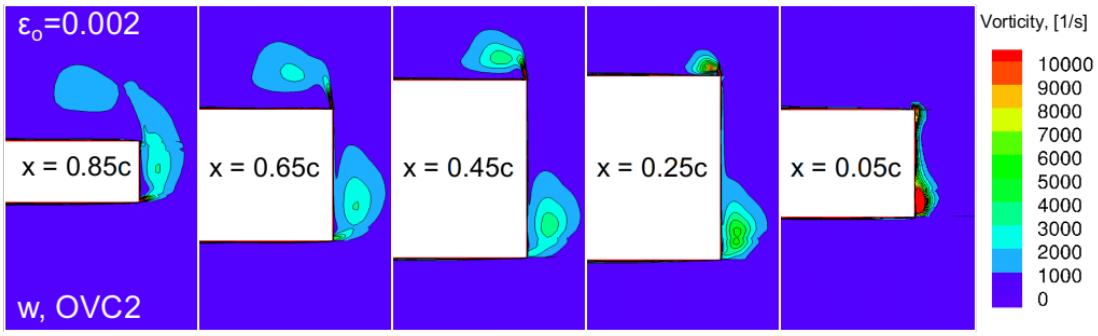

(b) *w, OVC2 model, ε_o = 0.002*

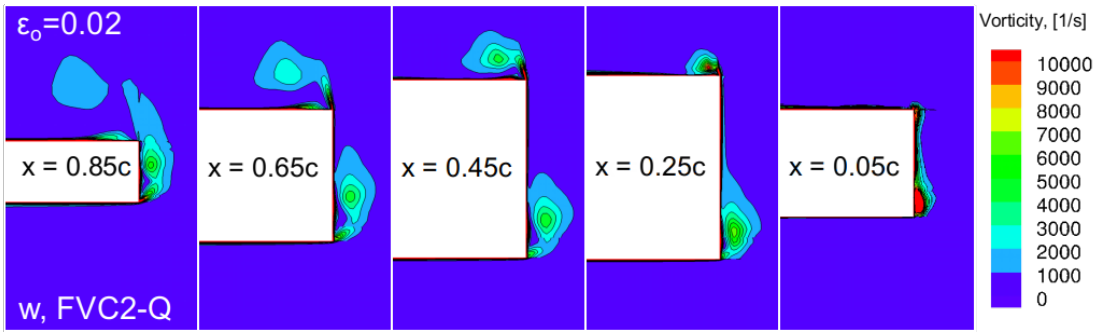

(c) *w, FVC2-Q model, ε_o = 0.02*

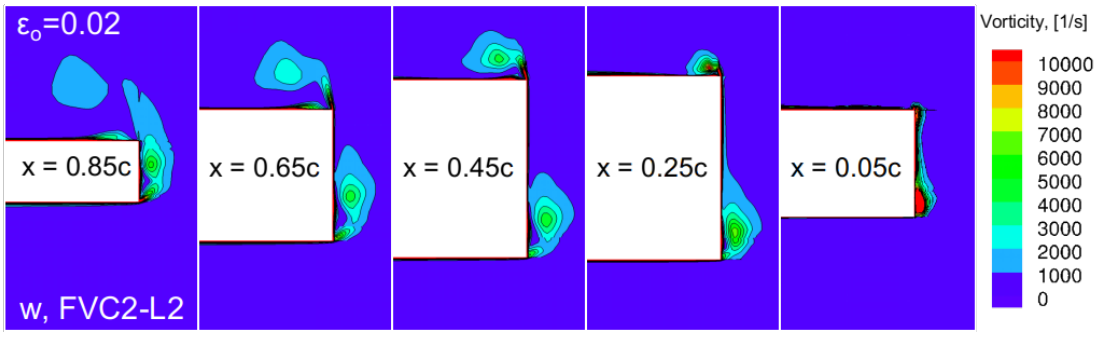

(d) *w, FVC2-L2 model, ε_o= 0.02*

Figure 4.7: *Formation process of wing-tip vortex.*

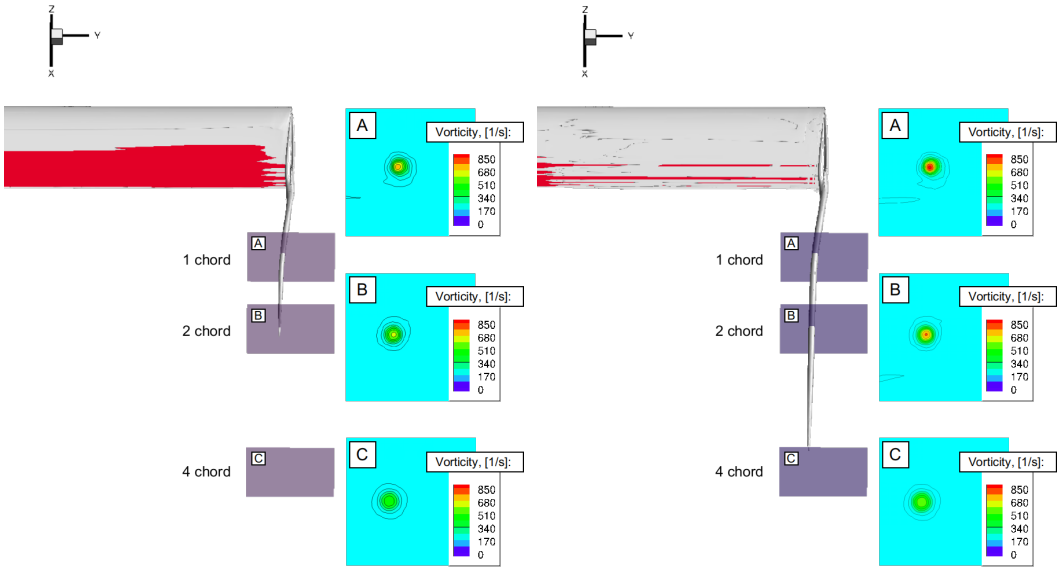

(a) *w/o, VC model, ε = 0.0*

(b) *w, OVC2 model, ε_o = 0.002*

(c) *w, FVC2-Q model, ε_o = 0.02*

(d) *w, FVC2-L2 model, ε_o= 0.02*

Figure 4.8: *Wake flow field for the NACA0015 wing using Q-criterion (Q=0.8) obtained with different VC models.*

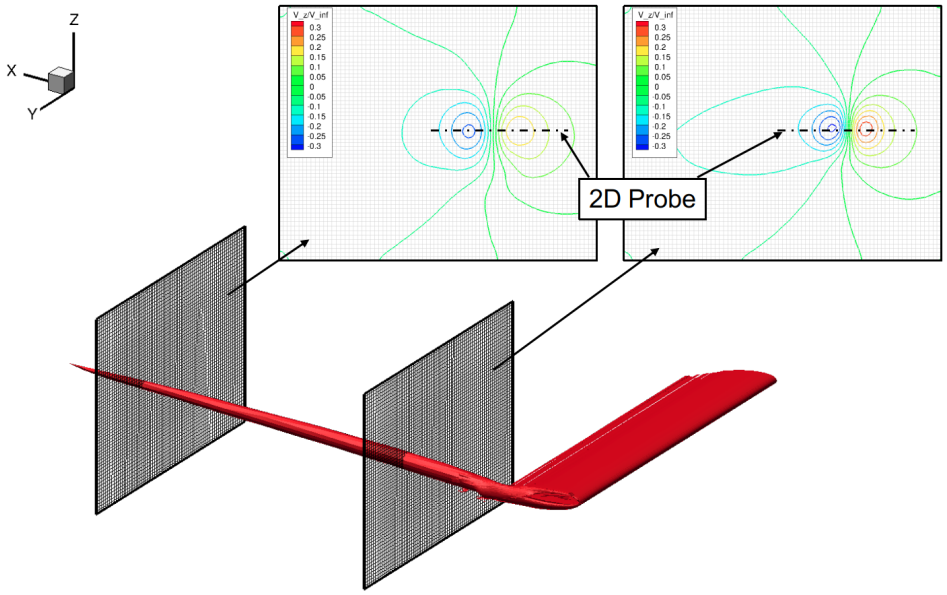

Figure 4.9: *Swirl velocity profile (z-velocity data normalized by freestream) is predicted at two dimensional locations by extracting a span-wise line, which passes through the vortex core.*

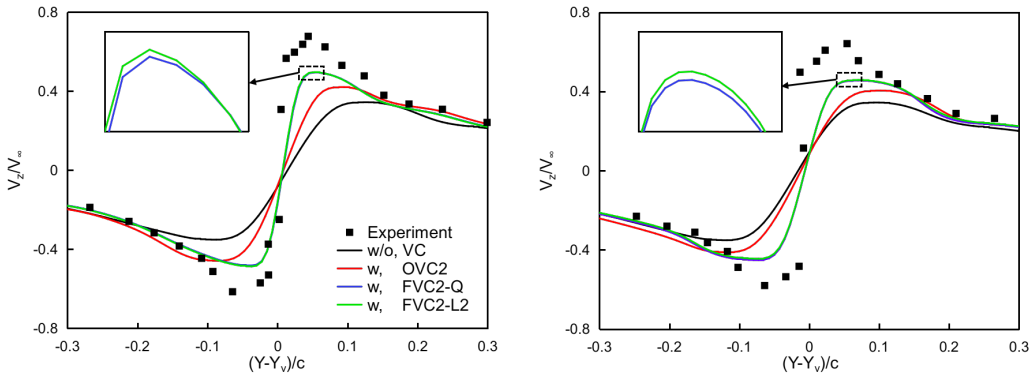

(a) *At two chords from trailing edge* **(b)** *At four chords from trailing edge*

Figure 4.10: *A comparison of normalized z-velocity at two and four chords downstream for the case with and without the VC models.*

4.3.2 Caradonna-Tung Rotor in Hovering Flight

The flow around the Caradonna-Tung rotor blades, in hover, is used to demonstrate the performance of the implemented VC models on the rotor flow. Due to the public availability of the experimental datasets, this rotor represents a benchmark to validate the VC models for hovering helicopter rotors.

The 2-bladed Caradonna-Tung model rotor has untwisted planform of 1.143 m radius. The blades are comprised of symmetric NACA0012 airfoil of 0.1905 m chord length. Experiments were carried out in the Army Aeromechanics Laboratory's hover test facility, where a large chamber with special ducting was designated to eliminate room recirculation [131]. The hover conditions considered here employ a blade collective pitch angle of $8°$, blade-tip Mach number of 0.877, and precone angle of $0.5°$.

A moving embedded grid system is designed for the present study, composed of background grid, and two identical body-fitted blade meshes. The grid system is presented in Figure 4.11. The background mesh consists of two different cylindrical grids. A coarse grid (far-field grid) is generated to represent the flow domain far from the rotor, where outer boundaries are located 4R (above), 8R (below), and 8R (radial) away from the blade hub. A finer grid (near-field grid) is created to model the flow region close to the blades. The body-fitted blade grid is modelled with a C-H topology. The wall distance of the first layer of blade surfaces is set to $1 \times 10^{-5}c$ so that the y^+ value is less than 1. A non-slip boundary condition is applied on the blade surface.

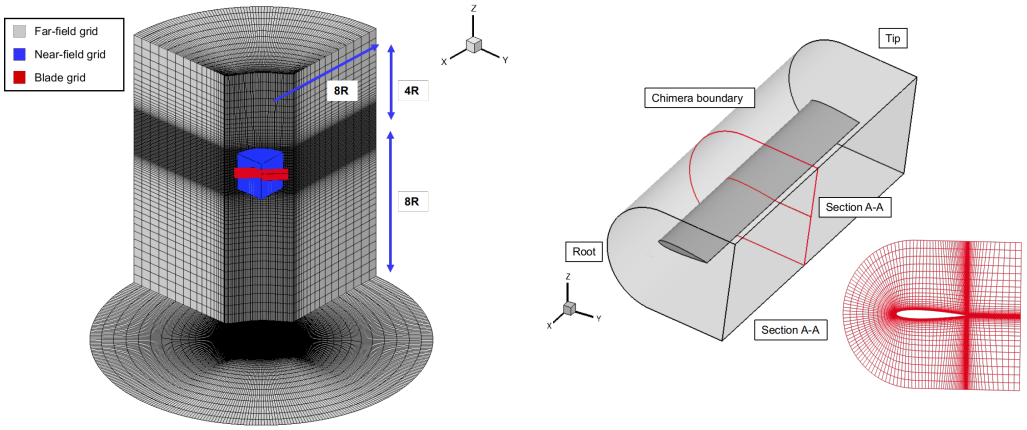

(a) *Overset grid system* **(b)** *Detailed view of blade grid*

Figure 4.11: *The computational grid of the Caradonna-Tung rotor case.*

To account for the grid sensitivity effect for the solutions around the blade, three structured blade grid, increasing the mesh size from 0.8 to 2.4 million cells, are generated to perform the grid sensitivity analysis. Furthermore, three near-field meshes are considered for the assessment of VC models on vorticity preservation and computational efficiency. The summary of the far- and near-field grids is shown in Table 4.3. The blade grid details are reported in Table 4.4

Table 4.3: *Details of the background grids (t: tangential, r: radial, z: normal, minimum spacing is outlined in terms of rotor radius R).*

Mesh	N_{tot}	N_t	N_r	N_z	Δt($\times 10^{-3}$)	Δr($\times 10^{-3}$)	Δz($\times 10^{-3}$)
Far-field	1805400	360	20	118	31.1	30.6	31.1
Near-field(NG1)	3402900	360	77	95	0.14	13.1	13.1
Near-field(NG2)	4454460	360	87	115	0.14	10.5	10.5
Near-field(NG3)	5452200	360	94	130	0.14	8.7	8.7

Table 4.4: *Details of the blade grid (ξ: chord-wise, ζ: span-wise, η: normal, minimum spacing is outlined in terms of blade chord c)*

Mesh	N_{tot}	N_ξ	N_ζ	N_η	$\Delta\xi(\times 10^{-3})$	$\Delta\zeta(\times 10^{-3})$	$\Delta\eta(\times 10^{-3})$
Coarse	872500	190	100	45	1.6	0.05	0.01
Medium	1722500	305	100	50	1.6	0.05	0.01
Fine	2409066	305	138	50	1.6	0.05	0.01

4.3.2.1 Grid Sensitivity Study

A grid sensitivity study is carried out first to obtain the grid convergence solutions when no VC models are enabled. Computations are performed by employing the NG1 near-field mesh and three different blade meshes with coarse, medium and fine grid densities. Figure 4.12 shows the comparison of the calculated C_P distributions with experimental data [131] at three radial positions, r/R = 0.5, 0.68, 0.80, 0.89 and 0.96. At inboard station (r/R = 0.5 and 0.68), the sectional C_p distributions are almost identical for three grid density cases. At three outboard positions (r/R = 0.80, 0.89 and 0.96), the grid resolution effect becomes more notable on the prediction of transonic shock wave. A more smeared shock is observed for the coarsest grid case. However, the results of the medium and fine grid cases are in good agreement with the measurements with negligible difference between them. Therefore, it is reasonable to believe that sufficiently converged results are obtained with the medium blade grid, which can be used for further study.

4.3.2.2 Effect on Computational Stability

In terms of the computational stability of the implemented VC models, Figure 4.13 shows the flow solution residuals of the Caradonna-Tung rotor blade (NG1 near-field mesh for all the test approaches) under seven confinement parameter values, where ε = 0.0 stands for the solution without any VC models. All flow solutions were simulated by solving the RANS equations, coupled with the Spalart-Allmaras turbulence model. The governing equations were integrated with the implicit dual-time stepping method of ROSITA, using a pseudo-time CFL number equal to 3.0. Typically, 4000 iterations are required to reduce the residuals by four levels of flow solutions in most cases. However, it is observed that, for the OVC2 solution with ε = 0.02 , some robustness problems occur after about 500 pseudo-time steps; therefore values greater than ε = 0.02 were not tested for the OVC2 model. The result for the FVC2-Q model with ε = 0.05 starts diverging after 6000 pseudo-time steps. The FVC2-L2 model is able to maintain the stability of the entire calculation process until ε = 0.07. This supports the idea that with

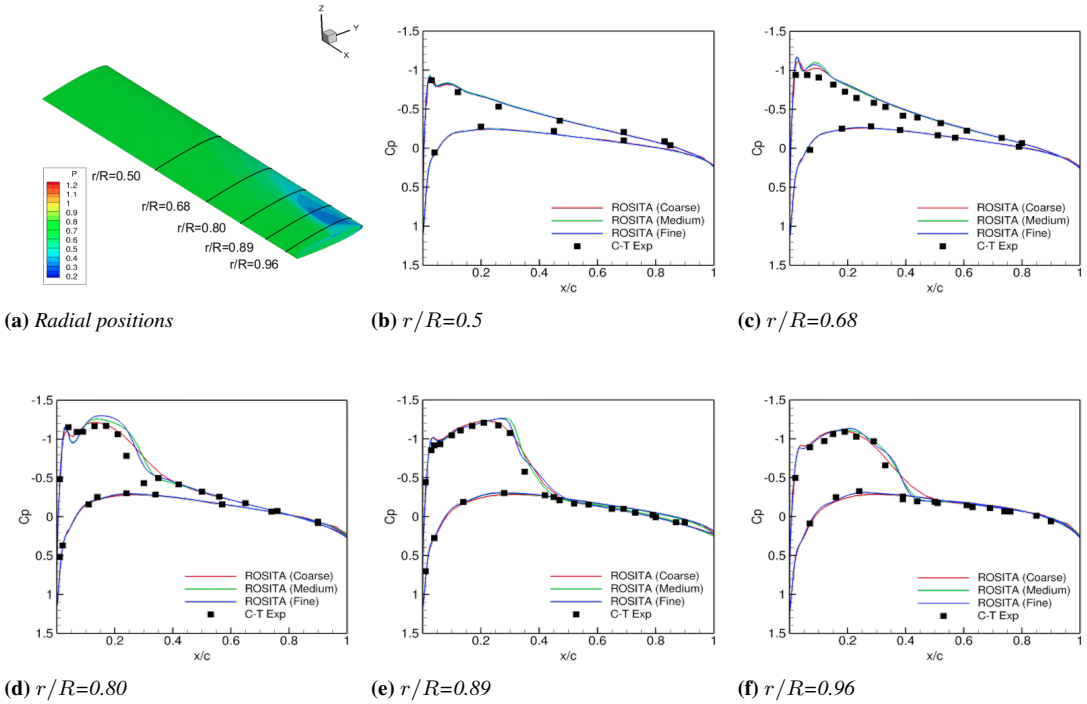

(a) *Radial positions* **(b)** r/R=0.5 **(c)** r/R=0.68

(d) r/R=0.80 **(e)** r/R=0.89 **(f)** r/R=0.96

Figure 4.12: *Blade surface pressure distribution at specified cross-section positions. Predictions compared against measurements.*

the introduction of vortex feature-detection method, the robustness of the standard VC2 model is maintained with higher confinement parameters, especially for the FVC2-L2 model. Therefore, the reference confinement parameter value can be roughly obtained: ε_o = 0.01 for OVC2 model, ε_o = 0.04 for FVC2-Q model, and ε_o = 0.06 for FVC2-L2 model.

4.3.2.3 Influence on Aerodynamic Loads Prediction

In this part, the medium blade mesh and NG1 near-field mesh are employed for all tested approaches. Furthermore, the ε parameter is set at its reference value for each VC model. The sectional lift coefficient C_L are employed to investigate the effect of different VC models on aerodynamic loads prediction. An averaging process is activated over 500 pseudo-time steps at the end of each simulation. Figure 4.14 shows the variation of sectional C_L along the rotor radial direction. It is observed that the FVC2-L2 model case provides notable improvements, although over-predictions are obtained for all calculations. As previously stated, this improved result could be attributed to the use of the vortex feature detection methods, which avoid the over-confinement in the boundary layer.

4.3.2.4 Effect on Vorticity Preservation

As shown in Figure 4.15, the contour plots of vorticity magnitude are extracted from five chordwise sections (y/c = 0.5, 0.25, 0.45, 0.65, 0.85). The development of the tip vortex system over the Caradonna-Tung rotor blade is presented in Figure 4.16, where

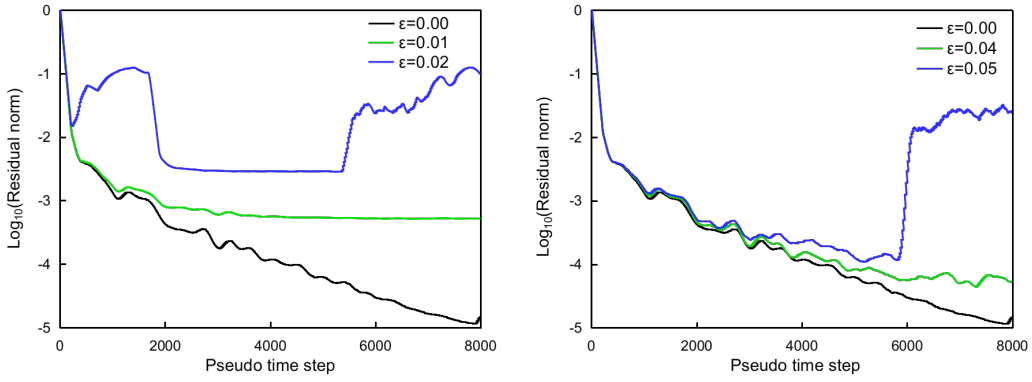

(a) *w, OVC2 model*

(b) *w, FVC2-Q model*

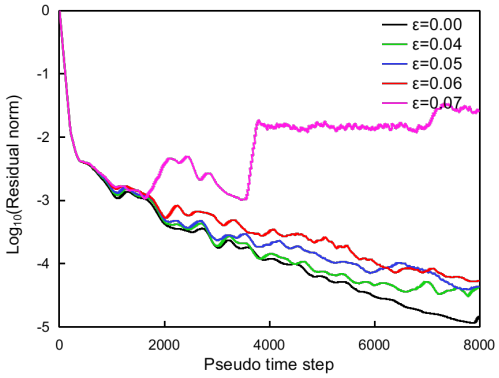

(c) *w, FVC2-L2 model*

Figure 4.13: *Residual flow solution history of the Caradonna-Tung rotor case.*

the results with three different VC models are compared against the non-VC model solution. From the section $y = 0.25c$, it can be seen that the application of VC models has improved the coherent vortex structures. However, the improvements in the vortex formation region are not so evident.

Visualization of the Caradonna-Tung rotor wake using the iso-surface of Q-criteria (Q = 0.15) is shown in Figure 4.17, in which the blade-tip vortex sections at five selected wake ages are extracted to better assess the downstream vorticity preservation capability of employed VC models. It should be reminded that, the VC models are employed with the reference ε values; the non-VC model is used for comparison on the same near-field mesh. It is observed that the helical vortex filaments shed from the blade-tip are better preserved with the use of the implemented VC models when compared with the solution of non-VC model case. Furthermore, the capacities of the vortex feature-based VC models to preserve downstream vorticity are well demonstrated through the comparison with the solution of the OVC2 model. Quantitatively, Figure 4.18 illustrated the vorticity magnitude of blade-tip vortex core as function of the wake age in degrees for the solutions with and without VC models on NG1 mesh. Although a dissipation of vorticity at the vortex core is observed along with the wake ages, the simulations performed with the VC models result in an improved vorticity preservation if compared with the solution without VC model. In detail, at wake ages of $\pi/6$, an improvement

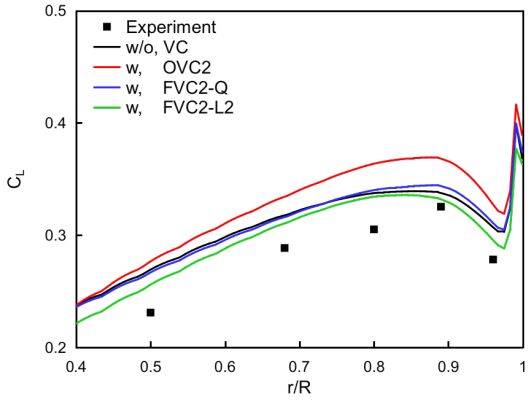

Figure 4.14: *Effect of different VC models on blade span loading.*

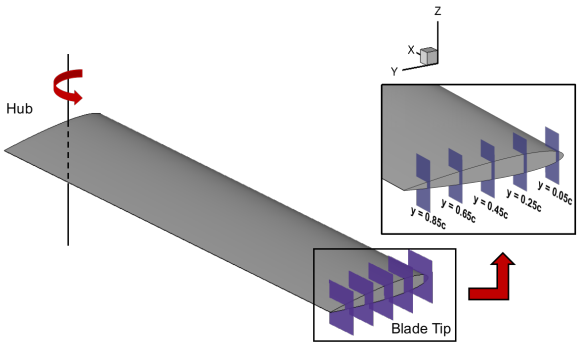

Figure 4.15: *Vorticity contour plots at plotted at five chordwise stations.*

of vorticity by 16%, 20.8% and 25.1%, with respect to the non-VC case, is reported for the OVC2 model, FVC2-Q model and FVC2-L2 model, respectively. As the wake age increases, a more notable discrepancy of vorticity is witnessed for the solutions of three VC models. After $5\pi/3$, the improvement of the core vorticity shown by the FVC2-L2 model is about twice as large as found for the FVC2-Q model if compared with the OVC2 model. These studies confirm that the introduction of vortex feature-detection methods can help to effectively enhance the capability of vorticity preservation of the OVC2 model. Moreover, the λ_2-based VC2 model shows lower dissipation than the Q-based VC2 model.

The wake structures of the non-VC model case performed over two finer near-field meshes (NG2 and NG3) are also shown in Figure 4.19. It is observed that, with the use of finer near-field meshes, the blade-tip vortex of the case without VC model can be traced up to about $11\pi/6$ and 2π, respectively. However, the coherent structures are better preserved up to further distance by introducing the FVC2-Q and FVC2-L2 model on NG1 mesh, as previously illustrated in Figure 4.17c and 4.17d.

This conclusion is further confirmed looking at the variations of the blade-tip vortex strength in Figure 4.20. The vortex strength captured by the two finer near-field meshes without VC model has a faster decay rate than those of the FVC2-Q and FVC2-L2 solutions. At the onset phase ($\psi = \pi/6$), the core vorticity of the non-VC model with NG2 and NG3 meshes is greater than the results of the vortex feature-based VC2 mod-

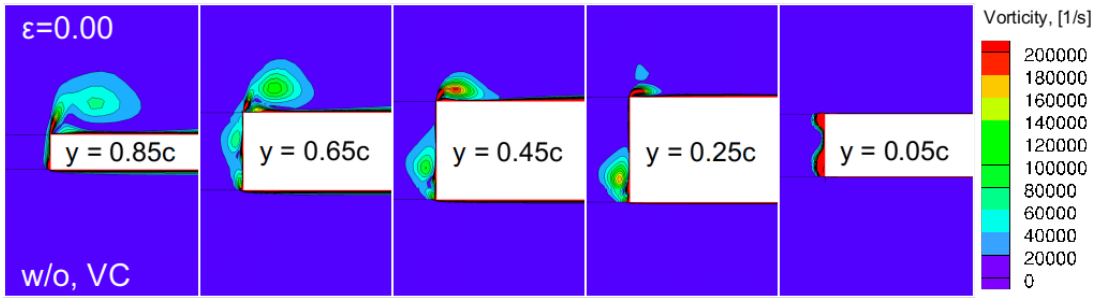

(a) *w/o, VC model, ε = 0.0*

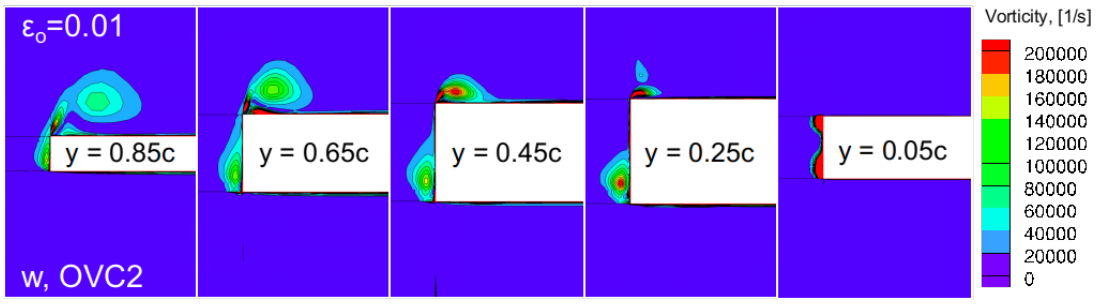

(b) *w, OVC2 model, ε_o = 0.01*

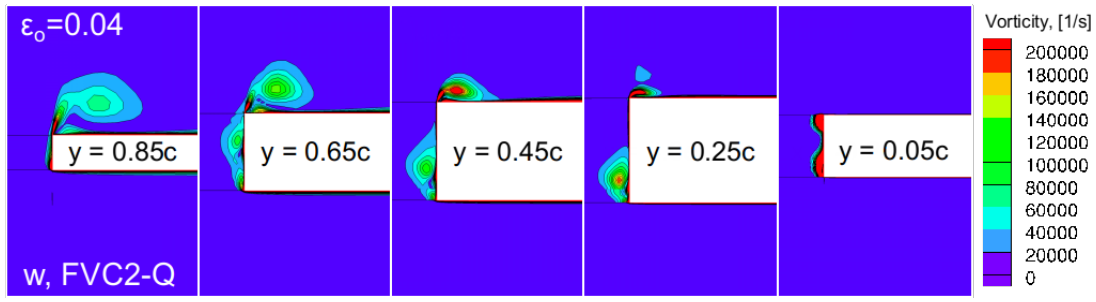

(c) *w, FVC2-Q model, ε_o = 0.04*

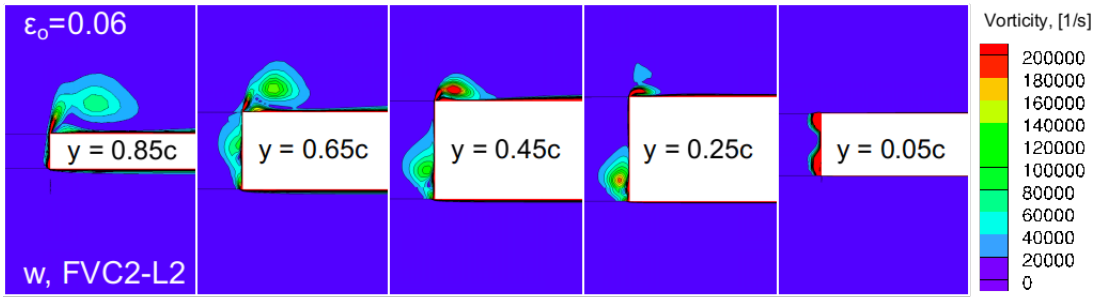

(d) *w, FVC2-L2 model, ε_o= 0.06*

Figure 4.16: *Formation process of blade-tip vortex.*

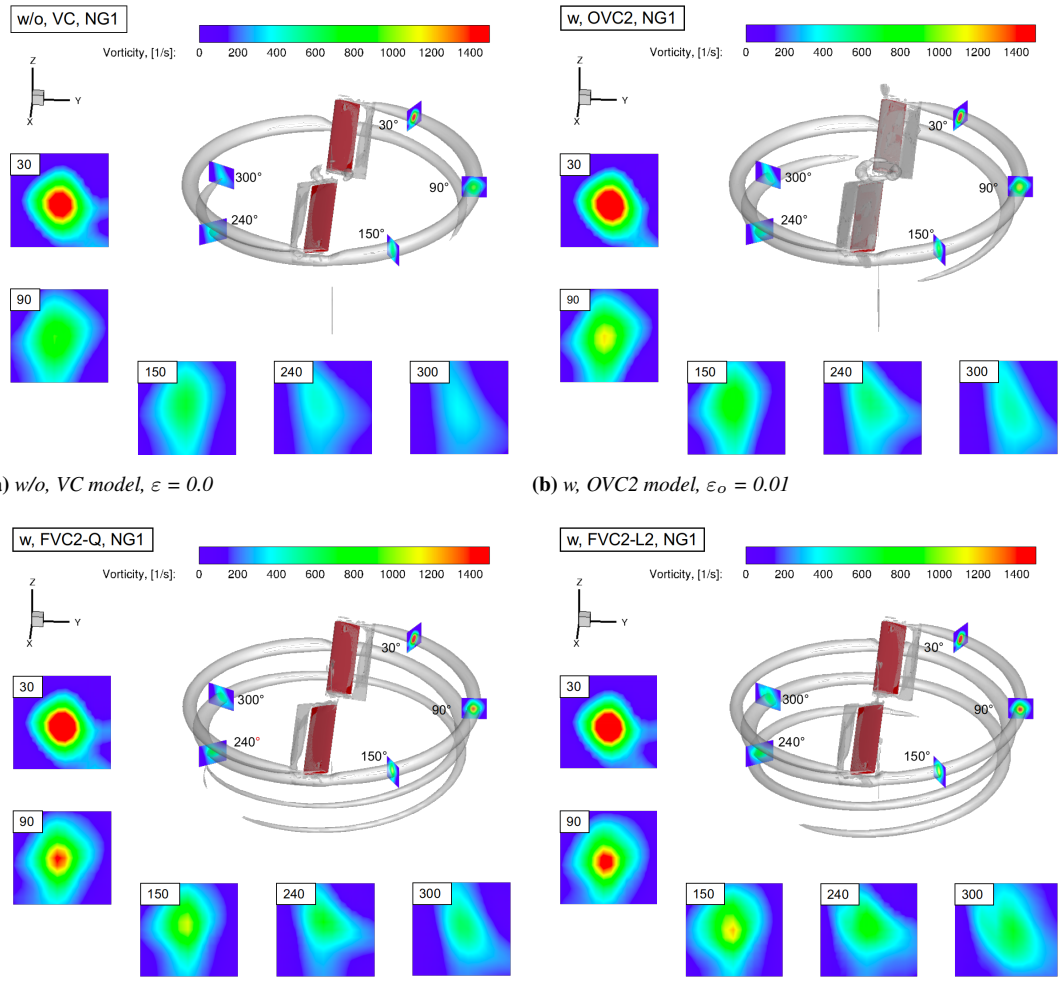

(a) *w/o, VC model, ε = 0.0*

(b) *w, OVC2 model, ε_o = 0.01*

(c) *w, FVC2-Q model, ε_o = 0.04*

(d) *w, FVC2-L2 model, ε_o= 0.06*

Figure 4.17: *Wake flow field for the Caradonna-Tung rotor using Q-criterion (Q = 0.15) obtained with different VC models.*

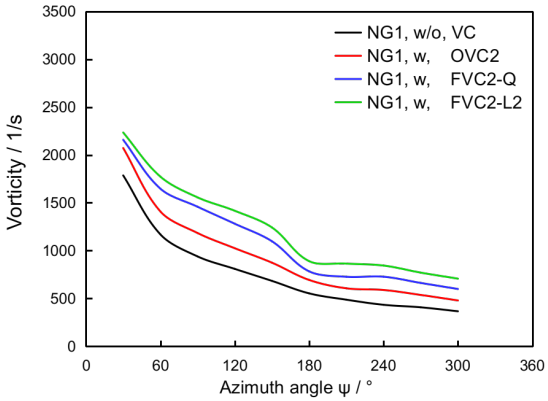

Figure 4.18: *Vorticity of the blade-tip vortex core, obtained with and without VC models on the NG1 mesh.*

els with NG1 mesh. At the wake age of $\psi = \pi/3$, the core vorticity value of the NG2 case turns to be lower than those of the NG1 cases. When it is close to the wake age of $\psi = 2\pi/3$, the calculated vorticity at the vortex core center for the NG3 case starts to become smaller than the vorticity value of the NG1 cases. In other words, it indicates that the vortex feature-based VC2 models express an excellent vorticity preservation capability.

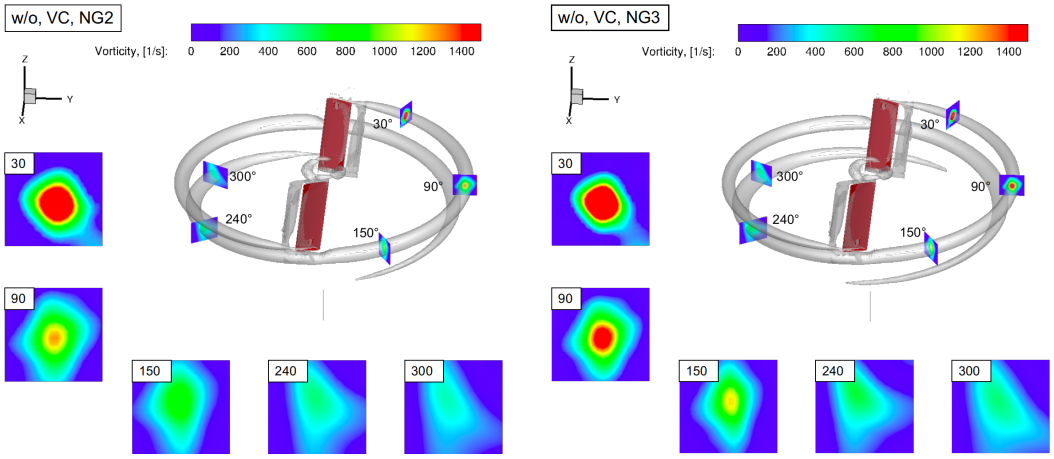

(a) *w/o, VC model, NG2 mesh* **(b)** *w/o, VC model, NG3 mesh*

Figure 4.19: *Wake flow field for the Caradonna-Tung rotor using Q-criterion (Q = 0.15).*

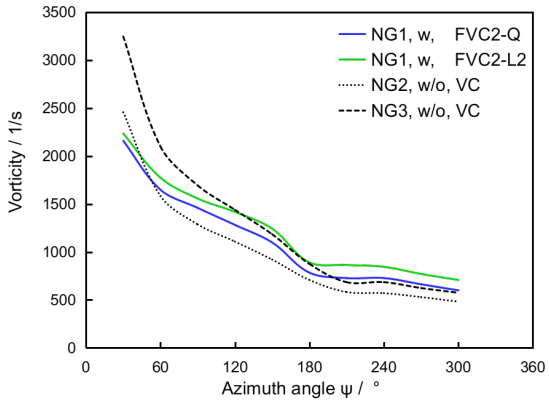

Figure 4.20: *Vorticity of the blade-tip vortex core, obtained with vortex feature-based VC models over NG1 mesh as well as the non-VC model over NG2 and NG3 meshes.*

4.3.2.5 Effect on Computational Efficiency

Table 4.5 reports the computational time cost for the Caradonna-Tung rotor blade simulations with the FVC2-Q and FVC2-L2 models on the NG1 mesh as well as the non-VC model on the NG1, NG2, and NG3 meshes. Solutions were computed on 64 cores of the high-performance cluster Galileo100 of CINECA, comprised of Intel CascadeLake 8260 2.4 GHz processors, nodes interconnected by a Mellanox Infiniband HDR100 high-performance network. As can be observed, cases with the vortex feature-based

VC2 models on the coarse near-field mesh present a much higher computational efficiency than the non-VC model case performed on the finer near-field meshes.

Table 4.5: *CPU run-time for the Caradonna-Tung rotor simulations.*

Case	Near-field mesh	VC model	Mesh number ($\times 10^6$)	simulation time (work units/iteration)
1		—		1.0
2		FVC2-Q	8.65	1.02 (2%)
3		FVC2-L2		1.04 (4%)
4	NG2	—	9.70	1.21 (21%)
5	NG3	—	10.70	1.48 (48%)

4.3.3 HART-II Rotor in Descending Flight

This work simulates the HART-II rotor in BL configuration using the FVC2-L2 model to investigate the influence of vorticity confinement in BVI effect capturing due to its better performance in computational stability and vorticity preservation, as stated in the previous sections. The same computational setup used in section 3.2.3, including the medium grid system, trimmed angles and temporal resolution, were employed. When applying the vorticity confinement, the trimmed computation without confinement was carried out for four revolutions first, and then two more revolutions with the FVC2-L2 models were performed.

The determination of ε_o in steady simulations is impacted by monitoring the residual magnitude of the flow variables, but in unsteady flows, it is a more complex issue. It is not sufficient to use the same methodologies to define the ε_o in unsteady flows as in steady simulations. For numerical solution of flows, vorticity is generated not only by physical reasons but also by artificial viscosity [132]. Applying large confinement values to artificial vorticity regions can lead to non-physical, spurious vortical structures. Therefore, the determination of ε_o should also take into consideration the reasonableness of the flow vortical structure. In this test example, the reference confinement parameter can be roughly determined as ε_o = 0.04 after several trial and error procedures.

4.3.3.1 Influence on Aerodynamic Loads Prediction

The C_nM^2 variations at 87% rotor radius over one revolution are plotted in Figure 4.21 where the results predicted with and without VC models are compared to the measurements [122]. Analyzing the azimuthal ranges affected by the FVC2-L2 model, a closer matching between the computed C_nM^2 variations with and without confinement may be found in the region of $120^\circ < \Psi < 240^\circ$, and a notable improvement in the prediction of load oscillations due to BVI is achieved at the advancing ($0^\circ < \Psi < 120^\circ$) and retreating ($240^\circ < \Psi < 360^\circ$) blade side for the FVC2-L2 solution when compared to the solution without confinement, although the high-frequency BVI fluctuations are still not adequately captured.

Figure 4.22 presents the low- and high-frequency components of the C_nM^2 distributions at 87% rotor radius decomposed by the low- and high-pass filters, respectively.

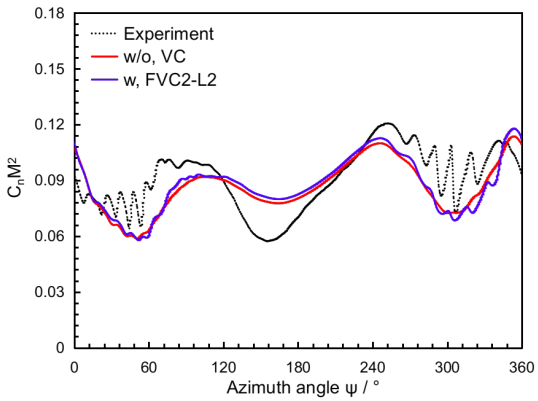

Figure 4.21: *Comparison of C_nM^2 variations with experiment for results with and without VC models.*

The low frequency of C_nM^2 mainly represents the effect of aerodynamic modeling induced by the blade motion, whereas the high frequency of C_nM^2 is closely related to the BVI airloads. Therefore, the low-frequency content could be used to examine the correctness of aerodynamic modeling effects due to the blade movement. The high-frequency component could be applied to assess the adequacy of the VC model to predict the BVI-related phenomenon. From Figure 4.22a, the low-frequency content of C_nM^2 shows a negligible change between the non-VC and FVC2-L2 results. In contrast, an evident improvement of amplitude and phase of the C_nM^2 fluctuations is observed on the retreating side for the FVC2-L2 results compared to the solution without VC models in Figure 4.22b. Regarding the advancing side, the improvements of the C_nM^2 oscillations in the FVC2-L2 computation are relatively low compared to those in the non-VC solution. The possible reason is that the vortices interacting on the advancing blade side dissipate faster than those on the retreating side due to the wake age being older than that on the retreating side. Although the full amplitude of the high-frequency peaks is not reached, the simulation results with the FVC2-L2 model are encouraging and clearly show the potential of the FVC2-L2 model in capturing the BVI phenomenon.

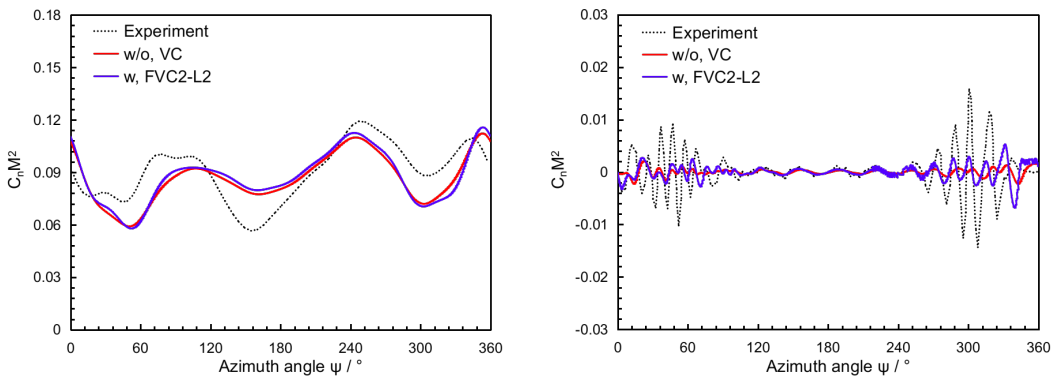

(a) *Low-frequency C_nM^2 component ($< 10/rev$)*

(b) *High-frequency C_nM^2 component ($> 10/rev$)*

Figure 4.22: *Frequency filtered C_nM^2 distributions at r/R = 0.87; VC model effects.*

The ability of the presented VC model in BVI capturing could also be interpreted as the difference of the normal force $C_n M^2$ between the FVC2-L2 results and the non-VC results on the rotor disk, as shown in Figure 4.23b. From this plot, the predicted BVI effects can be readily found in the first and fourth quadrants of the rotor disk and the positions are correlated well with the analytical solutions (Figure 4.23a).

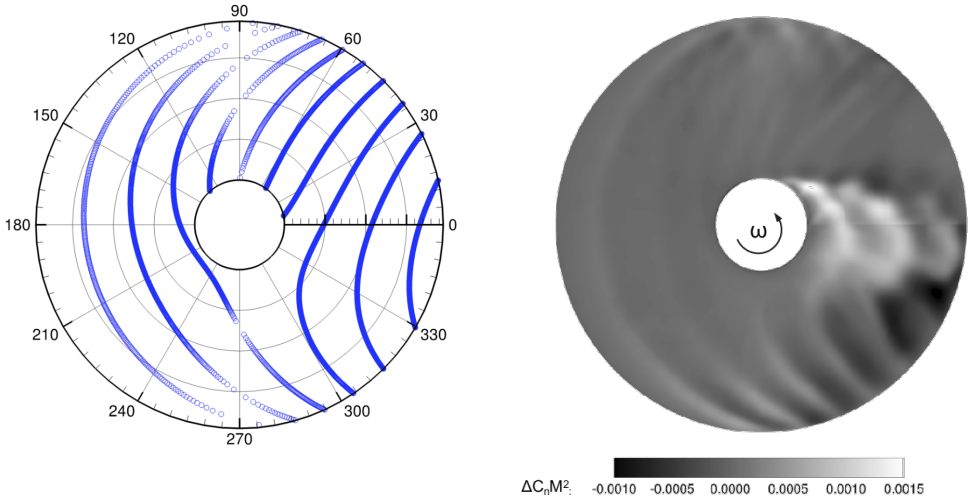

(a) *Analytical BVI positions on the rotor disk*

(b) $\Delta C_n M^2$ *distribution on the rotor disk*

Figure 4.23: *Locations of BVI events on the rotor disk for the HART-II rotor.*

4.3.3.2 Effect on Vorticity Preservation

Figure 4.24 shows the instantaneous 3D vortex system of the HART-II rotor BL case by using the Q-criterion (Q=0.03). These images qualitatively illustrate the effectiveness of the present VC model. It is clear that a lower dissipation vortical structure with coherent characters over a large number of wake spirals in all four quadrants of the rotor disk is observed for the solution with the FVC2-L2 model. This represents an important feature for accurately predicting the BVI phenomenon. In addition, Figure 4.25 presents the detailed view of the vorticity contour at three streamwise slices (x/R=0.5, 1 and 2) of blade 1 ($\psi = 0$). Solution with the FVC2-L2 model shows more concentrated vorticity at two side tip vortex pairs (A and B in Figure 4.25) than the non-VC results, which highlight the capability of the employed VC model in preserving the rotor vortical flow structures.

4.4 Acoustic Aanlysis

In the numerical simulation of helicopter rotor flow, the acoustic prediction highly depends on the accurate capturing of rotor vortical flows. This section concerns the application of the vortex feature-based VC2 (FVC2-L2) model on the prediction of helicopter rotor aeroacoustics. Two practical rotor flows are considered. The first case is the non-lifting UH-1H hovering rotor, where no tip vortices are shed from the blade tip. The second case employs the AH-1/OLS rotor in low-speed descending flight where the BVI phenomena are dominated.

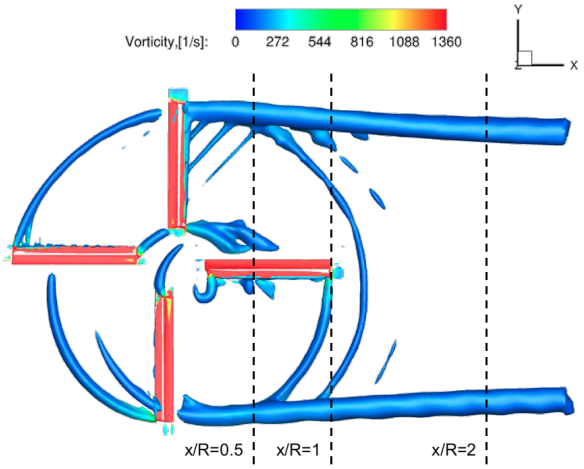

(a) *w/o, VC model*

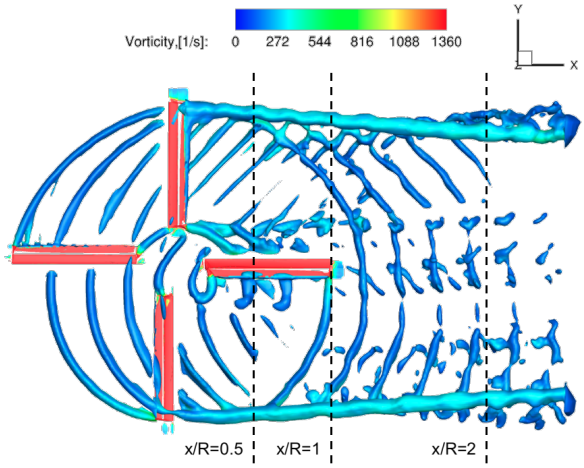

(b) *w, FVC2-L2 model, ε = 0.04*

Figure 4.24: *Q-visualization of HART-II rotor wake system, Q = 0.03.*

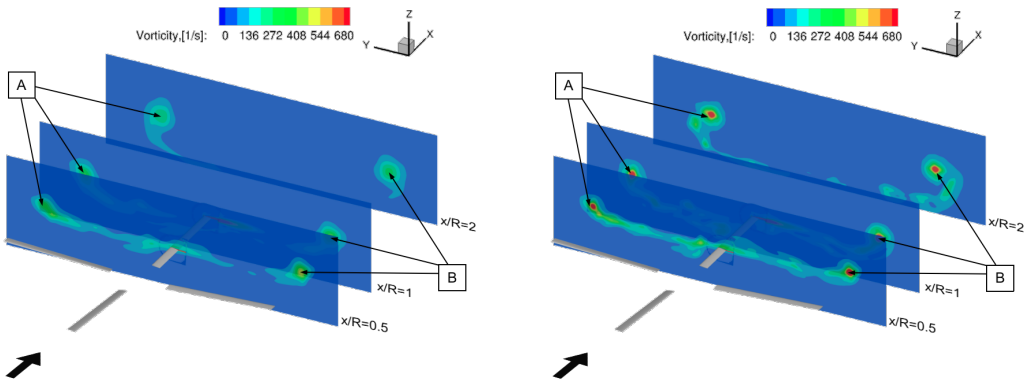

(a) *w/o, VC model*

(b) *w, FVC2-L2 model, ε = 0.04*

Figure 4.25: *Vorticity contours at three streamwise planes (x/R = 0.5, 1, and 2) of the blade 1 ($\Psi = 0°$).*

4.4.1 UH-1H Rotor in Hovering Flight

This section deals with the effect of the FVC2-L2 model on noise prediction for a helicopter rotor operated at non-lifting condition (i.e. $\theta_0 = 0°$), where no tip vortices are shed from the blade tip. The same non-lifting UH-1H hovering rotor case as used in the section 3.3.1 was applied to analyze the effect of the vorticity confinement method on acoustic prediction. Two test conditions with the blade tip Mach number M_T equal to 0.85 and 0.95 were considered. The same medium-resolution grids were used to obtain the input data for noise prediction instead of repeating the grid dependency analysis since it has been carried out in section 3.3.1.

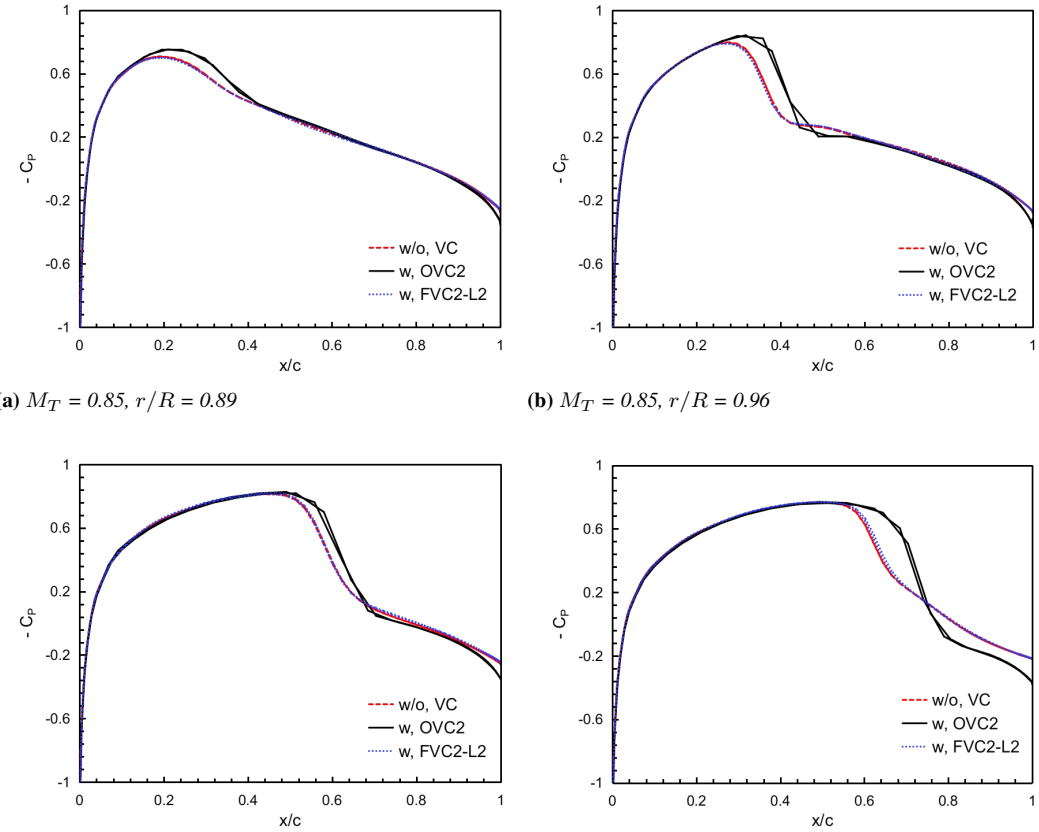

(a) M_T = 0.85, r/R = 0.89 **(b)** M_T = 0.85, r/R = 0.96

(c) M_T = 0.95, r/R = 0.89 **(d)** M_T = 0.95, r/R = 0.96

Figure 4.26: *Pressure coefficient comparisons on different blade cross-sections for the UH-1H rotor.*

Figure 4.26 shows the blade chordwise C_P profiles at two sectional positions (r/R = 0.89 and 0.96) computed by using the FVC2-L2 model. The results of the non-VC model and the standard VC2 (OVC2) model are undertaken for comparison. We assumed that ε_o = 0.01 and 0.06 are applied for the case with the OVC2 model and the FVC2-L2 model, respectively. It is observed that there are significant differences between the results simulated by the OVC2 model and the non-VC model on the C_P profiles due to the over-confinement inside the boundary layer. In contrast, the FVC2-L2 simulation with the λ_2-criterion introduced inside the boundary layer gives almost identical C_P distributions compared to the non-VC results. It implies that the robustness of the ROSITA solver on rotor blade aerodynamics prediction is maintained when the

FVC2-L2 model is adopted.

The predicted acoustic time-domain signals at M_T = 0.85 and 0.95 are compared with the measured data [125] in Figure 4.27, where the acoustic data predicted by the OVC2 simulation are not taken into account, due to its notable discrepancies in the C_P profiles compared to the non-VC and FVC2-L2 solutions. Since M_T, for two test conditions is operated in a transonic regime, the noise predictions are conducted by using the Emission-Surface formulation of the PS-FWH equation, which has a much less restrictive nature in the Doppler factor, instead of using the Retarded-Time formulation. It is shown that the predicted results are in good agreement with the experimental data in terms of the peak values and wave shapes. In addition, simulations using the FVC2-L2 model predict the negative and positive peaks of noise signals more precisely than in the non-VC model case. It is demonstrated that the FVC2-L2 model is able to improve the accuracy of the acoustic prediction to a certain extent, even if no tip vortices are shed from the blade tip.

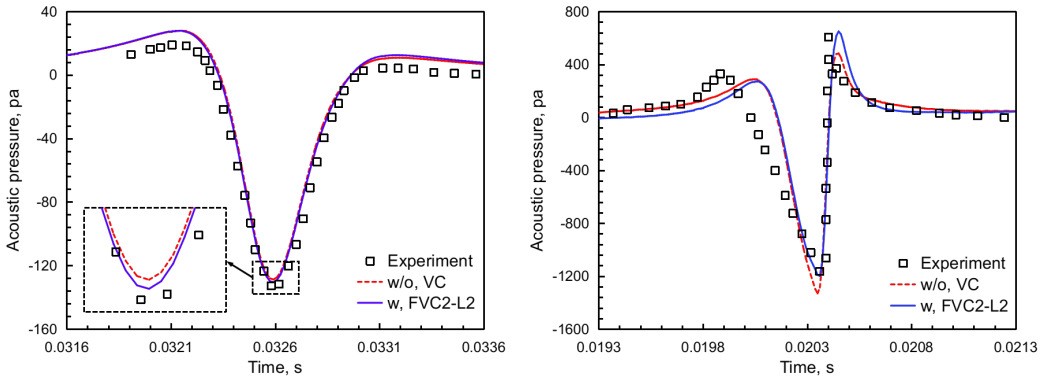

(a) M_T = 0.85 **(b)** M_T = 0.95

Figure 4.27: *Predicted and experimental acoustic pressure time history obtained from the non-VC and FVC2-L2 models for the UH-1H rotor at M_T = 0.85 and 0.95.*

4.4.2 AH-1/OLS Rotor in Forwarding Flight

This work simulates the AH-1/OLS rotor in low-speed descending flight (test point 10014 [120]) using the FVC2-L2 model with $\varepsilon_o = 0.04$ to investigate the influence of the vorticity confinement on noise prediction. The same computational setup, including the grid system, trimmed angles, and temporal resolution, used in section 3.3.2 were chosen to obtain the input data for noise prediction. All six microphone positions reported in Table 3.18 were considered.

The blade chordwise C_p distributions over the radial position of r/R = 0.955 at $0°$, $90°$, $135°$, and $180°$ azimuths are plotted in Figure 4.28, where the results with the non-VC model and the FVC2-L2 model are compared against the test data [121]. As expected, the C_p profiles computed with and without VC models show similar behaviors indicating the effectiveness of the CFD solver and no evident effects on the aerodynamic prediction with the introduction of the FVC2-L2 model.

The variation of $C_n M^2$ at two rotor radius stations (r/R=0.75 and 0.91) over one revolution are given in Figure 4.29. An evident improvement compared to the non-VC

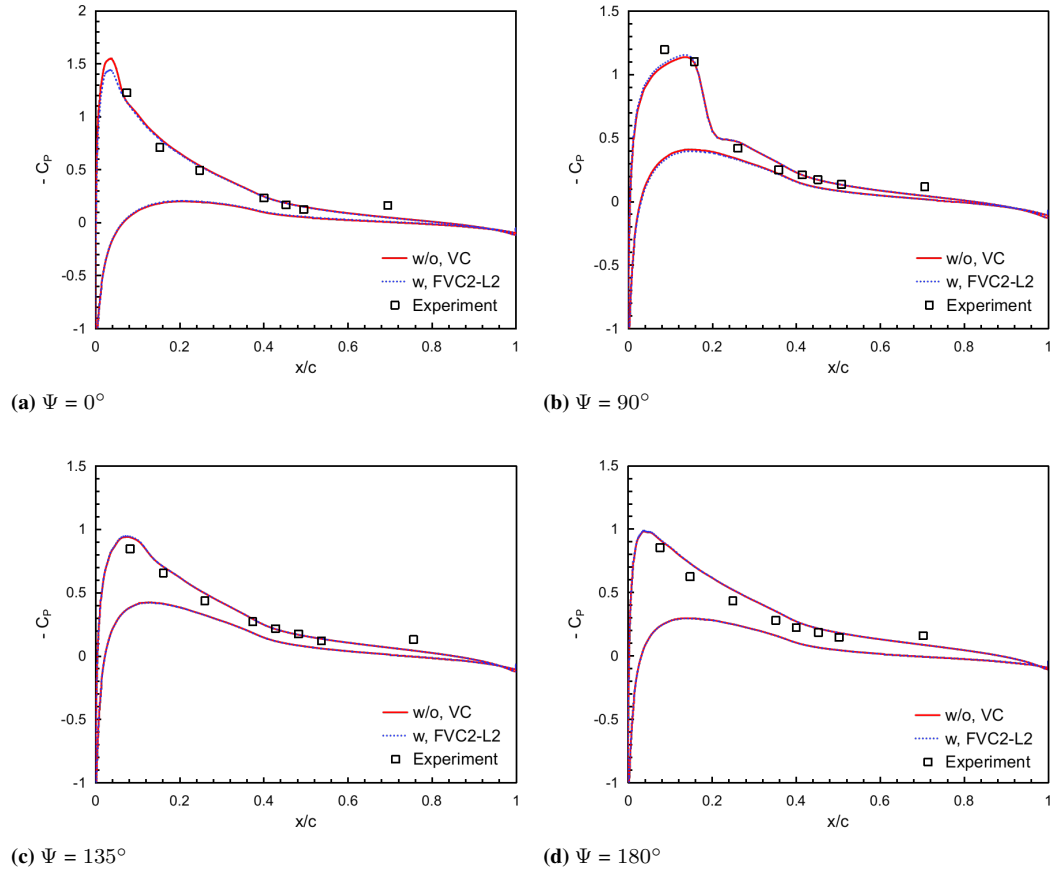

(a) $\Psi = 0°$ **(b)** $\Psi = 90°$

(c) $\Psi = 135°$ **(d)** $\Psi = 180°$

Figure 4.28: *Pressure coefficient comparisons on different blade cross-section at r/R = 0.955 for various azimuth angles.*

results is achieved using the FVC2-L2 model. For the FVC2-L2 model computation, a clear amplification of the BVI fluctuations is observed on the retreating blade side. some BVI airloads are also captured on the advancing side, although it features a small interaction. The difference of the normal force $C_n M^2$ between the solution of the FVC2-L2 model and the non-VC model is plotted on the rotor disk to visualize the BVI effects, as shown in Figure 4.30b. With this plotting style, the improvements of the BVI airloads prediction for the FVC2-L2 solution can readily be identified in four quadrants of the rotor disk. In addition, the BVI positions are correlated well with the analytical positions (Figure 4.30a).

The instantaneous rotor wake system of the AH-1/OLS rotor, captured from the non-VC and the FVC2-L2 model cases, is depicted using the Q-criterion (Q=0.02) in Figure 4.31. As can be seen, the non-VC model and the FVC2-L2 cases express substantial differences in the wake resolution. The result with the FVC2-L2 model provides a more sophisticated tip vortex structure than those without VC models. For example, the case with vorticity confinement could preserve the trajectory of the wake more than two radii downstream, but the non-VC case only maintains the wake system to less than one and a half radii downstream. Furthermore, the same postprocessing as used in Figure 4.25 can be performed using slice cuts at three downstream positions (x/R = 0.5, 1 and 2)

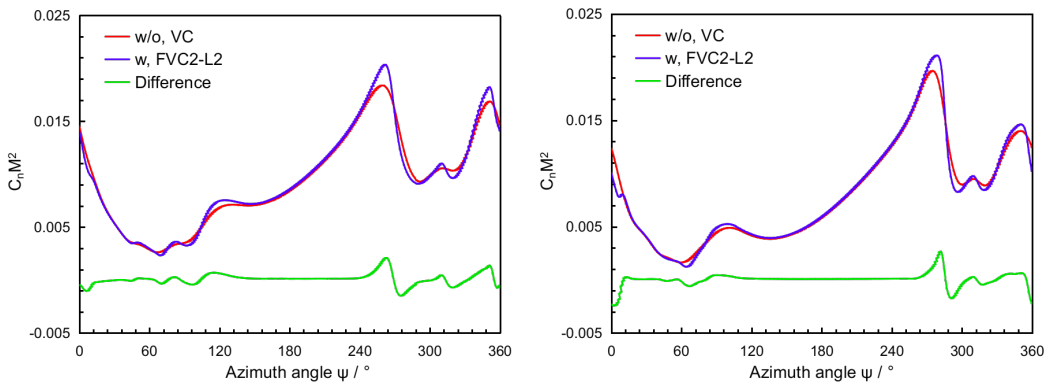

(a) $r/R = 0.75$ **(b)** $r/R = 0.91$

Figure 4.29: $C_n M^2$ *prediction by the case with and without VC models.*

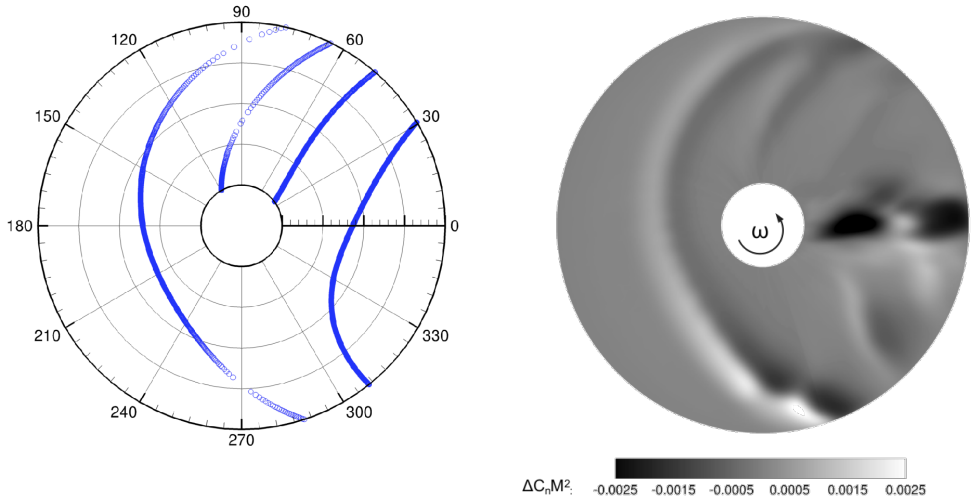

(a) *Analytical BVI positions on the rotor disk* **(b)** $\Delta C_n M^2$ *distribution on the rotor disk*

Figure 4.30: *Locations of BVI events on the rotor disk for AH-1/OLS rotor.*

to illustrate the difference of vorticity magnitude in the preserved tip vortex centers for the non-VC and the FVC2-L2 solutions, as shown in Figure 4.32. The FVC2-L2 case presents a higher extreme of vorticity magnitude than the case without confinement. These results reveal the low dissipation features and high rotor wake resolution of the FVC2-L2 model, demonstrating its benefit for capturing the rotor vortical flows and analyzing the BVI phenomena.

The conservative variables in the permeable data surface $S_{cs} = (1.0, 0.5)$ were extracted from the computed rotor flow field as the input data for noise prediction. The acoustic signals at six microphone positions are presented in Figure 4.33, where the results predicted by the non-VC and the FVC2-L2 models are compared with measurements [120]. A significant improvement in the pulse amplitude of the noise signal is observed for the results with the FVC2-L2 model. In addition, the high-frequency fluctuation features are well resolved for all six observer positions, which means the

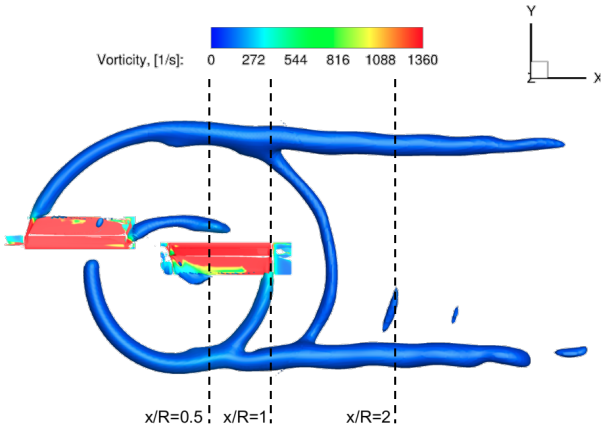

(a) *w/o, VC model*

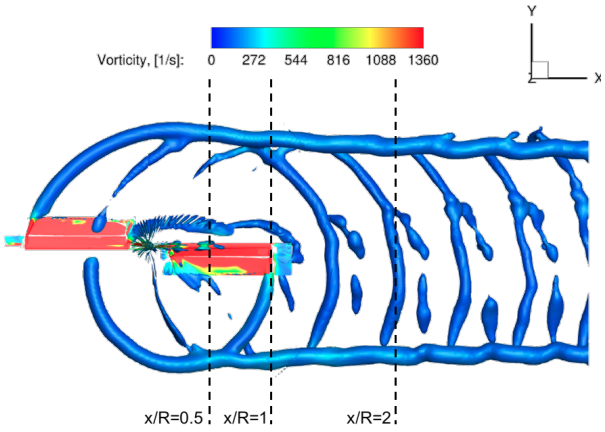

(b) *w, FVC2-L2 model,* ε_o*=0.04*

Figure 4.31: *Q-visulazation of the AH-1/OLS rotor wake system, Q = 0.02.*

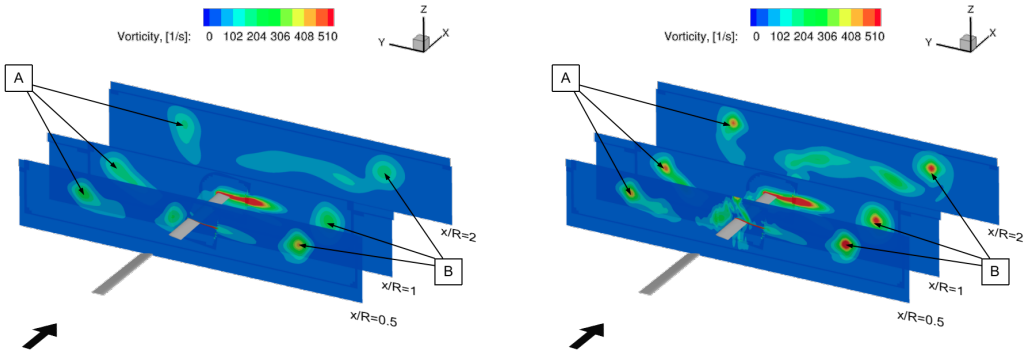

(a) *w/o, VC model*

(b) *w, FVC2-L2 model,* ε_o *= 0.04*

Figure 4.32: *Vorticity contours at three downstream slices (x/R = 0.5, 1, and 2) for the AH-1/OLS rotor.*

FVC2-L2 model is able to capture the effects of the BVI. Furthermore, by introducing the FVC2-L2 model, the predicted noise signals correlate well with the experimental

data in terms of the waveform and pulse peak pressure.

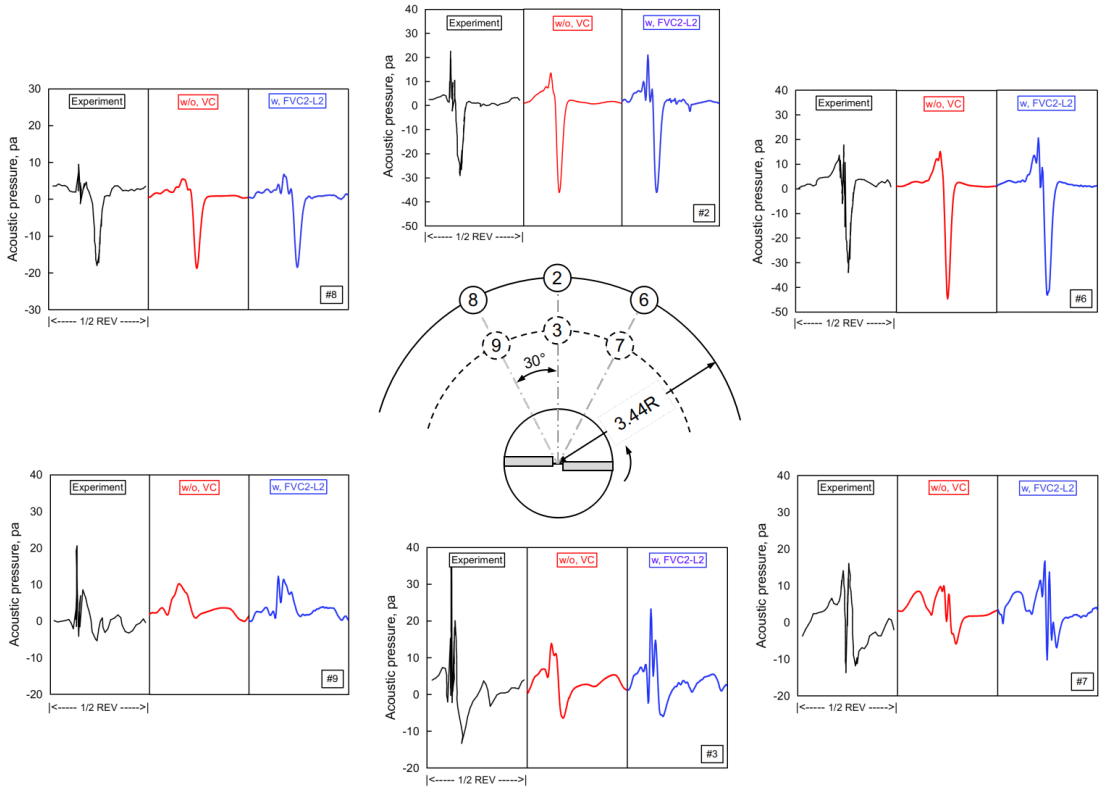

Figure 4.33: *Predicted acoustic pressure at six microphone positions for the AH-1/OLS rotor test. The plots showcase the computed acoustic pressure with non-VC and the FVC2-L2 models.*

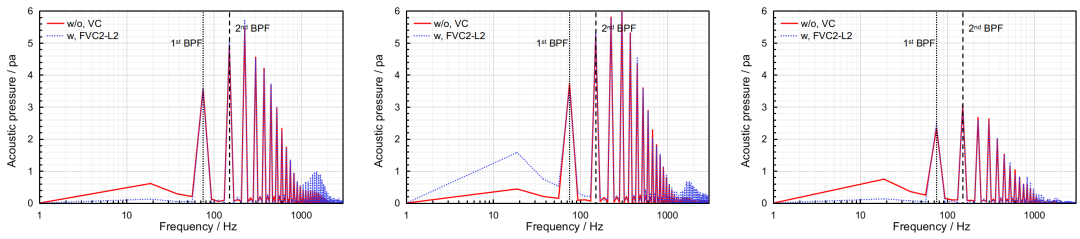

(a) *Microphone* #2 **(b)** *Microphone* #6 **(c)** *Microphone* #8

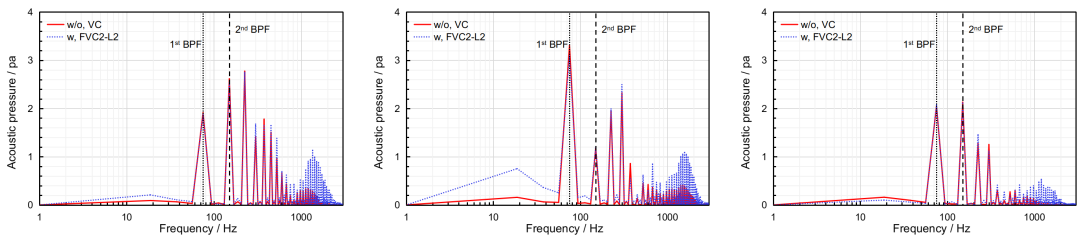

(d) *Microphone* #3 **(e)** *Microphone* #7 **(f)** *Microphone* #9

Figure 4.34: *Acoustic signals in frequency domain at six microphone positions.*

In Figure 4.34, spectral analysis with Fast Fourier Transformation (FFT) was per-

formed to understand the source contributions of the vorticity confinement on the predicted acoustic signatures. The calculated time-domain noise signals at all six microphone positions were transformed into the frequency domain. In general, high-frequency noise is related to highly unsteady sources, such as the BVI phenomenon; low-frequency noise relies on steady and periodic sources. From these plots, it is noted that the FVC2-L2 model results in an evident increase in high-harmonics noise but a negligible change in low-frequency noise compared to the non-VC case. It further confirmed that the FVC2-L2 model maintains the robustness of the aerodynamic prediction of the original CFD solver and decreases the numerical diffusion to capture the rotor vortical flows.

4.5 Summary

In this chapter, the implementation of the vortex feature-based second vorticity confinement (FVC2-Q and FVC2-L2) models was evaluated in terms of the aerodynamics and aeroacoustics. The investigation of the implemented VC2 models can be summarized as follows:

- A NACA0015 wing in steady flow and the Caradonna-Tung helicopter rotor in hovering flight were calculated to assess the performance of the FVC2-Q and FVC2-L2 models. Results were compared to the standard VC2 (OVC2) model and non-VC model solutions regarding the computational stability, aerodynamic prediction, vortex resolution, and computational efficiency. It was found that the vortex feature-based VC2 models express better performance on above aspects. In particular, the FVC2-L2 model showed a higher resolution of the vortical structure, more robust computational procedure, and more accurate aerodynamic loads if compared with the FVC2-Q model. Therefore, the FVC2-L2 was employed in the following analysis of the forward flight rotor case and aeroacoustic studies.
- The well-documented HART-II rotor BL case was simulated to analyze the performance of the FVC2-L2 model on the prediction of BVI phenomena. Results showed a better wake and higher resolution of the vortical structures than the CFD solution without confinement. Additionally, the FVC2-L2 model maintains the robust aerodynamic prediction of the standard CFD solution and better predicts the BVI effects on the advancing and retreating blade side.
- The non-lifting UH-1H hovering rotor and the AH-1/OLS rotor in low-speed descending flight were computed to investigate the effects of the FVC2-L2 model on aeroacoustic prediction. For the non-lifting rotor case, although no vortices were shed from the blade tip, an improvement in the acoustic pressure negative peaks was observed using the FVC2-L2 model. When it comes to the BVI-dominated cases, the case with the FVC2-L2 model significantly increased the high-frequency harmonics noise but had negligible influence on the low-frequency noise in the acoustic signatures when compared to the case without VC. It means that the BVI effects on the acoustic signals at all tested microphone positions were well captured by the results involving the FVC2-L2 model. The results demonstrated the positive effects of the FVC2-L2 model on the prediction of helicopter rotor noise.

CHAPTER 5

Grid Redistribution Method Development and Preliminary Validation

The previous chapter presented a vortex feature-based VC2 method to enhance the resolution of vortices in aerodynamic wakes at a modest computational cost. This chapter introduces the r-refinement technique, an alternative approach for improving the vortex resolution without creating additional mesh points. The r-refinement method, also known as the grid redistribution method, relies on a three-dimensional implementation of the Jacobian-weighted elliptic grid generation approach for redistributing the structured mesh points. The process for implementing the Knupp's original two-dimensional Jacobian-weighted elliptic grid generation approach is described in section 5.1, some examples are employed for validation. Then, section 5.2 details the derivation of the three-dimensional extension of Knupp's approach and validates the extended method by several test examples.

5.1 2D Jacobian-Weighted Elliptic Grid Generation Approach

5.1.1 Derivation of the 2D Jacobian-Weighted Elliptic Equation

The basis of the two-dimensional structured grid generation is to construct a transformation $\mathbf{F}$ that maps a planar grid from a computational domain Ω_C to the physical domain Ω_P:

$$\mathbf{F} : \Omega_C \rightarrow \Omega_P \tag{5.1}$$

For clarity, an example of mapping the grid from domain Ω_C to Ω_P is illustrated in Figure 5.1, where $\boldsymbol{\xi} = (\xi, \eta)$ represents the computational coordinates in computational space and $\boldsymbol{x} = (x(\xi, \eta), z(\xi, \eta))$ are the physical coordinates in physical space. Accordingly, the Jacobian matrix of the map and its determinant is given by

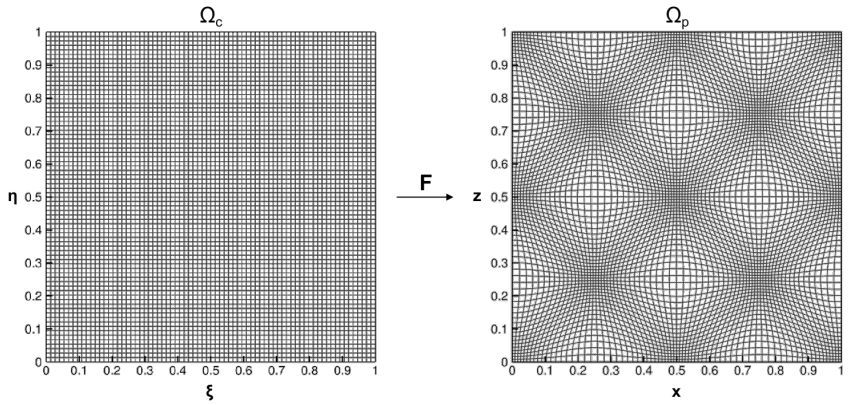

Figure 5.1: *An example of a mapping from the computational domain to the physical domain.*

$$\boldsymbol{J}(\boldsymbol{x}) = \frac{\partial(x,z)}{\partial(\xi,\eta)} = \begin{bmatrix} x_\xi & x_\eta \\ z_\xi & z_\eta \end{bmatrix}, \tag{5.2a}$$

$$\det(\boldsymbol{J}) = \sqrt{g} = x_\xi z_\eta - x_\eta z_\xi \tag{5.2b}$$

The Jacobian matrix can be viewed as two column vectors,

$$\boldsymbol{J} = (\boldsymbol{e}_\xi | \boldsymbol{e}_\eta) \tag{5.3}$$

with

$$\begin{aligned} \boldsymbol{e}_\xi &= (x_\xi, z_\xi)^T \\ \boldsymbol{e}_\eta &= (x_\eta, z_\eta)^T \end{aligned} \tag{5.4}$$

where $\boldsymbol{e}_\xi$ and $\boldsymbol{e}_\eta$ represent the local tangent vectors of the curve in the physical domain at the point (ξ_0, η_0). Figure 5.2 illustrates the geometrical interpretation of Jacobian matrix. l_1 and l_2 are the lengths of $\boldsymbol{e}_\xi$ and $\boldsymbol{e}_\eta$, respectively, associated with the grid spacing. θ_1 and θ_2 are the angles of the two tangent vectors to the x-axis, respectively, providing the local alignment of the grid cell. As a result, the Jacobian matrix of the mapping between two domains can be rewritten as the product of the direction of the tangent vectors and the local length scale:

$$\boldsymbol{J} = \begin{bmatrix} \cos\theta_1 & \cos\theta_2 \\ \sin\theta_1 & \sin\theta_2 \end{bmatrix} \cdot \begin{bmatrix} l_1 & 0 \\ 0 & l_2 \end{bmatrix} = \begin{bmatrix} l_1\cos\theta_1 & l_2\cos\theta_2 \\ l_1\sin\theta_1 & l_2\sin\theta_2 \end{bmatrix} \tag{5.5}$$

Furthermore, the difference between θ_2 and θ_1 can be used to control the grid orthogonality. It is natural to set $\theta_1 = \theta_o$ and $\theta_2 = \theta + \pi/2$ in the case where grid orthogonality is desired. Therefore, equation 5.5 is changed to

$$\boldsymbol{J} = \begin{bmatrix} l_1\cos\theta_o & -l_2\sin\theta_o \\ l_1\sin\theta_o & l_2\cos\theta_o \end{bmatrix} \tag{5.6}$$

From above expression and equation 5.2, it is easy to get the relations below

$$\begin{cases} l_1 = \sqrt{x_\xi^2 + z_\xi^2} = \sqrt{g_{11}} \\ l_2 = \sqrt{x_\eta^2 + z_\eta^2} = \sqrt{g_{22}} \\ l_1 l_2 = \sqrt{x_\xi z_\eta - x_\eta z_\xi} = \sqrt{g} \end{cases} \tag{5.7}$$

in which g_{11} and g_{22} are the elements of metric tensor g_{ij}.

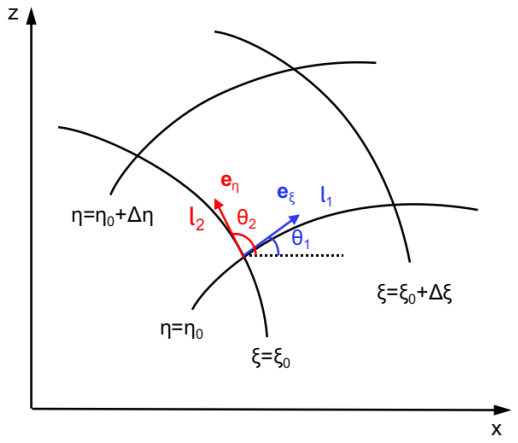

Figure 5.2: *Geometrical interpretation of 2D Jacobian matrix.*

In elliptic grid generation, the above transformation can be obtained by solving a set of Poisson equations with $\boldsymbol{x}$ as the dependent variables and $\boldsymbol{\xi}$ as the independent variables. The general form of the Poisson equations (in two dimensions) can be written as

$$\begin{cases} g_{22}x_{\xi\xi} - 2g_{12}x_{\xi\eta} + g_{11}x_{\eta\eta} = P(\xi,\eta) \\ g_{22}z_{\xi\xi} - 2g_{12}z_{\xi\eta} + g_{11}z_{\eta\eta} = Q(\xi,\eta) \end{cases} \tag{5.8}$$

where the left-hand terms can be abbreviated to the well-known Winslow operator, $\boldsymbol{\mathcal{Q}}_w\boldsymbol{x}$, $P(\xi,\eta)$ and $Q(\xi,\eta)$ at the right-hand side represent the source terms that used for controlling grid spacing, area, orthogonality, and alignment. $x_{\xi\xi} = \frac{\partial^2 x}{\partial \xi^2}$ (and similar for other second derivatives).

To determine the source terms, the Jacobian-weighted method performs a least-squares fit to a prescribed weight matrix $\boldsymbol{S}$ such that the inverse Jacobian matrix $\boldsymbol{J}^{-1}$ is as close as possible to weight $\boldsymbol{S}$. The least-square fit is achieved using the variational principle where the following function is minimised:

$$I[\boldsymbol{J}^{-1}] = \int_{\Omega_P} \|\boldsymbol{J}^{-1} - \boldsymbol{S}\|_F^2 d\boldsymbol{x} \tag{5.9}$$

where $\|\cdot\|_F$ represents the Frobenius norm that used to measure the closeness of two matrices. With this formulation, the weight matrix $\boldsymbol{S}$ is assigned with a clear geometric interpretation - the target inverse Jacobian matrix $\boldsymbol{J}^{-1}$. As a result, the corresponding Euler-Lagrange equation can be expressed as:

$$div_{\boldsymbol{x}}\left(\boldsymbol{J}^{-1} - \boldsymbol{S}\right) = \boldsymbol{0} \tag{5.10}$$

Afterward, the Jacobian-weighted elliptic grid generation equation can be derived in the following steps with $\boldsymbol{C} = \sqrt{g}\boldsymbol{J}^{-T}$ and $\boldsymbol{\mathcal{G}} = \boldsymbol{J}^T\boldsymbol{J}$:

$$\begin{aligned} div_{\boldsymbol{x}}\boldsymbol{J}^{-1} &= div_{\boldsymbol{x}}\boldsymbol{S}, \\ div_{\boldsymbol{\xi}}\boldsymbol{J}^{-1}\boldsymbol{C} &= div_{\boldsymbol{\xi}}\boldsymbol{S}\boldsymbol{C}, \\ div_{\boldsymbol{\xi}}\sqrt{g}\boldsymbol{\mathcal{G}}^{-1} &= [\nabla_{\boldsymbol{\xi}}\boldsymbol{S}]\,\boldsymbol{C}, \\ -\sqrt{g}\boldsymbol{J}div_{\boldsymbol{\xi}}\sqrt{g}\boldsymbol{\mathcal{G}}^{-1} &= -\sqrt{g}\boldsymbol{J}\,[\nabla_{\boldsymbol{\xi}}\boldsymbol{S}]\,\boldsymbol{C}, \\ g\,[\nabla_{\boldsymbol{\xi}}\boldsymbol{J}]\,\boldsymbol{\mathcal{G}}^{-1} &= -\sqrt{g}\boldsymbol{J}\,[\nabla_{\boldsymbol{\xi}}\boldsymbol{S}]\,\boldsymbol{C}, \\ \boldsymbol{\mathcal{Q}}_w\boldsymbol{x} &= -\sqrt{g}\boldsymbol{J}\,[\nabla_{\boldsymbol{\xi}}\boldsymbol{S}]\,\boldsymbol{C} \end{aligned} \tag{5.11}$$

The two-dimensional form of the Jacobian-weighted equation is explicitly obtained:

$$\begin{cases} g_{22}x_{\xi\xi} - 2g_{12}x_{\xi\eta} + g_{11}x_{\eta\eta} = P \\ g_{22}z_{\xi\xi} - 2g_{12}z_{\xi\eta} + g_{11}z_{\eta\eta} = Q \end{cases} \tag{5.12}$$

with

$$\begin{cases} P = -\sqrt{g}\,(x_\xi R_1 + x_\eta R_2) \\ Q = -\sqrt{g}\,(z_\xi R_1 + z_\eta R_2) \end{cases} \tag{5.13}$$

and

$$\begin{cases} R_1 = (S_{11})_\xi\, z_\eta - (S_{12})_\xi\, x_\eta - (S_{11})_\eta\, z_\xi + (S_{12})_\eta\, x_\xi \\ R_2 = (S_{21})_\xi\, z_\eta - (S_{22})_\xi\, x_\eta - (S_{21})_\eta\, z_\xi + (S_{22})_\eta\, x_\xi \end{cases} \tag{5.14}$$

From equation 5.6, the weights matrix $\boldsymbol{S}$ is defined as

$$\boldsymbol{S} = \boldsymbol{J}^{-1} = \begin{bmatrix} \dfrac{\cos\theta_o}{l_1} & \dfrac{\sin\theta_o}{l_1} \\ -\dfrac{\sin\theta_o}{l_2} & \dfrac{\cos\theta_o}{l_2} \end{bmatrix} \tag{5.15}$$

5.1.2 Numerical Implementation

It is clear that the 2D Jacobian-weighted elliptic equation 5.12 is nonlinear because the coefficients of the left-hand side terms are functions of the dependent variables x and z. In general, nonlinear equations are significantly more troublesome to solve analytically. For this reason, finite-difference schemes are always required to numerically approximate the nonlinear equations, resulting a system of linear equations.

In this work, a uniform grid with mesh size $\Delta\xi = L_\xi/(I_m - 1)$ and $\Delta\eta = L_\eta/(J_m - 1)$ on the computational domain is employed to discretise the 2D Jacobian-weighted elliptic equation 5.12 in space. The corresponding mesh points in the physical domain is denoted by

$$x_{i,j} = x(\xi_i, \eta_j), \quad z_{i,j} = z(\xi_i, \eta_j), \quad i = 1, \cdots, I_m \text{ and } j = 1, \cdots, J_m \tag{5.16}$$

A set of central difference schemes are used to discretise the partial derivatives in equa-

tion 5.12 for $i = 2, \cdots, I_m - 1$ and $j = 2, \cdots, J_m - 1$,

$$(x_\xi)_{i,j} \approx \frac{x_{i+1,j} - x_{i-1,j}}{2\Delta\xi} \tag{5.17a}$$

$$(x_\eta)_{i,j} \approx \frac{x_{i,j+1} - x_{i,j-1}}{2\Delta\eta} \tag{5.17b}$$

$$(x_{\xi\xi})_{i,j} \approx \frac{x_{i+1,j} - 2x_{i,j} + x_{i-1,j}}{\Delta\xi^2} \tag{5.17c}$$

$$(x_{\eta\eta})_{i,j} \approx \frac{x_{i,j+1} - 2x_{i,j} + x_{i,j-1}}{\Delta\eta^2} \tag{5.17d}$$

$$(x_{\xi\eta})_{i,j} \approx \frac{x_{i+1,j+1} - x_{i+1,j-1} - x_{i-1,j+1} + x_{i-1,j-1}}{4\Delta\xi\Delta\eta} \tag{5.17e}$$

At the boundaries, solving the equation 5.12 is subject to the following Neumann boundary condition:

$$\begin{aligned} x_{i,1} = x_{i,2}, \quad \text{and} \quad x_{i,J_m} = x_{i,J_m-1}, \quad \text{for} \quad i = 1, \cdots, I_m \\ z_{1,j} = z_{2,j}, \quad \text{and} \quad z_{I_m,j} = z_{I_m-1,j}, \quad \text{for} \quad j = 1, \cdots, J_m \end{aligned} \tag{5.18}$$

The numerically implementation of the 2D Jacobian-weighted elliptic equation follows the Point Successive Over-Relaxation (PSOR) algorithm, which is divided in three steps:

- **Step 1:** Starting from the initial uniform mesh in the physical domain, the Gauss-Seidel iteration method is adopted to compute the temporary positions for grid points, denoted as $x_{i,j}^{tmp}$, $z_{i,j}^{tmp}$,
- **Step 2:** The new positions $x_{i,j}^{new}$, $z_{i,j}^{new}$ are computed by performing a SOR type relaxation, which is a weighted average of the old position $x_{i,j}^{old}$, $z_{i,j}^{old}$ and temporary positions $x_{i,j}^{tmp}$, $z_{i,j}^{tmp}$:

  $$x_{i,j}^{new} = \omega \cdot x_{i,j}^{tmp} + (1 - \omega) \cdot x_{i,j}^{old} \tag{5.19}$$

  where ω is the relaxation factor with range of $(0, 2)$. Note that the Gauss-Seidel iteration method is recovered for ω = 1. In this work, the PSOR algorithm is conducted with ω=1.2 or 1.5.
- **Step 3:** The PSOR iteration is stopped by satisfying the following convergence criterion, otherwise assigning x^{new}, z^{new} to x^{old}, z^{old}, and repeating **Step 1** and **Step 2**.

  $$\max_{i,j}(|x_{i,j}^{new} - x_{i,j}^{old}|, |z_{i,j}^{new} - z_{i,j}^{old}|) \leq \epsilon \tag{5.20}$$

  for some specified tolerance ϵ chosen to be between 10^{-4} to 10^{-6}.

5.1.3 Numerical Examples

This section presents some examples to verify the implementation of the 2D Jacobian-weighted elliptic equation on various problems. The aim is to show that the method is able to flexibly attract mesh nodes to specified locations in the physical domain by devising weights $\boldsymbol{S}$. In the first example, we consider the attraction of multiple points,

where the mesh points are clustered towards the predetermined points in the physical space. The second case we employ is the adaption around a prescribed trajectory, where the grid points are adapted to a cosine trajectory. The last is a feature-based example in which the attraction of grid points depends on a predefined "solution" function.

Point Attraction This example supposes the grid nodes are attracted to thirteen predefined distinct points in the physical domain. The control angle for grid orthogonality is $\theta = 0$, the length-scale function l_1 and l_2 are defined as the form

$$l_1 = l_2 = \begin{cases} 1 - a & r \leq R_1 \\ 1 - a + a\left(3 - 2\dfrac{r - R_1}{R_2 - R_1}\right)\left(\dfrac{r - R_1}{R_2 - R_1}\right)^2 & R_1 < r < R_2 \\ 1 & r \geq R2 \end{cases} \tag{5.21}$$

where r is the minimum distance from the grid point (x, z) to the predetermined points (x_n, z_n). The region of $r \leq R1$ defines the local refinement, $r \geq R2$ represents the region without attraction, and $R_1 < r < R_2$ denotes the transition region. The parameter $0 < a < 1$ controls the strength of the redistribution. The closer the value of a is to 1, the higher level of refinement that will be imposed. For instance, if a is fixed at 0.8, the resulting grid spacing in the local refinement region should be 0.2 of the original grid spacing. However, since the Jacobian-weighted elliptic method is only a least-square fit of the inverse Jacobian matrix $\boldsymbol{J}^{-1}$ to a weight matrix $\boldsymbol{S}$, the ratio between the resulting grid spacing and the original spacing may not be as accurate as the previous analysis.

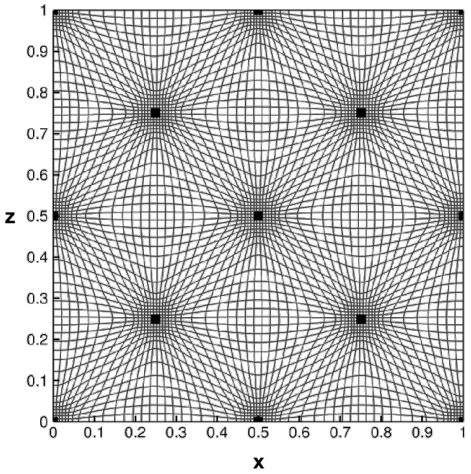

Figure 5.3: *The mesh attracted to thirteen points (black nodes represent the prescribed points).*

In this work, the computational domain $\Omega_C = [0, 1]^2$ is split into a grid of $n_\xi \times n_\eta$ points, with $n_\xi = n_\eta = 60$ ($N = 3600$) and is mapped into the physical domain with the Dirichlet conditions defined in equation 5.18 through the 2D Transfinite Interpolation (TFI) method. Figure 5.3 shows results for thirteen attraction points $(x_1, z_1) = (0, 0)$, $(x_2, z_2) = (1/2, 0)$, $(x_3, z_3) = (1, 0)$, $(x_4, z_4) = (1/4, 1/4)$, $(x_5, z_5) = (3/4, 1/4)$, $(x_6, z_6) = (0, 1/2)$, $(x_7, z_7) = (1/2, 1/2)$, $(x_8, z_8) = (1, 1/2)$, $(x_9, z_9) = (1/4, 3/4)$, $(x_{10}, z_{10}) =$

$(3/4, 3/4)$, (x_{11}, z_{11}) = $(0, 1)$, (x_{12}, z_{12}) = $(1/2, 1)$, (x_{13}, z_{13}) = $(1, 1)$, where the radii of the local refinement and transition region were set to $R_1 = 0.03$ and $R_2 = 0.12$, respectively; the attraction strength was set to $a = 0.75$; the convergence tolerance of the mesh was set to $\epsilon = 10^{-6}$. It is clear from this plot that the redistributed grid is following the predefined points closely.

Prescribed Trajectory Adaption In this next example, we define a prescribed trajectory that localises on a sine-wave form. This example was chosen because it resulted in a very non-uniform and distorted mesh, and therefore it was a major challenge for the algorithm. The function of the trajectory is given by

$$z = \frac{1}{2} + \frac{\sin(2\pi x)}{4} \tag{5.22}$$

The domain is discretised into 60×60 grid points. The 2D Jacobian-weighted elliptic equation was applied to the prescribed trajectory attraction problem with the same formulation of the length-scale function as defined in equation 5.21. The radii of the local refinement and transition region were $R_1 = 0.01$ and $R_2 = 0.04$, respectively. In this case, the 2D Jacobian-weighted elliptic grid solver will be divergence if $a > 0.78$. As the initial grid spacing is much larger than the resultant spacing, it is impossible to achieve a sufficient grid resolution with only one level of redistribution. For this reason, multi-level grid refinement by multiple uses of the PSOR algorithm is required. Three levels of attraction strength was applied with a_1 = 0.6, a_2 = 0.7, and a_3 = 0.8. The exponential convergence of the mesh was specified as $\epsilon = 10^{-6}$.

The mesh generated by solving the 2D Jacobian-weighted elliptic equation using the PSOR algorithm is shown in Figure 5.4, where the grid after each redistribution level is displayed. It is found that the multi-level grid refinement is able to further generate sufficient grid resolution. Moreover, the results demonstrate the capability of the 2D Jacobian-weighted elliptic method to adapt the grid to a prescribed trajectory.

Feature-based Adaption The last example is taken directly from [133], where the solution function is given by

$$f(x, z) = \tanh R\left[r^2 - (x - x_c)^2 - (z - z_c)^2\right] \tag{5.23}$$

This function is defined as a circular "hill" of radius r centered on the position of $x = x_c$, $z = z_c$. In this example, we define the same values as used in Ref [133], $r = 1/4$, $x_c = 1/2$, and $z_c = 1/2$. R is used to describe the steepness of the hill. The higher the R value, the steeper the hill. Then the control angle $\theta_o = 0$, the length-scale function $l(\boldsymbol{x})$, which creates small cells in physical space where $|\nabla_{\boldsymbol{x}} f|$ is large, is given by

$$l_1 = l_2 = \frac{1}{1 + a|\nabla_{\boldsymbol{x}} f|} \tag{5.24}$$

where a is a positive parameter that controls the strength of the attraction; $\nabla_{\boldsymbol{x}} f = [f_x, f_z]^T$ that can be expressed follows that

$$f_x = \frac{1}{\sqrt{g}}\left(z_\eta f_\xi - z_\xi f_\eta\right) \tag{5.25a}$$

$$f_z = \frac{1}{\sqrt{g}}\left(x_\xi f_\eta - x_\eta f_\xi\right) \tag{5.25b}$$

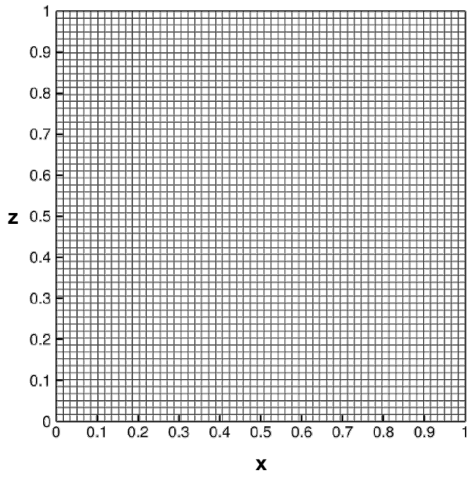

(a) *Initial grid*

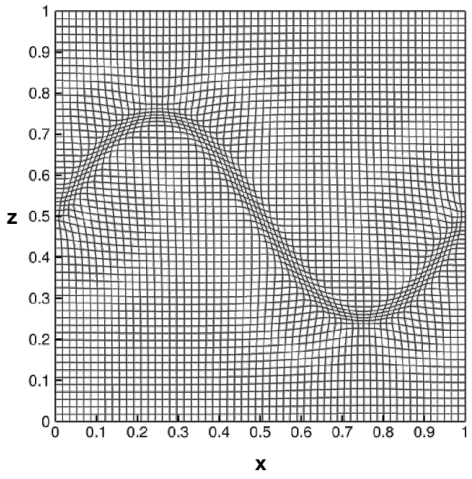

(b) *Grid redistribution - Level 1,* $a_1 = 0.6$

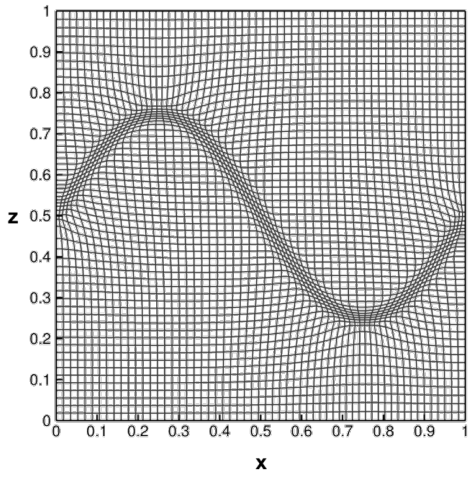

(c) *Grid redistribution - Level 2,* $a_2 = 0.7$

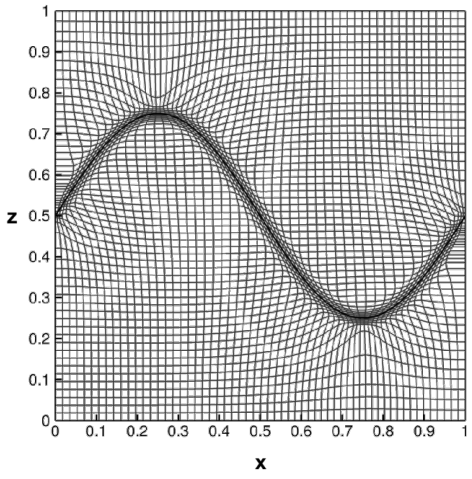

(d) *Grid redistribution - Level 3,* $a_3 = 0.8$

Figure 5.4: *The mesh attracted to a prescribed sine-wave trajectory (black curve is the prescribed trajectory).*

In numerical discretisations, a uniform square grid with mesh size $\Delta\xi = \Delta\eta = 1/(N-1)$ is employed on the computational domain such that the equations 5.25 become

$$[f_x]_{i,j} = \begin{cases} \dfrac{[z_\eta]_{i,j}[f_\xi]_{i,j} - [z_\xi]_{i,j}[f_\eta]_{i,j}}{\sqrt{g_{i,j}}} & \text{for} \quad i,j = 2,\cdots N-1 \\ \dfrac{[z_\eta]_{i,j}[f_\xi]_{i,j}}{\sqrt{g_{i,j}}} & \text{for} \quad i,j = 1,N \end{cases} \tag{5.26}$$

$$[f_z]_{i,j} = \begin{cases} \dfrac{[x_\xi]_{i,j}[f_\eta]_{i,j} - [x_\eta]_{i,j}[f_\xi]_{i,j}}{\sqrt{g_{i,j}}} & \text{for} \quad i,j = 2,\cdots N-1 \\ \dfrac{[x_\xi]_{i,j}[f_\eta]_{i,j}}{\sqrt{g_{i,j}}} & \text{for} \quad i,j = 1,N \end{cases} \tag{5.27}$$

The approximation of the first order derivatives of f as follows

$$[f_\xi]_{i,j} = \begin{cases} \dfrac{f(x_{i+1}, z_j) - f(x_{i-1}, z_j)}{2\Delta\xi} & \text{for} \quad i, j = 2, \cdots N-1 \\ \dfrac{-3f(x_1, z_j) + 4f(x_2, z_j) - f(x_3, z_j)}{2\Delta\xi} & \text{for} \quad i = 1 \\ \dfrac{f(x_{N-2}, z_j) - 4f(x_{N-1}, z_j) + 3f(x_N, z_j)}{2\Delta\xi} & \text{for} \quad i = N \end{cases} \tag{5.28}$$

$$[f_\eta]_{i,j} = \begin{cases} \dfrac{f(x_i, z_{j+1}) - f(x_i, z_{j-1})}{2\Delta\eta} & \text{for} \quad i, j = 2, \cdots N-1 \\ \dfrac{-3f(x_i, z_1) + 4f(x_i, z_2) - f(x_i, z_3)}{2\Delta\eta} & \text{for} \quad j = 1 \\ \dfrac{f(x_i, z_{N-2}) - 4f(x_i, z_{N-1}) + 3f(x_i, z_N)}{2\Delta\eta} & \text{for} \quad j = N \end{cases} \tag{5.29}$$

and similar for other first derivatives.

The purpose of this example is to validate the effectiveness of the implemented mesh redistribution method for the feature-based problem. Three grids are solved with the same parameters in [133], as illustrated in Figure 5.5. A gentle hill is first created on a coarse grid (20×20 cells) with $R = 20$ and $a = 0.2$. Then, a steep hills are achieved on a finer grid (40×40 cells) with $R = 100$ and $a = 0.1$. The last case employs a finest grid (60×60 cells) with $R = 100$ and $a = 0.1$. It can be see that these results are very close to those obtained in [133]. The effectiveness of the 2D Jacobian-weighted elliptic grid solver is well demonstrated.

5.2 3D Jacobian-Weighted Elliptic Grid Generation Approach

5.2.1 3D Extension of the Jacobian-Weighted Elliptic Equation

This section extended the Jacobian-weighted elliptic method from two dimensions to three dimensions. The extension may be derived along the line of the 2D method described in previous section.

In terms of three-dimensional problems, the computational and physical coordinates become $\boldsymbol{\xi} = (\xi, \eta, \zeta)$ and $\boldsymbol{x} = (x(\xi, \eta, \zeta), y(\xi, \eta, \zeta), z(\xi, \eta, \zeta))$, respectively. Then the Jacobian matrix of the mapping and its determinant are given below.

$$\boldsymbol{J}(\boldsymbol{x}) = \frac{\partial(x, y, z)}{\partial(\xi, \eta, \zeta)} = \begin{bmatrix} x_\xi & x_\eta & x_\zeta \\ y_\xi & y_\eta & y_\zeta \\ z_\xi & z_\eta & z_\zeta \end{bmatrix} \tag{5.30a}$$

$$\det(\boldsymbol{J}) = \sqrt{g} = x_\xi y_\eta z_\zeta + x_\zeta y_\xi z_\eta + x_\eta y_\zeta z_\xi - x_\zeta y_\eta z_\xi - x_\xi y_\zeta z_\eta - x_\eta y_\xi z_\zeta \tag{5.30b}$$

Considering a 3D cell in the physical space, $\boldsymbol{J}$ can be viewed as three unit local tangent vectors of the curve $(\boldsymbol{e}_\xi, \boldsymbol{e}_\eta, \boldsymbol{e}_\zeta)$ in the physical space at the point (ξ_0, η_0, ζ_0), as shown in Figure 5.6. Nine variables of l_1, l_2, l_3, θ_1, θ_2, θ_3, ϕ_1, ϕ_2, ϕ_3 are adopted

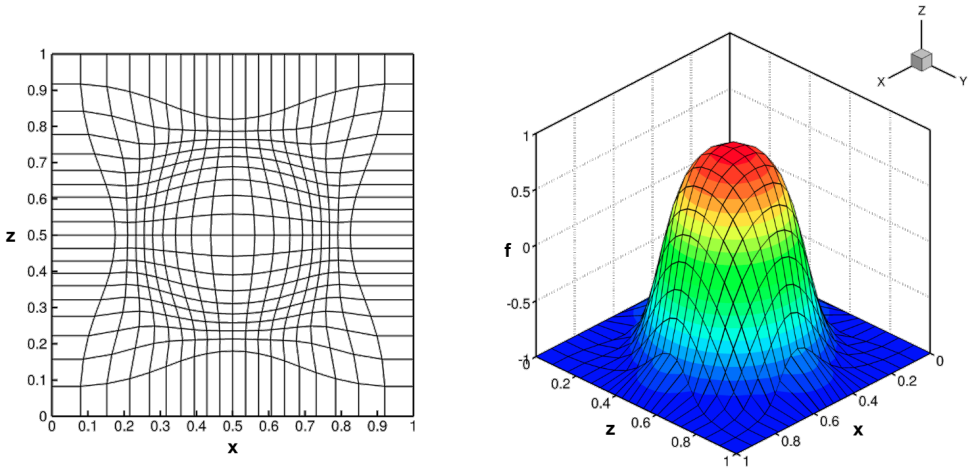

(a) *Gentle hill,* $R = 20$, $a = 0.2$, 20×20 *cells*

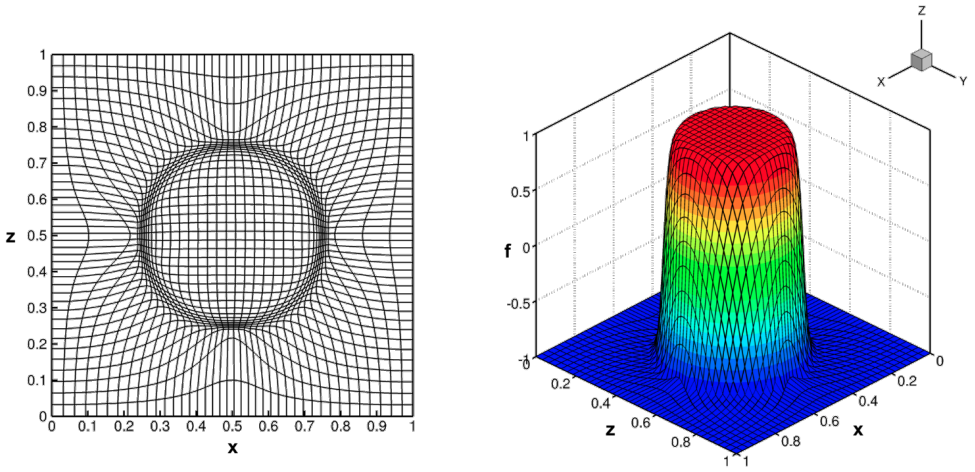

(b) *Steep hill,* $R = 100$, $a = 0.1$, 40×40 *cells*

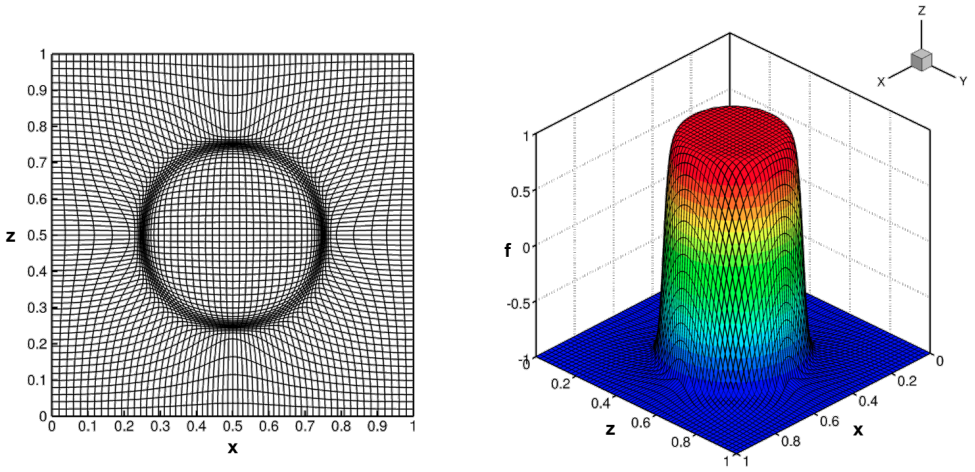

(c) *Steep hill,* $R = 100$, $a = 0.1$, 60×60 *cells*

Figure 5.5: *Feature-based 2D grid redistribution case (the mesh was rendered by function value)*

to control the geometry of cell. l_i is the length scaling factor used for controlling the grid spacing. The azimuth angle θ_i, lies in the range of $[0, 2\pi]$, represents the angle between the projection of unit vector onto the x-y plane and x-axis. The polar angle ϕ_i, lies in the range of $[0, \pi]$, defines the angle between the unit vector and the z-axis. As a result, $\boldsymbol{J}$ can be interpreted geometrically as the product of the directional matrix and the length control matrix.

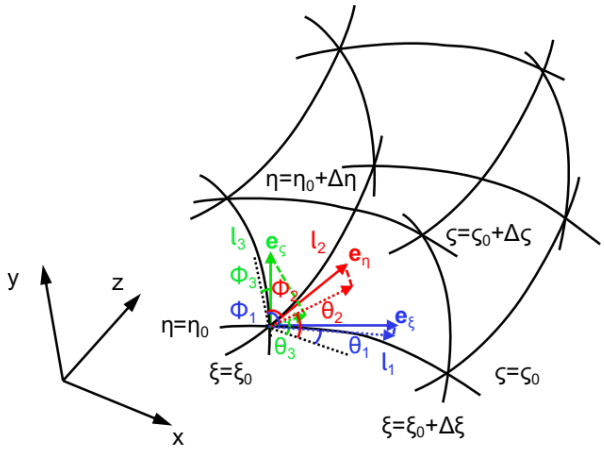

Figure 5.6: *Geometrical interpretation of 3D Jacobian matrix.*

$$\boldsymbol{J} = \begin{bmatrix} \sin\phi_1\cos\theta_1 & \sin\phi_2\cos\theta_2 & \sin\phi_3\cos\theta_3 \\ \sin\phi_1\sin\theta_1 & \sin\phi_2\sin\theta_2 & \sin\phi_3\sin\theta_3 \\ \cos\phi_1 & \cos\phi_2 & \cos\phi_3 \end{bmatrix} \cdot \begin{bmatrix} l_1 & 0 & 0 \\ 0 & l_2 & 0 \\ 0 & 0 & l_3 \end{bmatrix} \tag{5.31}$$

Particularly, in order to achieve good grid orthogonality, the unit vectors $\boldsymbol{e}_\xi$, $\boldsymbol{e}_\eta$, and $\boldsymbol{e}_\zeta$ satisfy

$$\boldsymbol{e_\xi} \cdot \boldsymbol{e_\eta} = 0, \quad \text{and} \quad \boldsymbol{e_\xi} \cdot \boldsymbol{e_\zeta} = 0, \quad \text{and} \quad \boldsymbol{e_\eta} \cdot \boldsymbol{e_\zeta} = 0 \tag{5.32}$$

with

$$\theta_2 = \theta_1 + \frac{\pi}{2}, \quad \text{and} \quad \phi_1 = \phi_3 + \frac{\pi}{2}, \quad \text{and} \quad \phi_2 = \phi_3 + \frac{\pi}{2} \tag{5.33}$$

Accordingly, we set $\theta_1 = \theta_o$, $\boldsymbol{J}$ can be rewritten as:

$$\boldsymbol{J} = \begin{bmatrix} l_1\cos\theta_o & -l_2\sin\theta_o & 0 \\ l_1\sin\theta_o & l_2\cos\theta_o & 0 \\ 0 & 0 & l_3 \end{bmatrix} \tag{5.34}$$

Following a similar derivation process of the 2D method, the 3D Jacobian-weighted elliptic equation also gives

$$\boldsymbol{\mathcal{Q}}_w \boldsymbol{x} = -g\boldsymbol{J}\left[\nabla_{\boldsymbol{\xi}}\boldsymbol{S}\right]\boldsymbol{J}^{-T} \tag{5.35}$$

with the components of $\nabla_{\boldsymbol{\xi}}\boldsymbol{S}$ ($\boldsymbol{S}$ is a tensor) defines

$$\left(\left[\nabla_{\boldsymbol{\xi}}\boldsymbol{S}\right]\boldsymbol{J}^{-T}\right)_i = \sum_{j=1}^{3}\sum_{k=1}^{3}\frac{\partial S_{ij}}{\partial \xi_k}\left(\boldsymbol{J}^{-T}\right)_{jk} \tag{5.36}$$

The resulting form of the 3D Jacobian-weighted elliptic equation can be written explicitly as

$$\begin{cases} g^{11}x_{\xi\xi} + g^{22}x_{\eta\eta} + g^{33}x_{\zeta\zeta} + 2g^{12}x_{\xi\eta} + 2g^{13}x_{\xi\zeta} + 2g^{23}x_{\eta\zeta} = P \\ g^{11}y_{\xi\xi} + g^{22}y_{\eta\eta} + g^{33}y_{\zeta\zeta} + 2g^{12}y_{\xi\eta} + 2g^{13}y_{\xi\zeta} + 2g^{23}y_{\eta\zeta} = Q \\ g^{11}z_{\xi\xi} + g^{22}z_{\eta\eta} + g^{33}z_{\zeta\zeta} + 2g^{12}z_{\xi\eta} + 2g^{13}z_{\xi\zeta} + 2g^{23}z_{\eta\zeta} = R \end{cases} \tag{5.37}$$

with the source terms P, Q, and R as follows

$$\begin{cases} P = -\left(x_\xi R_1 + x_\eta R_2 + x_\zeta R_3\right) \\ Q = -\left(y_\xi R_1 + y_\eta R_2 + y_\zeta R_3\right) \\ R = -\left(z_\xi R_1 + z_\eta R_2 + z_\zeta R_3\right) \end{cases} \tag{5.38}$$

$$\begin{cases} R_1 = (S_{11})_\xi \xi_x + (S_{11})_\eta \eta_x + (S_{11})_\zeta \zeta_x + (S_{12})_\xi \xi_y + (S_{12})_\eta \eta_y + (S_{12})_\zeta \zeta_y \\ \qquad\qquad + (S_{13})_\xi \xi_z + (S_{13})_\eta \eta_z + (S_{13})_\zeta \zeta_z \\ R_2 = (S_{21})_\xi \xi_x + (S_{21})_\eta \eta_x + (S_{21})_\zeta \zeta_x + (S_{22})_\xi \xi_y + (S_{22})_\eta \eta_y + (S_{22})_\zeta \zeta_y \\ \qquad\qquad + (S_{23})_\xi \xi_z + (S_{23})_\eta \eta_z + (S_{23})_\zeta \zeta_z \\ R_3 = (S_{31})_\xi \xi_x + (S_{31})_\eta \eta_x + (S_{31})_\zeta \zeta_x + (S_{32})_\xi \xi_y + (S_{32})_\eta \eta_y + (S_{32})_\zeta \zeta_y \\ \qquad\qquad + (S_{33})_\xi \xi_z + (S_{33})_\eta \eta_z + (S_{33})_\zeta \zeta_z \end{cases} \tag{5.39}$$

where each element of inverse metric tensor g^{ij} may be represented as

$$\begin{cases} g^{11} = \left(g_{22}g_{33} - g_{23}^2\right)/g \\ g^{22} = \left(g_{33}g_{11} - g_{13}^2\right)/g \\ g^{33} = \left(g_{11}g_{22} - g_{12}^2\right)/g \\ g^{12} = \left(g_{23}g_{13} - g_{12}g_{33}\right)/g \\ g^{13} = \left(g_{12}g_{23} - g_{13}g_{22}\right)/g \\ g^{23} = \left(g_{13}g_{12} - g_{23}g_{11}\right)/g \end{cases}$$

with

$$\begin{cases} g_{11} = x_\xi^2 + y_\xi^2 + z_\xi^2 \\ g_{22} = x_\eta^2 + y_\eta^2 + z_\eta^2 \\ g_{33} = x_\zeta^2 + y_\zeta^2 + z_\zeta^2 \\ g_{12} = x_\xi x_\eta + y_\xi y_\eta + z_\xi z_\eta \\ g_{13} = x_\xi x_\zeta + y_\xi y_\zeta + z_\xi z_\zeta \\ g_{23} = x_\eta x_\zeta + y_\eta y_\zeta + z_\eta z_\zeta \end{cases}$$

The transformations between the derivatives of the computational coordinates and physical coordinates are expressed as

$$\begin{cases} \xi_x = \dfrac{1}{\sqrt{g}}\left(y_\eta z_\zeta - z_\eta y_\zeta\right), \quad \xi_y = \dfrac{1}{\sqrt{g}}\left(z_\eta x_\zeta - x_\eta z_\zeta\right), \quad \xi_z = \dfrac{1}{\sqrt{g}}\left(x_\eta y_\zeta - y_\eta x_\zeta\right) \\ \eta_x = \dfrac{1}{\sqrt{g}}\left(y_\zeta z_\xi - z_\zeta y_\xi\right), \quad \eta_y = \dfrac{1}{\sqrt{g}}\left(z_\zeta x_\xi - x_\zeta z_\xi\right), \quad \eta_z = \dfrac{1}{\sqrt{g}}\left(x_\zeta y_\xi - y_\zeta x_\xi\right) \\ \zeta_x = \dfrac{1}{\sqrt{g}}\left(y_\xi z_\eta - z_\xi y_\eta\right), \quad \zeta_y = \dfrac{1}{\sqrt{g}}\left(z_\xi x_\eta - x_\xi z_\eta\right), \quad \zeta_z = \dfrac{1}{\sqrt{g}}\left(x_\xi y_\eta - y_\xi x_\eta\right) \end{cases}$$

In addition, the weight matrix $\boldsymbol{S}$ corresponding to equation 5.34 takes the form

$$\boldsymbol{S} = \boldsymbol{J}^{-1} = \begin{bmatrix} \dfrac{\cos\theta_o}{l_1} & \dfrac{\sin\theta_o}{l_1} & 0 \\ -\dfrac{\sin\theta_o}{l_2} & \dfrac{\cos\theta_o}{l_2} & 0 \\ 0 & 0 & \dfrac{1}{l_3} \end{bmatrix} \tag{5.40}$$

5.2.2 Numerical Implementation

Supposing that a uniform grid on the computational domain is discretised into $I_m \times J_m \times K_m$ grid nodes such that

$$\Delta\xi = \frac{L_\xi}{I_m - 1}, \quad \Delta\eta = \frac{L_\eta}{J_m - 1}, \quad \Delta\zeta = \frac{L_\zeta}{K_m - 1} \tag{5.41}$$

The partial derivatives of the interior nodes ($i = 2, \cdots, I_m - 1$, $j = 2, \cdots, J_m - 1$, and $k = 2, \cdots, K_m - 1$) in the equation 5.37 may be approximated by using a set of central difference schemes, as follows:

$$(x_\xi)_{i,j,k} \approx \frac{x_{i+1,j,k} - x_{i-1,j,k}}{2\Delta\xi} \tag{5.42a}$$

$$(x_\eta)_{i,j,k} \approx \frac{x_{i,j+1,k} - x_{i,j-1,k}}{2\Delta\eta} \tag{5.42b}$$

$$(x_\zeta)_{i,j,k} \approx \frac{x_{i,j,k+1} - x_{i,j,k-1}}{2\Delta\zeta} \tag{5.42c}$$

$$(x_{\xi\xi})_{i,j,k} \approx \frac{x_{i+1,j,k} - 2x_{i,j,k} + x_{i-1,j,k}}{\Delta\xi^2} \tag{5.42d}$$

$$(x_{\eta\eta})_{i,j,k} \approx \frac{x_{i,j+1,k} - 2x_{i,j,k} + x_{i,j-1,k}}{\Delta\eta^2} \tag{5.42e}$$

$$(x_{\zeta\zeta})_{i,j,k} \approx \frac{x_{i,j,k+1} - 2x_{i,j,k} + x_{i,j,k-1}}{\Delta\zeta^2} \tag{5.42f}$$

$$(x_{\xi\eta})_{i,j,k} \approx \frac{x_{i+1,j+1,k} - x_{i+1,j-1,k} - x_{i-1,j+1,k} + x_{i-1,j-1,k}}{4\Delta\xi\Delta\eta} \tag{5.42g}$$

$$(x_{\xi\zeta})_{i,j,k} \approx \frac{x_{i+1,j,k+1} - x_{i+1,j,k-1} - x_{i-1,j,k+1} + x_{i-1,j,k-1}}{4\Delta\xi\Delta\zeta} \tag{5.42h}$$

$$(x_{\eta\zeta})_{i,j,k} \approx \frac{x_{i,j+1,k+1} - x_{i,j+1,k-1} - x_{i,j-1,k+1} + x_{i,j-1,k-1}}{4\Delta\eta\Delta\zeta} \tag{5.42i}$$

The equation 5.37 is then solved numerically using the same PSOR algorithm as employed in the 2D approach.

5.2.3 Numerical Examples

In this section, three examples are employed to verify the 3D extension of Jacobian-weighted elliptic method. The first example is a simple case of point attraction where the mesh is generated by considering the local refinement around two points. This

helps to show the regularity and alignment of the resulting mesh. The second example is a more complicated, but still analytically determined a helical trajectory. This will demonstrate more clearly the grid redistribution capability of the 3D Jacobian-weighted elliptic method for a complex three dimensional geometry. The last example is a feature-based three dimensional spherical shell, which relates to the value of a prescribed "solution" function. This example will further demonstrate the effectiveness of the approach on grid redistribution based on solution features.

Point Attraction In this example, a three-dimensional mesh of a unit cube was constructed using the 3D TFI method and adapted to two predetermined points, (x_1, y_1, z_1) = $(1/4, 1/2, 1/2)$ and (x_2, y_2, z_2) = $(3/4, 1/2, 1/2)$. The computational domain Ω_C = $[0, 1]^3$ was discretised into $n_\xi \times n_\eta \times n_\zeta$ cells, with $n_\xi = n_\eta = n_\zeta = 100$ ($N = 10^6$) and was mapped into the same physical domain with Dirichlet boundary conditions.

The control angle in the weight matrix of equation 5.40 was defined as $\theta = 0$, the local length scaling factors were explicitly given the same as the equation 5.21 with the relation $l_1 = l_2 = l_3$, where the radii of local refinement and transition regions were set to $R_1 = 0.05$ and $R_2 = 0.15$, respectively; the multi-level attraction was applied with the refinement strength of $a_1 = 0.6$, $a_2 = 0.7$, and $a_3 = 0.8$. Figure 5.7 presents the finally converged mesh with a tolerance of $\epsilon = 10^{-5}$, where a detailed view of the point attraction at slice A is plotted. From this simple test problem, it is clear to see that there are many more grid points in the region where the local refinement is imposed than outside of that region.

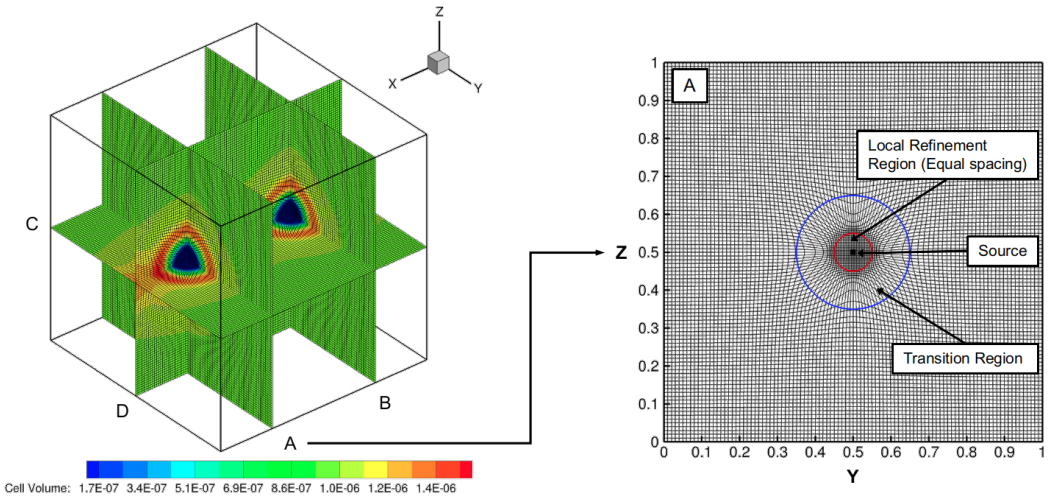

Figure 5.7: *3D plot of the point attraction case (the mesh was rendered by cell volume).*

Prescribed Trajectory Adaption We next consider a prescribed trajectory given by Landgrebe wake model [8] that describes a complex three dimensional helical blade tip vortex trajectory. This problem was selected as it results in a very non-uniform and distorted mesh, which is a major challenge for the algorithm. Furthermore, it is commonly encountered situation in helicopter rotor flow simulations. Taking $\boldsymbol{x} = (x, y, z)^T$, then

the Landgrebe prescribed wake model is given by

$$z_{tip} = \begin{cases} k_1 \Psi_w \cdot R & \text{for} \quad 0 \leq \Psi_w \leq \dfrac{2\pi}{N_b} \\ (z_{tip})_{\Psi_w = \frac{2\pi}{N_b}} + k_2 \left(\Psi_w - \dfrac{2\pi}{N_b} \right) \cdot R & \text{for} \quad \Psi_w \geq \dfrac{2\pi}{N_b} \end{cases} \tag{5.43}$$

and

$$r_{tip} = A + (1 - A) \cdot \exp\left(-\Lambda \Psi_w\right) \tag{5.44}$$

where Ψ_w is the wake age, N_b represents the number of blade, R is the rotor radius, k_1 and k_2 are axial settling rates describing the axial displacement, which can be modeled by the following equations

$$\begin{aligned} k_1 &= -0.25 \cdot \left(\frac{C_T}{\sigma} + 0.001 \theta_{tw} \right) \\ k_2 &= -\left(1.41 + 0.0141 \theta_{tw}\right) \cdot \sqrt{\frac{C_T}{2}} \end{aligned} \tag{5.45}$$

in which C_T is the thrust coefficient, θ_{tw} is the blade twist rate, and σ is the rotor solidity. A and Λ are empirical coefficients used to depict the radial contraction of the wake, which can be given by

$$\begin{aligned} A &= 0.78 \\ \Lambda &= 0.145 + 27 \cdot C_T \end{aligned} \tag{5.46}$$

In this test, a single blade rotor tip vortex trajectory was constructed with the rotor parameters of R = 0.25, σ = 0.053, $\theta_{tw} = 0°$, and C_T = 0.00464. An unit cube in computational space $\Omega_C = [0, 1]^3$ was split into $n_\xi \times n_\eta \times n_\zeta$ cells with $n_\xi = n_\eta = n_\zeta = 100$ ($N = 10^6$) and resulted in a uniform mesh in physical space via the 3D TFI approach.

The 3D Jacobian-weighted elliptic approach was applied to the helical trajectory adaption problem with the same formulation of the local length scaling factors as in the previous example, but with $R_1 = 0.01$ and $R_2 = 0.05$. A three levels of refinement strength parameters, $a_1 = 0.6$, $a_2 = 0.7$ and $a_3 = 0.8$, was used for grid redistribution. The convergence tolerance was set to $\epsilon = 10^{-4}$. For these parameter values, a highly non-uniform mesh without any mesh tangling was successfully generated, as illustrated in Figure 5.8, where the refined cells along with the prescribed helical trajectory are shown in Figure 5.8a. In Figure 5.8b we show two horizontal slices (ζ_1 and ζ_2) in the physical domain corresponding to the horizontal planes in computational domain. Figure 5.8c and 5.8d present the project view of aforementioned slices in physical space. These results show that the redistributed grid closely follows the prescribe trajectory, showing very clearly the fully 3D nature of the problem.

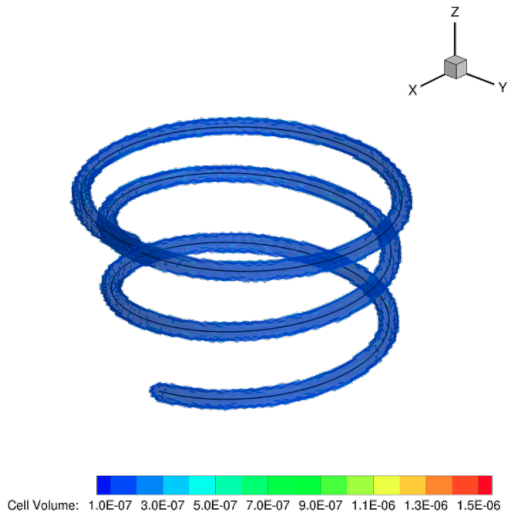

(a) *3D plot of the helical trajectory with refined cells in blue (black line is the trajectory created by Landgrebe wake model)*

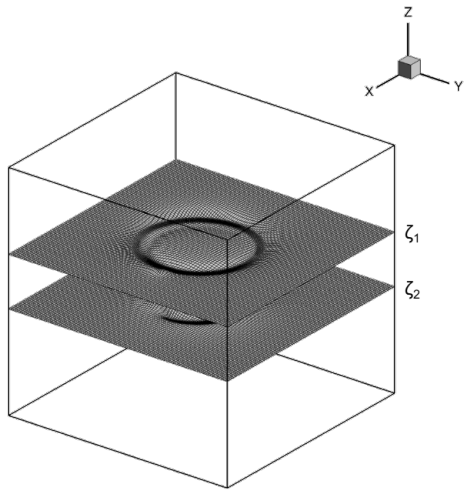

(b) *3D view in physical space of a grid with* $\zeta_1 = 66/100$ *and* $\zeta_2 = 44/100$ *slices in computational space*

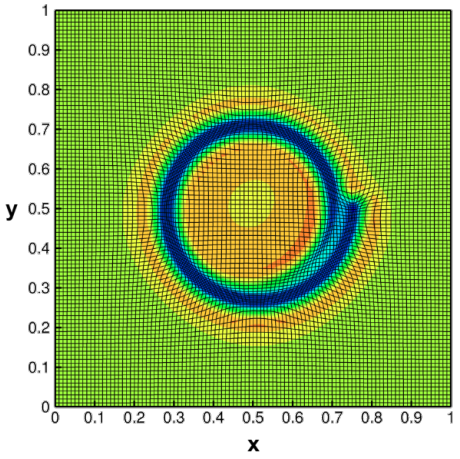

(c) *Projected view of the slice* $\zeta_1 = 66/100$ *in physical space*

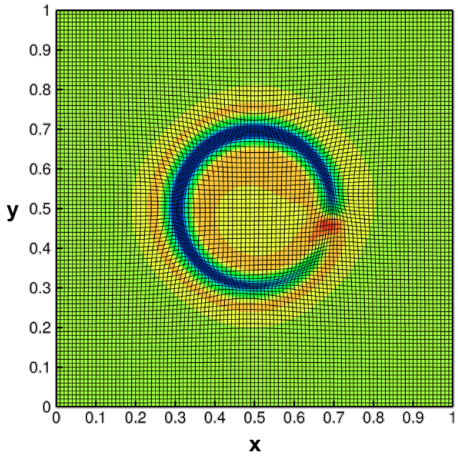

(d) *Projected view of the slice* $\zeta_2 = 44/100$ *in physical space*

Figure 5.8: *Detailed view of the helical trajectory adaption case (the mesh was rendered by cell volume)*

Feature-based Adaption This example is motivated by [134], where a density function $f(\boldsymbol{x})$ of a smooth 3D spherical shell is defined. This function is given as follows

$$f(\boldsymbol{x}) = f(x,y,z) = \begin{cases} 1 & \text{for} \quad s(x,y,z) \leq r_1 \\ \dfrac{1}{2}\cos\left(\dfrac{(s(x,y,z)-r_1)\,\pi}{r_2}\right) + \dfrac{1}{2} & \text{for} \quad s(x,y,z) \leq r_1 + r_2 \\ 0 & \text{for} \quad s(x,y,z) > r_1 + r_2 \end{cases} \tag{5.47}$$

with the distance function s

$$s(\boldsymbol{x}) = s(x, y, z) = \sqrt{(x - x_c)^2 + (y - y_c)^2 + (z - z_c)^2} \tag{5.48}$$

where r_1 represent the inner boundary of the spherical shell, r_2 is the width of the shell. (x_c, y_c, z_c) is the center of the shell. For accurately forming a spherical shell, we consider generating a mesh with concentrated grid points around the shell boundary. This is able to achieve by defining a local length scaling factor which is small when the derivatives of the density function $f(\boldsymbol{x})$ are large. Therefore, the length scaling factor used in the 3D Jacobian-weighted elliptic method is expressed as

$$l_1 = l_2 = l_3 = \frac{1}{\sqrt{1 + a^2 |\nabla_{\boldsymbol{x}} f|^2}} \tag{5.49}$$

where a is a regularisation constant that controls the attraction strength; $\nabla_{\boldsymbol{x}} f = [f_x, f_y, f_z]^T$ that can be written as

$$f_x = \frac{1}{\sqrt{g}} \left[(y_\eta z_\zeta - z_\eta y_\zeta) f_\xi + (z_\xi y_\zeta - y_\xi z_\zeta) f_\eta + (y_\xi z_\eta - z_\xi y_\eta) f_\zeta \right] \tag{5.50a}$$

$$f_y = \frac{1}{\sqrt{g}} \left[(z_\eta x_\zeta - x_\eta z_\zeta) f_\xi + (x_\xi z_\zeta - z_\xi x_\zeta) f_\eta + (z_\xi x_\eta - x_\xi z_\eta) f_\zeta \right] \tag{5.50b}$$

$$f_z = \frac{1}{\sqrt{g}} \left[(x_\eta y_\zeta - y_\eta x_\zeta) f_\xi + (y_\xi x_\zeta - x_\xi y_\zeta) f_\eta + (x_\xi y_\eta - y_\xi x_\eta) f_\zeta \right] \tag{5.50c}$$

In this example, the spherical shell is centered at $(x_c, y_c, z_c) = (1/2, 1/2, 1/2)^T$ with the shell geometric parameters of r_1 = r_2 = $1/6$. The domain is uniformly discretised into $100 \times 100 \times 100$ mesh cells.

This problem used a 3D Jacobian-weighted elliptic method with $a = 0.75$ and $\theta_o = 0$. The grid redistribution process converged to a tolerance of $\epsilon = 10^{-4}$. As shown in Figure 5.9, it is clear that many of the grid points are concentrated into the regions with large derivatives of the density function. Furthermore, the resulting mesh shows excellent alignment with the boundary of the shell. Figure 5.9a and 5.9b illustrate the changes between the initial and redistributed grids, where part of the sphere has been cut away to show the distribution of the density function. Figure 5.9c shows a slice of $\zeta = 33/100$ in the physical space that accurately follows the length scaling factor. Figure 5.9d is a detailed view of slice $\zeta = 51/100$ projected onto the $x - y$ plane in the physical domain. These indicate that the 3D Jacobian-weighted elliptic method is able to generate good regularity meshes for solution-based problems effectively.

5.3 Summary

This chapter presented the Jacobian-weighted elliptic grid generation method, for concentrating grid points into the regions of interest without creating additional points. It is an r- refinement technique that combines variational principle with least squares fitting of the inverse Jacobian matrix to a weight matrix to control the mapping from a uniform computational mesh to a bounded, simply connected mesh in physical domain. The original two-dimensional Jacobian-weighted elliptic method have been introduced first to demonstrate the effectiveness of this method. Later the three-dimensional extension of this method was derived in detail, the construction of the weight matrix for

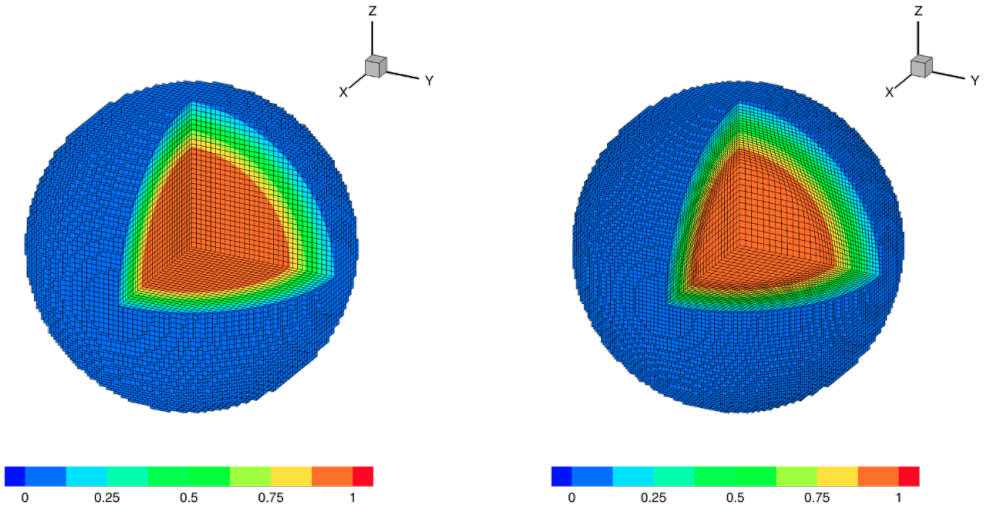

(a) *Cut away 3D plot of the density function on initial mesh for* $0.5 \leq f(\boldsymbol{x}) \leq 0.95$

(b) *Cut away 3D plot of the density function on converged mesh for* $0.5 \leq f(\boldsymbol{x}) \leq 0.95$

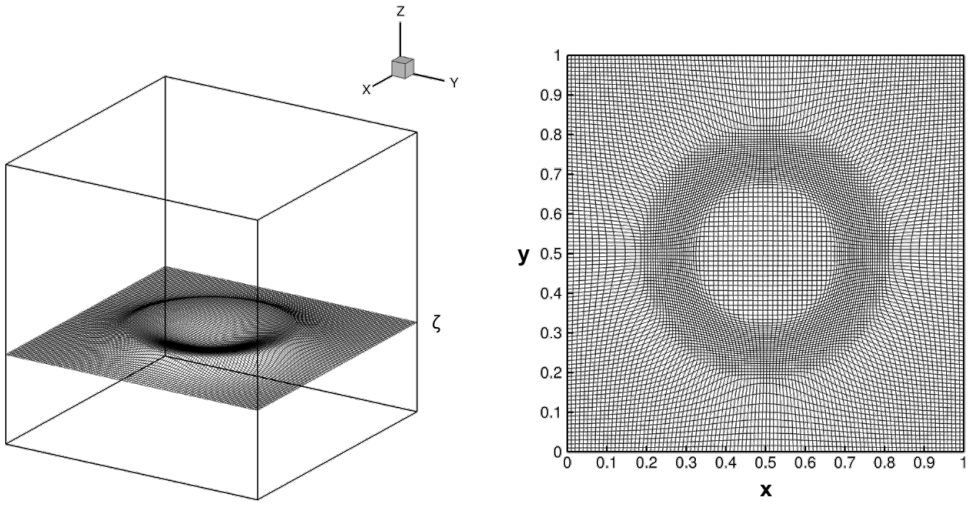

(c) *3D view of grid in physical domain with* ζ *= 33/100 slices in computational domain*

(d) *Projected view of the slice* ζ *= 51/100 in physical space*

Figure 5.9: *Feature-based 3D grid redistribution case (the mesh was rendered by density function)*

three-dimensional problems was clearly presented. Three different types of numerical examples were employed for validating both two- and three-dimensional methods. The investigations are summarized as follows:

- The implementation of the Jacobian-weighted elliptic method in two dimensions was verified from three numerical examples. It was shown that this method implemented correctly and demonstrated its effectiveness in concentrating mesh points into the desired region.
- From three numerical test cases, we have demonstrated that the Jacobian-weighted elliptic method was successfully extended to three dimensions. The performance of this extended approach in generating good regularity grids without mesh tan-

gling for three-dimensional meshes was well proved. The tip vortex trajectory adaption and the solution-based examples also showed its potential in helicopter rotor flows.

CHAPTER 6

Conclusions and Perspectives

6.1 Summary and Conclusions

This doctoral dissertation focused on the development of aerodynamic and aeroacoustic methods to better understand the complicated aeromechanical environment of helicopter rotors at hovering and forwarding flight conditions. The simulation of helicopter rotor flows was accomplished using Computational Fluid Dynamics based on the RANS equations.

In the first part (Chapter 2 and Chapter 3), an efficient simulation framework for helicopter aerodynamics and aeroacoustics was developed, in which the ROSITA CFD solver was integrated with a novel acoustic solver ROCAAP, and an efficient rotor trimming algorithm was introduced and implemented for simulating the helicopter rotor in forward flight condition. A sequence of numerical examples was employed in the verification and validation process, where the acoustic solver was validated by comparing with analytical and well-established solutions; the effectiveness and efficiency of the developed rotor trimming approach were validated by comparing with experimental data; the predictions of both transonic rotor noise and BVI noise were conducted with the aim of validating the integrated simulation framework.

The second part (Chapter 4) of this thesis presents the capability of the vortex feature-based VC2 (FVC2-Q and FVC2-L2) models to obtain the high-resolution vortical structures and reliable noise signals for helicopter rotor flows with moderate computational cost. Two benchmark tests, the NACA0015 wing in steady flow, the Caradonna-Tung helicopter rotor in hovering flight, were employed and results were compared with experimental data to illustrate the performance of the vortex feature-based VC2 models. It was found that with the introduction of the vortex feature detection techniques, the performance of the original VC2 model was improved in terms of computational stability, aerodynamic prediction, and vortex resolution due to the avoidance of over-

confinement inside the boundary layer. In particular, the λ_2-based VC2 (FVC2-L2) schemes expressed a higher resolution of vortical structure, more robust computational procedure, and more accurate aerodynamic loads if compared with the Q-based VC2 (FVC2-Q) model. In addition, it allows the use of higher confinement parameters on a coarse grid with a relatively higher computational efficiency to obtain better results than those of a finer grid. On this basis, the FVC2-L2 model was then applied to the HART-II baseline case to enhance the prediction of helicopter rotor BVI phenomenon. In helicopter rotor aeroacoustics, the effect of the FVC2-L2 model on aeroacoustic predictions was investigated using the UH-1H non-lifting rotor case and the AH-1/OLS low-speed forwarding flight case. It was observed that simulations with the FVC2-L2 model were capable of providing more reliable noise predictions than those without VC models, even when the tip vortices were not shed from the blade tip.

To explore the application of the r-refinement method on helicopter rotor flows, the last part (Chapter 5) introduced Kunpp's Jacobian-weighted elliptic method first for two-dimensional problems, where the variational principle was combined with the least-square fit to approximate the weight matrix to the inverse Jacobian matrix. The implementation of this method was verified by three different types of numerical examples. Afterward, this method was extended from two dimensions to three dimensions, where the derivation of weight matrix was presented for the first time. Through three different types of three-dimensional numerical examples, the capability of the three-dimensional Jacobian-weighted elliptic method in concentrating grid points into the regions of interest with good regularity was first demonstrated. Furthermore, the validations also showed its potential in helicopter rotor flows.

6.2 Research Contributions

This following points highlight the contributions of this dissertation to the simulation of helicopter rotor aerodynamics and aeroaocustics.

- **A novel acoustic solver for helicopter rotor subsonic and transonic/supersonic noise prediction**

  The permeable surface Ffocws-Williams and Hawkings acoustic pressure formulations for both subsonic and transonic/supersonic noise sources have been numerically implemented as an acoustic solver ROCAAP. Specifically, the Marching-Cube algorithm, originally conceived for ISO-surface construction, was combined with permeable surface Emission-Surface formulation for the first time to predict transonic rotor noise. The effectiveness of this method has been demonstrated in the UH-1H strong delocalized shock case ($M_T = 0.95$). The one-way coupling of the CFD solver ROSITA and the developed acoustic solver was achieved by developing an acoustic source extraction algorithm capable of automatically extracting porous control surfaces from a Chimera multi-block, structured grid.

- **A high-efficiency rotor trimming algorithm designated for CFD-based helicopter rotor simulation**

  The delta trim algorithm, derived from the coupling of the low-fidelity aerodynamics solver and the CFD solver, was combined with the multiple levels of grid and temporal resolutions, resulting in the multi-dimensional delta trim approach.

It was found to be more efficient than the original delta trim method by 12% in simulating the AH-1/OLS low-speed forwarding flight and 31% in computing the HART-II low-speed descent flight.

- **Explicitly presenting the benefits in CFD and acoustic results for the combination of vortex feature detection techniques and the original second vorticity confinement method**

  Two locally normalized vortex feature detection techniques (non-dimensional Q and λ_2 criteria) were combined with the original second vorticity confinement model, resulting in the FVC2-Q and the FVC2-L2 models, respectively. These two feature-based VC2 models have been implemented into the CFD solver ROSITA and compared with the results of the standard CFD solver and the original VC2 model. The results showed that the performances of the feature-based VC2 models on computational stability, aerodynamic loads prediction, and vorticity preservation were improved significantly, especially for the FVC2-L2 model. Moreover, it allows using higher confinement parameters on a coarse grid with a relatively higher computational efficiency to obtain more accurate results than those of a finer grid. On this basis, the FVC2-L2 model was adopted for the HART-II rotor descending flight case to improve the prediction of the helicopter rotor BVI phenomenon. In helicopter rotor aeroacoustics, computations with the FVC2-L2 model were shown to provide more reliable noise predictions than those without the VC model enabled, even if there were no tip vortices shed from the blade tip.

- **A three-dimensional r-refinement method for redistributing grid points in the desired regions without creating additional grid points**

  The Jacobian-weighted elliptic approach has been extended from two dimensions to three, and the weight matrix that control the grid movement for three-dimensional problems was derived for the first time. Three different types of numerical examples in three dimensions were employed for preliminary validating this method. The results showing that the presented method was effective and reliable in generating grids without mesh tangling after redistribution procedure. Furthermore, the potential of this method in the application of helicopter rotor flows was also demonstrated.

6.3 Perspectives

Based on the current thesis, some recommendations are proposed for future investigations in this section.

- **Transonic noise prediction for realistic high-speed forward flight helicopter rotors**

  In the current work, the investigation of transonic rotor noise prediction was only performed on the UH-1H hovering rotor case. Further studies for realistic high-speed forward flight helicopter rotors will provide valuable insight into the capabilities of transonic rotor noise prediction for the developed acoustic solver.

- **Developing a method to determine the confinement parameter automatically**
  Although the feature-based VC2 models allow using a higher value of confine-

ment parameters to achieve better results than the original VC2 model, the determination of the confinement parameters is still a very expensive task. A further investigation that automatically determines the confinement parameters is favorable.

- **Parallelization of the three-dimensional r-refinement method and testing this method as an adaptive generator incorporation with the CFD solver ROSITA for helicopter rotor quasi-steady and unsteady flows**

  Since the numerical algorithm used in the three-dimensional Jacobian-weighted elliptic method works serially, the computational time cost is relatively high, especially for large three-dimensional meshes. It is necessary to employ a parallel numerical algorithm or high-efficient algorithm to speed up the grid redistribution process so that the CFD solver can be coupled efficiently. In addition, this thesis only validates the three-dimensional r-refinement method preliminary. There is still a long distance to couple it with a CFD solver. For example, an effective and robust conservative interpolation method should be developed for transferring the solutions of the original grid to the redistributed grid accurately.

Bibliography

[1] K.S. Brentner, F. Farassat. Modeling aerodynamically generated sound of helicopter rotors. *Progress in Aerospace Sciences*, 39:83–120, 2003.

[2] J.G. Leishman. *Principles of Helicopter Aerodyamics, Second Edition*. Cambridge University Press, 2006.

[3] C.K. Zioutis, A.I. Spyropoulos, A.P. Fragias, D.P. Margaris, D.G. Papanikas. Influence of helicopter rotor wake modeling on blade airloads predictions. *International Journal of Engineering*, 3(6):521–537, 2010.

[4] J.M. Delery. Toward the elucidation of three-dimensional separation. *Annual Review of Fluid Mechanics*, 33:129–154, 2001.

[5] G. Romani. *Computational aeroacoustics of rotor noise in novel aircraft configurations: A lattice-boltzman method-based study*. PhD thesis, Delft University of Technology, February 2022.

[6] K.S. Brentner, F. Farassat. Helicopter noise prediction: The current status and future direction. *Journal of Sound and Vibration*, 170(1):79–96, 1994.

[7] S. Goldstein. On the vortex theory of screw propellers. *Proceedings of the Royal Society of London A, Mathematical Physical & Engineering Sciences*, 123(792):440–465, 1929.

[8] A.J. Landgrebe. Wake geometry of a hovering helicopter rotor and its influence on rotor performance. *Journal of the American Helicopter Society*, 17(4):3–15, 1972.

[9] J.D. Kocurek, J.L. Tangler. A prescribed wake lifting surface hover performance analysis. *Journal of the American Helicopter Society*, 22(1):24–35, 1977.

[10] D.B. Bliss, M.E. Teske, T.R. Quackenbush. A new methodology for free wake analysis using curved vortex elements. Technical report, NASA-CR-3958, 1987.

[11] F. Gandhi, L. Tauszig. A critical evaluation of various approaches for the numerical detection of helicopter blade-vortex interactions. *Joural of the American Helicopter Society*, 45(3):179–190, 2000.

[12] M.J. Bhagwat, J.G. Leishman. Stability, consistency and convergence of time-marching free-vortex rotor wake algorithms. *Journal of the American Helicopter Society*, 46(1):59–71, 2001.

[13] J.G. Leishman M.J. Bhagwat. Generalized viscous vortex model for application to free-vortex wake and aeroacoustic calculations. In *58th Annual Forum and Technology Display of American Helicopter Society International*, Montreal, Canada, June 2002.

[14] E.M. Murman T.W. Roberts. Solution method for a hovering helicopter rotor using the Euler equations. In *AIAA 23rd Aerospace Sciences Meeting*, Reno, USA, January 1985.

[15] N.L. Sankar, B.E. Wake, S.G. Lekoudis. Solution of the unsteady Euler equations for fixed and rotor wing configurations. *Journal of Aircraft*, 23(4):283–289, 1986.

[16] J.E. Deese R.K. Agarwal. An Euler solver for calculating the flowfield of a helicopter rotor in hover and forward flight. In *AIAA 19th Fluid Dynamics, Plasma Dynamics and Lasers Conference*, Honolulu, USA, June 1987.

[17] B.E. Wake, L.N. Sankar. Solutions of the Navier-Stokes equations for the flow about a rotor blade. *Journal of the American Helicopter Society*, 34(2):13–23, 1989.

[18] G.R. Srinivasan, J.D. Baeder, S. Obayashi, W.J. McCroskey. Flowfield of a lifting rotor in hover: A Navier-Stokes simulation. *AIAA Journal*, 30(10):2371–2378, 1992.

[19] J. Ahmad, E.P.N. Duque. Helicopter rotor blade computation in unsteady flows using moving overset grids. *Journal of Aircraft*, 33(1):54–60, 1996.

[20] F.R. Menter, J. Schutze, K.A. Kurbatskii, M. Gritskevich, A. Garbaruk. Scale-resolving simulation techniques in industrial CFD. In *6th AIAA Theoretical Fluid Mechanics Conference*, Honolulu, USA, June 2011.

[21] N.M. Chaderjian, J.U. Ahmad. Detached Eddy Simulation of the UH-60 rotor wake using adaptive mesh refinement. In *American Helicopter Society 68th Annual Forum*, Fort Worth, USA, May 2012.

[22] N.M. Chaderjian. Advances in rotor performance and turbulent wake simulation using DES and adaptive mesh refinement. In *7th International Conference on Computational Fluid Dynamics (ICCFD7)*, Hawaii, USA, July 2012.

[23] F. Dehaeze, G.N. Barakos, A.N. Kusyumov, S.A. Kusyumov, S.A. Mikhailov. Exploring the Detached-Eddy Simulation for main rotor flows. *Russian Aeronautics*, 61(1):37–44, 2018.

[24] W. Fu, J. Ma, J. Li. Investigation of rotor tip vortex in hover based on IDDES methods. *Journal of Northwestern Polytecnical University*, 37(1):195–202, 2019.

[25] G. Romani, D. Casalino. PowerFLOW simulations of helicopters in blade-vortex interaction conditions. In *The Vertical Flight Society 75th Annual Forum & Technology Display*, Philadelphia, Pennsylvania, USA, May 2019.

[26] W.C.P. van der Velden, G. Romani, D. Casalino. Validation and insight of a full-scale S-76 helicopter rotor using the Lattice-Boltzmann Method. *Aerospace Science and Technology*, 118, 2021.

[27] M.C. Ruiz, M. Scanavino, D. D'Ambrosio, G. Guglieri, A. Vilardi. Experimental and numerical analysis of hovering multicopter performance in low-Reynolds number conditions. *Aerospace Science and Technology*, 128, 2022.

[28] S.J. Kamkar, A. Jameson, A.M. Wissink, V. Sankaran. Automated off-body cartesian mesh adaption for rotorcraft simulations. In *49th AIAA Aerospace Science Meeting including the New Horizons Forum and Aerospace Exposition*, Orlando, USA, January 2011.

[29] X. Su. Accurate and robust adaptive mesh refinement for aerodynamic simulation with multi-block structured curvilinear mesh. *International Journal for Numerical Methods in Fluids*, 77:747–766, 2015.

[30] J.Y. Hwang, O.J. Kwon. Assessment of S-76 rotor hover performance in ground effect using an unstructured mixed mesh method. *Aerospace Science and Technology*, 84, 2019.

[31] C.J. Budd, W. Huang, R.D. Russell. Adaptivity with moving grids. *Acta Numerica*, 18:111–241, 2009.

[32] L. Tang, J.D. Baeder. A two-step grid redistribution method. *Computers and Fluids*, 32:323–336, 2003.

[33] A. Jimenez-Garcia, G.N. Barakos. Assessment of a high-order MUSCL method for rotor flows. *International Journal for Numerical Methods in Fluids*, 87:292–327, 2018.

[34] J.A. Ekaterinaris. High-order accurate, low numerical diffusion methods for aerodynamics. *Progress in Aerospace Sciences*, 41(3-4):192–300, 2005.

[35] Z.J. Wang. High-order methods for the Euler and Navier-Stokes equations on unstructured grids. *Progress in Aerospace Sciences*, 43(1-3):1–41, 2007.

[36] Z.J. Wang, K. Fidkowski, R. Abgrall, F. Bassi, D. Caraeni, A. Cary, H. Deconinck, R. Hartmann, K. Hillewaert, H.T. Huynh, N. Kroll, G. May, P. Persson, B. van Leer, M, Visbal. High-order CFD methods: Current status and perspective. *International Journal for Numerical Methods in Fluids*, 72:811–845, 2013.

[37] R. Steijl, G.N. Barakos, K.J. Badcock. A CFD framework for analysis of helicopter rotors. In *17th AIAA Computational Fluid Dynamics Conference*, Toronto, Canada, June 2005.

[38] T. Zhang, G.N. Barakos. High-fidelity numerical investigations of rotor-propeller aerodynamic interactions. *Aerospace Science and Technology*, 124, 2022.

[39] T.A. Fitzgibbon, G.N. Barakos. Investigation of wake breakdown in hover using the HMB3 solver. In *AIAA SCITECH 2022 Forum*, San Diego, USA, January 2022.

[40] Q. Zhao, G. Zhao, B. Wang, Q. Wang, Y. Shi, G. Xu. Robust Navier-Stokes method for predicting unsteady flowfield and aerodynamic characteristics of helicopter rotor. *Chinese Journal of Aeronautics*, 31(2):214–224, 2018.

[41] J.D. Baeder, S. Medida, T.S. Kalra. OVERTURNS simulations of S-76 rotor in hover. In *AIAA SCITECH 2014 Forum*, National Harbor, USA, January 2014.

[42] B. Lee, B. Govindarajan, J.D. Baeder. Methods for efficient resolution of vortical structures of an S-76 rotor in hover. In *AIAA SCITECH 2017 Forum*, Grapevine, USA, January 2017.

[43] D. Ghosh. *Compact-reconstruction weighted essentially non-Oscillatory schemes for hyperbolic conservation laws*. PhD thesis, University of Maryland, 2012.

[44] J.G. Coder. OVERFLOW rotor hover simulations using advanced turbulence and transition modeling. In *AIAA SCITECH 2017 Forum*, Grapevine, USA, January 2017.

[45] B.Y. Min, C.A. Reimann, B.E. Wake, S. Jee, J.D. Baeder. Hovering rotor simulation using OVERFLOW with improved turbulence model. In *AIAA SCITECH 2018 Forum*, Kissimmee, USA, January 2018.

[46] U. Kowarsch, M. Kebler, E. Kramer. High order CFD-simulation of the rotor-fuselage interaction. In *39th European Rotorcraft Forum*, Moscow, Russia, September 2013.

[47] U. Kowarsch, M. Kebler, E. Kramer. CFD-simulation of the rotor head influence to the rotor-fuselage interaction. In *40th European Rotorcraft Forum*, Southampton, UK, September 2014.

[48] U. Kowarsch, D. Lippert, S. Schneider, M. Kebler, E. Kramer. Aeroacoustic simulation of an EC145-T2 rotor in descend flight. In *AHS International 71st Annual Forum*, Virginia, USA, May 2015.

[49] U. Kowarsch, C. Ohrle, M. Kebler, E. Kramer. Aeroacoustic simulation of a complete H145 helicopter in descent flight. In *41st European Rotorcraft Forum*, Munich, Germany, September 2015.

[50] C. Ohrle, U. Schaferlein, M. Kebler. Higher-order simulations of a compound helicopter using adaptive mesh refinement. In *AHS International 74th Annual Forum*, Arizona, USA, May 2018.

[51] J.W. Kim, S.H. Park, Y.H. Yu. Euler and Navier-Stokes simulations of helicopter rotor blade in forward flight using an overlapped grid solver. In *19th AIAA Computational Fluid Dynamics Conference*, San Antonio, Texas, June 2009.

[52] Y. You, D. Na, S.N. Jung. Improved rotor aeromechanics predictions using a fluid structure interaction approach. *Aerospace Science and Technology*, 73:118–128, 2008.

[53] B. Van Leer. Towards the ultimate conservative difference scheme. v. a second-order sequel to godunov's method. *Journal of Computational Physics*, 32(1):101–136, 1979.

[54] E.P. Duque, R. Biswas, R.C. Strawn. A solution adaptive structured/unstructured overset grid flow solver with applications to helicopter rotor flows. In *13th AIAA Applied Aerodynamics Conference*, San Diego, USA, June 1995.

[55] R. Vasilescu. Rotor wake cpature improvement based on the controlled grid resolution. In *44th AIAA Aerospace Sciences Meeting and Exhibit*, Reno, USA, January 2006.

[56] H.Q. Yang, Z.J. Chen, A. Przekwas, J. Dudley. A high-order CFD method using successive differentiation. *Journal of Computational Physics*, 281:690–707, 2015.

[57] X.D. Liu, S. Osher, T. Chan. Weighted essentially non-oscillatory schemes. *Journal of Computational Physics*, 115(1):200–212, 1994.

[58] G.S. Jiang, C.W. Shu. Efficient implementation of weighted ENO schemes. *Journal of Computational Physics*, 126(1):202–228, 1996.

[59] R. Borges, M. Carmona, B. Costa, W.S. Don. An improved weighted essentially non-oscillatory scheme for hyperbolic conservation laws. *Journal of Computational Physics*, 227:3191–3211, 2008.

[60] J. Steinhoff, W. Yonghu, T. Mersch, H. Senge. Computational vorticity capturing: Application to helicopter rotor flow. In *30th Aerospace Sciences Meeting and Exhibit*, Reno, USA, January 1992.

[61] J. Steinhoff, D. Underhill. Modification of the Euler equations for "vorticity confinement": Application to the computation of the interacting vortex rings. *Physics of Fluids*, 6(8):2738–2744, 1994.

[62] J. Steinhoff, T. Mersch. Computation of incompressible flow over delta wings using vorticity confinement. In *32nd Aerospace Sciences Meeting and Exhibit*, Reno, USA, January 1994.

[63] J. Steinhoff, M. Fan, L. Wang, W. Dietz. Convection of concentrated vortices and passive scalars as solitary waves. *Journal of Scientific Computing*, 19(1-3):457–478, 2003.

[64] M. Biava, L. Vigevano. Assessment of the vorticity confinement technique applied to rotorcraft flows. In *21st AIAA Applied Aerodynamics Conference*, Orlando, USA, June 2003.

[65] M. Costes. Analysis of the second vorticity confinement scheme. *Aerospace Science and Technology*, 12(3):203–213, 2008.

[66] M. Costes. Stability analysis of the VC2 confinement scheme for the linear transport equation. *Computers and Fluids*, 86:537–557, 2013.

[67] M. Costes, F. Juillet. Analysis and higher-order extension of the vc2 confinement scheme. *Computers and Fluids*, 56:102–117, 2012.

[68] M. Costes, I. Petropoulos, P. Cinnell. Development of a third-order accurate vorticity confinement scheme. *Computers and Fluids*, 136:132–151, 2016.

[69] I. Petropoulos, M. Costes, P. Cinnell. Development and analysis of high-order vorticity confinement schemes. *Computers and Fluids*, 156:602–620, 2017.

[70] M. Costes. Development of a 3rd-order vorticity confinement scheme for rotor wake simulations. In *38th European Rotorcraft Forum*, Amsterdam, Netherlands, September 2012.

[71] R. Boisard, M. Costes, G. Reboul, F. Richez, B. Rodriguez. Assessment of aeromechanics and acoustics methods for bvi prediction using cfd. In *39th European Rotorcraft Forum*, Moscou, Russia, September 2013.

[72] M. Costes, R. Boisard, T. Renaud, F. Richez, B. Rodriguez. Investigation of vorticity confinement techniques for rotorcraft wake simulation. In *2nd Asian/Australian Rotorcraft Forum*, Tianjin, China, September 2013.

[73] S. Pevchin, B. Grossman, J. Steinhoff. Capture of contact discontinuities and shock waves using a discontinuity confinement procedure. In *35th Aerospace Sciences Meeting and Exhibit*, Reno, USA, January 1997.

[74] K. Yee, D.H. Lee. An Euler calculation for a hovering coaxial rotor flow field with new boundary condition. In *24th European Rotorcraft Forum*, Marseilles, France, 1998.

[75] G. Hu, B. Grossman, J. Steinhoff. Numerical method for vorticity confinement in compressible flow. *AIAA Journal*, 40(10):1945–1953, 2002.

[76] A. Dadone, G. Hu, B. Grossman. Towards a better understanding of vorticity confinement methods in compressible flow. In *15th AIAA Computational Fluid Dynamics Conference*, Anaheim, USA, June 2001.

[77] R. Lohner, C. Yang. Vorticity confinement on unstructure grids. In *40th Aerospace Sciences Meeting and Exhibit*, Reno, USA, January 2002.

[78] M.A. Robinson. Application of vorticity confinement to inviscid missile force and moment prediction. In *42nd Aerospace Sciences Meeting and Exhibit*, Reno, USA, January 2004.

[79] N. Butsuntorn, A. Jameson. Time spectral method for rotorcraft flow. In *46th Aerospace Sciences Meeting and Exhibit*, Reno, USA, January 2008.

[80] M. Costes, G.Kowani. An automatic anti-diffusion method for vortical flows based on vorticity confinement. *Aerospace Science and Technology*, 7(1):11–21, 2003.

[81] S. Hahn, G. Iaccarino. Towards adaptive vorticity confinement. In *47th Aerospace Sciences Meeting Including the New Horizons Forum and Aerospace Exposition*, Florida, USA, January 2009.

[82] D.F. Feder, A.M. Moustafa. Tracking a tip vortex with adaptive vorticity confinement and hybrid RANS-LES. *Open Journal of Fluid Dynamics*, 6(4):406–429, 2016.

[83] M. Mohseni, S.M. Malek Jafarian. Improvement of compressible vorticity confinement method by combining it with vortex feature detection methods. *Journal of Applied Fluid Mechanics*, 11(5):1395–1406, 2018.

[84] Z.J. Huang. *Numerical Sound Field Simulations of Supersonic Rotating Sources in a Uniform Mean-Flow of Arbitrary Direction*. PhD thesis, Vrije University Brussel, January 2019.

[85] C. Bailly, D. Juve. Numerical solution of acoustic propagation problems using linearized euler equations. *AIAA Journal*, 38(1):22–29, 2000.

[86] L. Liu, X. Li, F.Q. Hu. Nonuniform time-step Runge-Kutta Discontinuous Galerkin method for computational aeroacoustics. *Journal of Computational Physics*, 229(19):6874–6897, 2010.

[87] T. Yang, X. Chen, Q. Zhao, G. Zhao. Numerical study on the noise propagation characteristics of rotor in non-uniform downwash flowfield based on linearized euler equations. *Interantional Journal of Aeroacoustics*, 0(0):1–35, 2022.

[88] R.Ewert, W.Schroder. Acoustic perturbation equations based on flow decomposition via source filtering. *Journal of Computational Physics*, 188(2):365–398, 2003.

[89] K.S. Brentner, F. Farassat. An analytical comparison of the acoustic analogy and Kirchhoff formulation for moving surfaces. *AIAA Journal*, 36:1379–1385, 1998.

[90] B. Wang, Q. Zhao, G. Xu, L. Ye, J. Wang. Numerical analysis on noise of rotor with unconventional blade tips based on CFD/Kirchhoff method. *Chinese Journal of Aeronautics*, 26(3):572–582, 2013.

[91] N.D. Polyzos, S. Vouros, I. Goulos, V. Pachidis. Multi-disciplinary optimization of variable rotor speed and active blade twist rotorcraft: Trade-off between noise and emissions. *Aerospace Science and Technology*, 107, 2020.

[92] Y. Delorme, R. Stanly, S.H. Frankel, D. Greenblatt. Application of actuator line model for large eddy simulation of rotor noise control. *Aerospace Science and Technology*, 108, 2021.

[93] S. Vouros, I. Goulos, V. Pachidis. Integrated methodology for the prediction of helicopter rotor noise at mission level. *Aerospace Science and Technology*, 89, 2019.

[94] L. Wang, G. Xu, Y. Shi. Development and validation of a hybrid method for predicting helicopter rotor impulsive noise. *Proceedings of the Institution of Mechanical Engineers, Part G: Journal of Aerospace Engineering*, 233(4):1323–1339, 2019.

[95] J.E. Ffowcs Williams, D.L. Hawkings. Sound generation by turbulence and surfaces in arbitrary motion. *Philosophical Transactions of the Royal Society of London. Series A, Mathematical and Physical Sciences*, 264(1151):321–342, 1969.

[96] A.S. Lyrintizs. Review: The use of Kirchhoff's method in computational aeroacoustics. *Journal of Fluids Engineering*, 116(4):665–676, 1994.

[97] P.di Francescantonio. A new boundary integral formulation for the prediction of sound radiation. *Journal of Sound and Vibration*, 202(4):491–509, 1997.

[98] K.S. Brentner. A new algorithm for computing acoustic signals. *Preceedings of the IMACS 14th World Congress on Computational and Applied Mathematics*, 4:592–595, 1994.

[99] S. Ianniello. Algorithm to integrate the Ffowcs Williams-Hawkings equation on supersonic rotating domain. *AIAA Journal*, 37(9):1040–1047, 1999.

[100] S. Ianniello. Aeroacoustic analysis of high tip-speed rotating blades. *Aerospace Science and Technology*, 5(9):179–192, 2001.

[101] S. Ianniello. New perpectives in the use of the Ffowcs Williams-Hwakings equation for aeroacoustic analysis of rotating blades. *Journal of Fluid Mechanics*, 570(10):79–127, 2007.

[102] S. Loiodice, D. Drikakis, A. Kokkalis. An efficient algorithm for the retarded time equation for noise from rotating sources. *Journal of Sound and Vibration*, 412(6):336–348, 2018.

[103] S. Loiodice, D. Drikakis, A. Kokkalis. Emission surfaces and noise prediction from rotating sources. *Journal of Sound and Vibration*, 429(1):245–264, 2018.

[104] L. Vendemini, L. Vigevano. An emission surface approach for noise propagation from high speed sources. In *43rd European Rotorcraft Forum*, Milano, Italy, September 2017.

[105] F. Farassat, K.S. Brentner. Supersonic quadrupole noise theory for high-speed helicopter rotors. *Journal of Sound and Vibration*, 218(3):481–500, 1998.

[106] S. Ianniello. The k-algorithm and the modeling of the emission surface from supersonically rotating bodies. *Journal of Computational Physics*, 408, 2020.

[107] M. Biava, L. Vigevano. Simulation of a complete helicopter: A cfd approach to the study of interference effects. *Aerospace Science and Technology*, 19:37–49, 2012.

[108] V. Venkatakrishnan. On the accuracy of limiters and convergence to steady state solutions. In *31st Aerospace Sciences Meeting*, Reno, NV, USA, January 1993.

[109] G. Chesshire, W.D. Henshaw. Composite overlapping meshes for the solution of partial differential equations. *Journal of Computational Physics*, 90:1–64, 1990.

[110] D. Casalino. An advanced time approach for acoustic analogy predictions. *Journal of Sound and Vibration*, 261(4):583–612, 2003.

[111] F. Farassat. Derivation of formulations 1 and 1A of Farassat. Technical report, NASA/TM-2007-214853, 2007.

[112] C. Montani, R. Scateni, R. Scopigno. A modified look-up table for implicit disambiguation for marching cubes. *The Visual Computer*, 10:353–355, 1994.

[113] Z. Yang, L.N. Sankar, M. Smith, O. Bauchau. Recent improvements to a hybrid method for rotors in forward flight. In *38th Aerospace Sciences Meeting & Exhibit*, Reno, NV, USA, January 2000.

[114] J. Zhao, C. He. A viscous vortex particle model for rotor wake and interference analysis. *Journal of the American Helicopter Society*, 55, 2018. 012007.

[115] Y. Zhou, G. Hua, Y. Shi, R. Xia. A high-efficiency trim method for CFD numerical calculation of helicopter rotors. *International Journal of Aeronautical and Space Sciences*, 18(2):186–196, 2017.

[116] J.M. Drees. A theory of airflow through rotors and its application to some helicopter problems. *Journal of the Helicopter Association of Great Britain*, 3(2):79–104, 1949.

[117] K.S, Brentner. Prediction of helicopter rotor discrete frequency noise. Technical report, NASA/TM-87721, 1986.

[118] W. Zhu, M. Morandini, S. Li. Viscous vortex particle method coupling with computational structural dynamics for rotor comprehensive analysis. *Applied Sciences*, 11, 2021. 3149.

[119] J.L. Cross, M.E. Watts. Tip aerodynamics and acoustic test – A report and data survey. Technical report, NASA/RP-1179, 1988.

[120] W.R. Splettstoesser, K.J.Schultz, D.A. Boxwell, F.H. Schmitz. Helicopter model rotor-blade vortex interaction impulsive noise: Scalability and parametric variations. Technical report, NASA/TM-86007, 1984.

[121] R.C. Strawn, E.P.N. Duque, J. Ahmad. Rotorcraft aeroacoustics computations with overset-grid CFD methods. *Journal of the American Helicopter Society*, 44(2):132–140, 1999.

[122] B.G. van der Wall, C.L. Burley, Y. Yu, H. Richard, K. Pengel, P. Beaumier . The HART-II test – measurement of helicopter rotor wakes. *Aerospace Science and Technology*, 8:237–284, 2004.

[123] A.S. Morgans, S.A. Karabasov, A.P. Dowling, T.P. Hynes. Transonic helicopter noise. *AIAA Journal*, 43:1512–1524, 2005.

[124] D.A. Boxwell, Y.H. Yu, F.H. Schmitz. Hovering impulsive noise: Some measured and calculated results. *Vertica*, 3:35–45, 1979.

[125] T.W. Purcell. CFD and transonic helicopter sound. In *14th European Rotorcraft Forum*, Milano, Italy, 1988.

[126] J.R. Hunt, A. Wary, P. Moin. Eddies, stream, and convergence zones in turbulence flows. Technical report, Center for Turbulence Research Report CTR-S88, 1988.

[127] J. Jeong, F. Hussain. On the identification of a vortex. *Journal of Fluid Mechanics*, 285:69–94, 1995.

[128] O.K. Smith. Eigenvalues of a symmetric 3×3 matrix. *Communications of the ACM*, 4(4):168, 1961.

[129] K.W. McAlister, R.K. Takahashi. NACA0015 wing pressure and trailing vortex measurements. Technical report, NASA/TP-3151, 1991.

[130] W.M. Chan, P.G. Buning. Zipper grids for force and moment computation on overset grids. In *12th AIAA Computational Fluid Dynamics Conference*, San Diego, CA, USA, 1995.

[131] F.X. Caradonna, C. Tung. Experimental and analytical studies of a model helicopter rotor in hover. Technical report, NASA/TM-81232, 1981.

[132] M. Hafez, D. Brucker. The effect of artificial vorticity on the discrete solution of euler equations. In *10th Computational Fluid Dynamics Conference*, Honolulu, HI, USA, 1991.

[133] P.M. Knupp. Jacobian-weighted elliptic grid generation. *SIAM Journal of Scientific Computing*, 17(6):1475–1490, 1996.

[134] P.A. Browne, C.J. Budd, C. Piccolo, M. Cullen. Fast three dimensional r-adaptive mesh redistribution. *Journal of Computational Physics*, 275:174–196, 2014.